Kv channel interacting proteins (KChIPs) as Ca^{2+} sensors for Kv4 channels

Dissertation

to obtain the Doctoral Degree

(Dr. rer. nat.)

Handed to the Department of Biology of the Faculty for Mathematics, Informatics and Natural Sciences at Universität Hamburg

by

Georgios Tachtsidis

Hamburg, 2023

Gutachter:	Prof. Dr. Christian Lohr
	Prof. Dr. Robert Bähring
Datum der Disputation:	20.10.2023

Eidesstattliche Versicherung - Declaration on oath

Hiermit erkläre ich an Eides statt, dass ich die vorliegende Dissertationsschrift selbst verfasst und keine anderen als die angegebenen Quellen und Hilfsmittel benutzt habe.
I hereby declare, on oath, that I have written the present dissertation by my own and have not used other than the acknowledged resources and aids.

18.07.23 — G. Tachtsidis

Hamburg, den — Unterschrift

ZUSAMMENFASSUNG

Auswärtsgerichtete transiente Kaliumströme wurden vor über einem halben Jahrhundert erstmals beschrieben und seitdem wurden weitreichende Fortschritte im Verständnis ihrer molekularen Grundlagen, sowie ihrer physiologischen Funktion erzielt. Die spannungsabhängigen Kaliumkanäle der Kv4-Familie zeichnen sich durch eine schnelle Aktivierung und Inaktivierung aus und spielen eine entscheidende Rolle bei der Repolarisation von Herz- und neuronalen Aktionspotentialen sowie bei der Regulation der neuronalen Erregbarkeit. Diese Kanäle formen ternäre Komplexe zusammen mit den akzessorischen Untereinheiten: Kv-Kanal-interagierende Proteine (KChIPs) und Dipeptidyl Aminopeptidase-ähnliche Proteine (DPPs). KChIPs gehören zu der neuronalen Kalziumsensor Familie und besitzen vier EF-Hand-Domänen, von denen zwei Kalzium Ionen (Ca^{2+}) binden können.

Bisherige Studien deuten auf die potenzielle modulatorische Rolle von KChIP bei den Kv4-Kanal-Komplexen in Reaktion auf die intrazellulären Schwankungen der Ca^{2+} Konzentration hin. Diese Studien verwendeten jedoch indirekte Ansätze zur Beeinflussung des intrazellulären Ca^{2+}-Spiegels und die genaue akute Modulation des Kv4-Kanal-Komplexes durch die Bindung von Ca^{2+} an KChIP bleibt unklar.

Die vorliegende Studie untersuchte den modulatorischen Effekt von intern appliziertem Ca^{2+} auf Kv4.2-Kanal-Komplexe hinsichtlich des makroskopischen Stromabfalls, der Erholung von der Inaktivierung und der Spannungsabhängigkeit der steady-state Inaktivierung. Hierfür wurden Inside-out-Patches von HEK293T-Zellen und *Xenopus* Oozyten verwendet, um die modulatorischen Effekte von internem Ca^{2+} zu untersuchen. Zusätzlich kamen Epitop-markierte Kv4.2/KChIP-Konstrukte zum Einsatz, um die subzelluläre Verteilung von Kv4/KChIP-Kanal-Komplexen unter unterschiedlichen internen Ca^{2+}-Bedingungen zu untersuchen.

Die interne Applikation von Ca^{2+} führte zu widersprüchlichen Effekten zwischen den verwendeten Expressionssystemen. Darüber hinaus wurde festgestellt, dass eine Erhöhung der intern applizierten Ca^{2+}-Konzentration einige der mit weniger Ca^{2+} beobachteten Effekte teilweise umkehrte. Diese Ergebnisse werfen interessante Fragen auf, erstens hinsichtlich einer potenziell höherer lokaler Ca^{2+}-Konzentrationen in physiologischen Umgebung und zweitens hinsichtlich der Beteiligung anderer intrazellulärer Komponenten wie CaMKII bei der Modulation von Kv4-Kanal-Komplexen.

ABSTRACT

Transient outward potassium currents were first described over half a century ago and since then significant discoveries have been made in the understanding of their molecular basis as well as in their physiological roles. The Kv4 family of voltage-gated potassium channels, known for their rapid activation and inactivation, play a crucial role in the repolarization of heart and neuronal action potentials, as well as the regulation of neuronal excitability. These channels form ternary complexes with auxiliary subunits, including Kv channel interacting proteins (KChIP) and dipeptidyl aminopeptidase-like proteins (DPP). KChIP, belonging to the neuronal Ca^{2+} sensor family, possesses four EF-hands, two of which can bind Calcium ions (Ca^{2+}).

Studies so far indicate the potential modulatory role of KChIP in the Kv4 channel complexes in response to fluctuations of intracellular Ca^{2+} concentration. However, these studies relied on indirect approaches to manipulate internal Ca^{2+} levels and the precise acute modulation of the Kv4 channel complex through Ca^{2+} binding on KChIP remains unclear.

The present study investigated the modulatory effect of internally applied Ca^{2+} on Kv4.2 channel complexes on macroscopic current decay, recovery from inactivation and voltage dependence of steady-state inactivation. Inside-out patches from both HEK293T cells and *Xenopus* oocytes were utilized to study the modulatory effects of internal Ca^{2+}. Additionally, epitope-tagged Kv4.2/KChIP constructs were employed to study the subcellular distribution of Kv4/KChIP channel complexes under varying internal Ca2+ conditions.

Internal application of Ca^{2+} resulted in contradicting effects between the used expression systems. Furthermore, an increase in internally applied Ca^{2+} concentration partially reversed some of the observed effects with low Ca^{2+}. These findings raise intriguing questions regarding the potential existence of higher local Ca^{2+} concentrations in native environments or the involvement of other intracellular components, such as CaMKII, in modulating Kv4 channel complexes.

1. Introduction

It is intriguing to understand how perception and reaction evolved and how more complex behavior emerged through millennia of evolution. Every heartbeat and cognitive process hinges upon the precise orchestration of ion distribution and the generation of potential differences within excitable cells. Environmental influences, including various chemicals, can influence the internal distribution of ions within cells, leading to alterations in their electrical potential and triggering diverse cellular responses such as cellular contraction or chemical signaling with neighboring cells.

The primary contributors to the establishment of membrane potential and the basis for cellular excitability are sodium (Na^+) and potassium (K^+) ions. Each excitable cell is able to express Na^+-K^+-pumps which use energy in the form of adenosine-triphosphate (ATP) to transport Na^+ from the inside of the cell to the outside and in the opposite direction for K^+ ions, generating two large ionic gradients along the cell membrane and producing a resting membrane potential[1].

In the case of neurons, external stimuli can trigger a calculated series of events involving the opening and closing of ion channels, generating a rapid change in the membrane potential. Alan Hodgkin and Andrew Huxley were the first to describe this phenomenon using the voltage clamp method in isolated squid giant axon, which further led to the discovery of ionic fluxes in the action potential in nerve cells. They were awarded in 1963 (together with John Eccles) the Nobel Prize in physiology or medicine. First, after reaching a threshold in the membrane potential, Na^+ channels open, and Na^+ flows from the extracellular space into the cell, rapidly changing the negative membrane potential to a positive potential. Secondly, K^+ channels activate, allowing K^+ to flow from the cell to the extracellular space, shifting the positive membrane potential back to a negative potential. Such sequential changes form the foundation of electrical signal transduction within neurons, allowing their communication with one another[2].

Decades of research later revealed the myriad variations of action potentials across species, neuron types, and even different location of the same neuron. The human genome alone revealed the existence of over 300 distinct ion channels, each playing a unique role in shaping the characteristics of action potentials. Some ion channels require multiple subunits to come together and form a functional pore, which can give rise to either homomeric ion channels or heteromeric ion channels. Additionally, ion

channels can further be modulated by regulatory subunits, generating a vast diversity of ion channel populations, which contributes to the variety of action potential morphology[3,4].

1.1 Potassium channels

Potassium channels (K^+ channels) represent the largest and most varied group of ion channels. They are found across all domains of life, ranging from animals and plants to prokaryotes and archaea, with only a few exceptions among parasitic bacteria[5,6]. The great diversity of mammalian K^+ channels is a result of the abundance of genes encoding for K^+ channels, as well as the occurrence of alternative splicing of mRNA transcripts. Over 80 genes encoding for K^+ channels exist in the mammalian genome and can be divided into four subfamilies: 1. Ca^{2+}- and Na^+-activated K^+ channels (K_{Ca}, K_{Na}), 2. Voltage gated K^+ channels (Kv), 3. Inwardly rectifying K^+ channels (K_{IR}) and 4. Two pore domain K^+ channels (K_{2P})[7,8]. The structural basis of K^+ channels is either a dimer or a tetramer formed by monomers. Monomers consist of two, four or six transmembrane helices (Tm's) and contain one pore-forming domain (Figure 1.1). The pore-forming domain consists of a strictly conserved amino acid motive (TXGYGD) and acts as a selectivity filter for K^+ ions. The precise arrangement of carbonyl oxygen in the selectivity filter, which replicates the hydrated shell of K^+ ions, is what gives K^+ channels their high conductivity. This arrangement allows K^+ ions to diffuse efficiently through the selectivity filter, compensating for the energy required for dehydration. Four K^+ ions can sit in the selectivity filter, where each K^+ ion sits in between two oxygen layers. Furthermore, because of this arrangement of the selectivity filter carbonyl atoms, the filter is more selective for K^+ ions than Na^+ ions. Despite Na^+ ions having a smaller ionic radius, it is energetically unfavorable for them to permeate the K^+ channel due to the greater ion-ligand distance in the selectivity filter[9–11].

In the K^+ channel family, inwardly rectifying K_{IR} channels have the simplest transmembrane structure. They consist of two transmembrane domains and are linked by an extracellular pore-forming region that is equivalent of the S5 and S6 of voltage-gated potassium channels (more detailed description in Chapter 1.2 Voltage gated potassium channels). The K_{IR} channel family includes 15 members and is divided into seven subfamilies. They exhibit diverse physiological roles depending on channel localization, ion flux, and the regulation of pore opening. K_{IR} channels have a distinctive characteristic where they allow the conduction of K^+ ions during hyperpolarization, unlike other K^+ channels that conduct ions during depolarization. Magnesium and

polyamines block the channel internally during depolarization, causing inward rectification, which is then released during hyperpolarization to allow K^+ to enter the cell. K^+ outward conductance is maintained around the reversal potential of K^+ at the resting membrane potential to control a wide range of cellular functions[8,11,12].

The K_{2P} channels consist of 15 members, and they are characterized by having four transmembrane domains with two pore-forming domains. They exhibit a topology similar to that of two K_{IR} channels fused together in tandem. These channels are commonly known as "leak channels" because they remain open constitutively, allowing a continuous flux of K^+ ions. This activity helps in stabilizing the negative membrane potential around the reversal potential of K^+ and counterbalancing depolarization. Their activity, however, can be regulated by diverse mediators like pH, temperature, mechanical force, lipids and regulatory proteins[13,14].

The Ca^{2+}- and Na^+-activated potassium channels consist of eight members divided into three subfamilies. The first two subfamilies are the large conductance Ca^{2+}-activated K^+ channels (BK) and the small conductance Ca^{2+}-activated K+ channels (SK). SK channels consist of six transmembrane domains (S1-S6) with an N- and C-terminus on the intracellular side, while BK channels consist of seven transmembrane domains with an additional transmembrane domain (S0) before the S1 segment, resulting in an extracellular N-terminus. Both shift in their open probability by elevation of intracellular Ca^{2+}. BK channels have a cytoplasmic regulatory unit on the C-terminal side, which can bind Ca^{2+} and regulate BK channels, while SK channels are regulated by Calmodulin. The third group of the subfamily are the Na^+-activated channels. They consist of six transmembrane domains and have, similar to BK channels, a regulatory unit at the C-terminal cytoplasmic side, which are sensitive to Na^+ and Cl^-. These channels exhibit diverse functionality in the regulation of smooth muscle contractility, action potential firing, and neuronal plasticity[15].

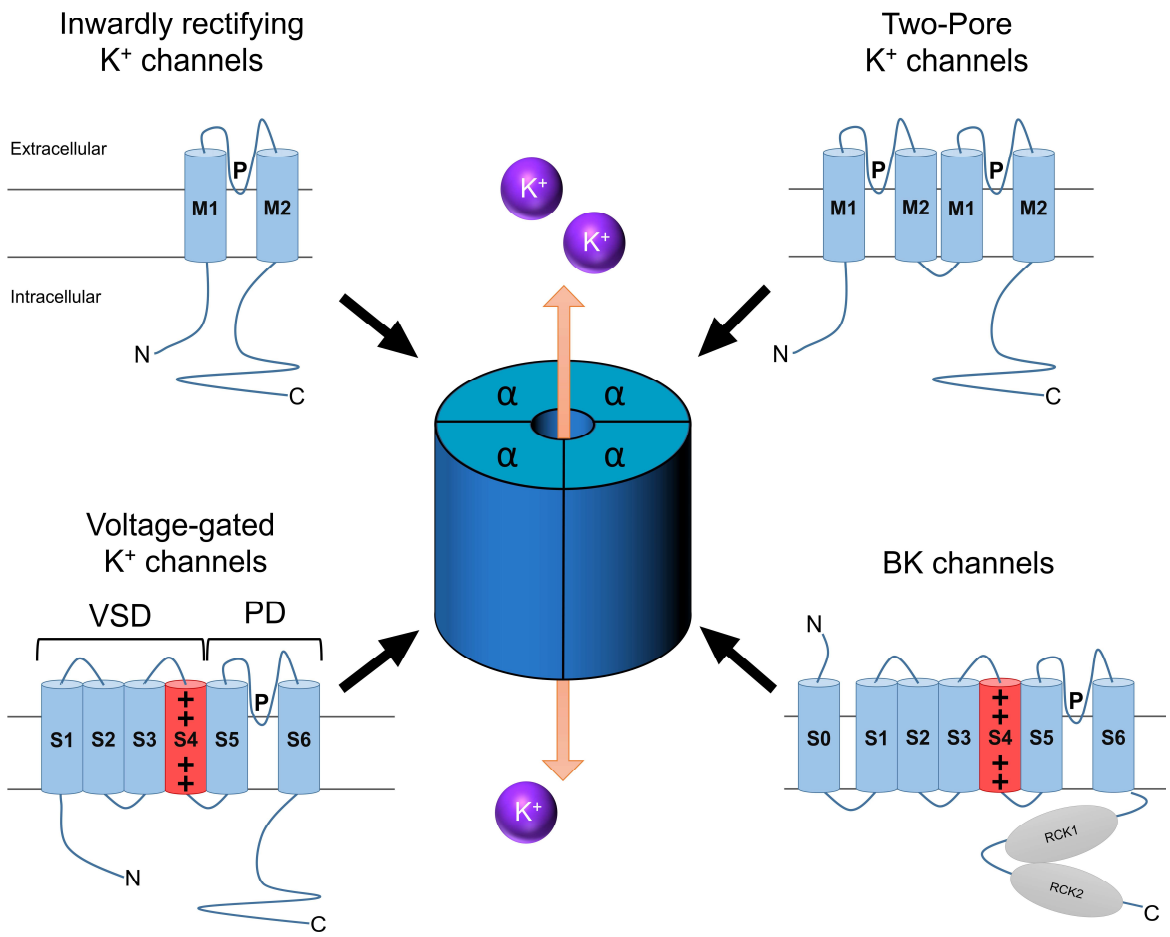

Figure 1.1: Topology diagrams of K^+ channel α-subunits.
K^+ channels can exhibit a variety of membrane topologies, depending on the family to which they belong. Most K^+ channels are formed by combining four α-subunits into one functional channel. In the case of two-pore K^+ channels, two α-subunits form a functional K^+ channel. Voltage-gated K^+ channels are characterized by two distinct functional domains: the voltage-sensing domain (VSD) and the pore-forming domain (PD). The VSD contains a transmembrane helix with positively charged amino acids that enables it to detect changes in membrane potential, and the PD contains the selectivity filter. BK channels contain an additional transmembrane helix as well as intracellular Ca^{2+} sensing domains called regulator of the conductance of K^+ ion (RCK).

1.2 Voltage-gated potassium channels and A-Type channels

The voltage-gated potassium channels (Kv) represent the largest K^+ channel family, comprising 40 genes that encode for the α-subunit and are further divided into 12 subfamilies. The principle function of these channels are the selective efflux of K^+. Kv channels play an important regulatory role in various cellular processes like the regulation of cellular excitation, apoptosis, cell differentiation, and cell growth[16]. Structurally, Kv channels consist of six transmembrane domains (S1-S6), which can be subdivided into two key regions: the voltage-sensing domain (VSD) located in the S1-S4 region and the pore-forming domain located in S5-S6. The VSD contains positively charged amino acids in the S4 segment, rendering Kv channels sensitive to

changes in the membrane potential. The pore-forming domain S5-S6 contains the selectivity filter as well the channel gate[16]. Kv1-4 channels, additionally, have a tetramerization domain (T1-domain), which is located before the first transmembrane segment at the N-terminal side in the cytoplasm. Its functionality is the specific tetramerization of Kv α-subunits as homomers, but additionally allows the assembly of heteromeric channels of the same subfamily but not between other subfamilies (e.g. Kv4.2/Kv4.3 heteromer)[17]. Similarly, Kv10-12 subfamilies can form homo- or hetero-multimers through a recognition site in the C-terminal domain[18]. In the case of the Kv7 channel subfamily, tetramerization occurs via a C-terminal domain, resembling BK channels. Kv channels in families 5, 6, 8 and 9 do not form functional channels by itself, but function as modulators and regulators for Kv2 channel subfamily[8,19].

A-type channels

Voltage-gated K^+ channels of the families Kv4, Kv3.3, Kv3.4 and Kv1.4 exhibit fast transient K^+ currents, which are referred to as A-type channels. This characteristic phenotype of fast activation and immediate rapid inactivation was initially observed in neurons from sea slugs[20]. The rapid inactivation kinetics in A-type channels have been described in Kv1.4 by two distinct types of inactivation: N-type and C-type inactivation. Fast N-type inactivation involves the binding of the N-terminal peptide in the central cavity in the inner pore and is further described as a “ball and chain” mechanism, while slower C-type inactivation involves the partial collapse of the outer pore[21].

The Kv4 subfamilies can also undergo N-type inactivation when expressed alone, but they additionally exhibit a unique inactivation process called closed-state inactivation (CSI). CSI allows Kv4 channels to undergo inactivation without prior channel opening, whereas N- and C-type inactivations require voltage-induced channel opening. The mechanism of CSI has been widely studied, and a dynamic coupling between the S4-S5 linker region and the activation gate in the distal S6 area has been proposed[22,23]. Recently, the mechanism of CSI was first resolved structurally by Ye and co-workers, which show the symmetry breakdown (4-fold symmetry to 2-fold symmetry) in the central cavity involving the conformational changes of two of the four S4-S5 linkers[20,24]. (Figure 1.2 A)

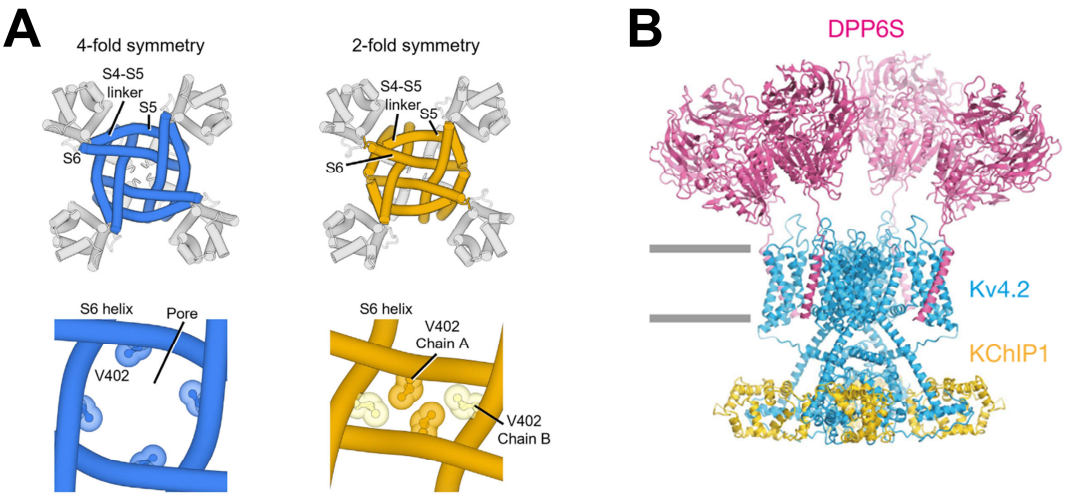

Figure 1.2: Kv4.2 channel conformations (Ye *et al*., 2022) and structure of Kv4.2/KChIP1/DPP6 channel complex (Kise *et al*., 2021, Ma *et. al*., 2022).
(**A**) Pore-forming S6 helices in open state (blue) and inactivated state (yellow) showcasing closed state inactivation and the symmetry breakdown of the central cavity. (**B**) Structure of Kv4.2 channel complex. Kv4.2 channels (blue) form together with auxiliary subunits KChIP (yellow) and DPP6 (red) a dodecamer in a 4:4:4 stoichiometry.

1.3 Auxiliary subunits and the Kv4.2 channel complex

Kv4 channel complexes generate subthreshold A-type K^+ currents (I_{SA}), which play a crucial role in determining neuronal firing activity and synaptic integration by activating at membrane potentials more negative than those required for the generation of action potentials. Initially, when Kv4 channels were expressed heterologously, differences in channel kinetics were observed compared to native mammalian A-type currents. This gave the awareness of potentially other modulatory elements for the Kv4 channel complexes.

An and coworkers were the first to describe an auxiliary subunit of the Kv4 channel using yeast two-hybrid screening and named it Kv channel-interacting protein (KChIP). KChIPs are a subfamily of the neuronal Ca^{2+} sensor (NCS) family and can further be divided into 4 members (KChIP1-4) with multiple splice variants[25,26]. Similar to other NCS family members, KChIPs consist of N- and C-terminal lobules, each containing two EF-hand motifs. EF1 on the N-terminal lobule is degenerated and cannot bind Ca^{2+} and EF2 mediates a low affinity for Ca^{2+} and, under physiological conditions, is bound to Mg^{2+}. EF3 and EF4, however, show a high affinity for Ca^{2+} and conformational changes in the form of reduced helical content and increased flexibility[27,28]. Every KChIP member shares a highly conserved core domain containing the four EF hands but vary in their N-terminal domain through alternative splicing. They exhibit a specific tissue expression pattern and furthermore expression levels of splice variants vary

significantly between different neuronal populations in the brain[26]. Despite their modulatory role in Kv4 channels, KChIPs have additional functions such as binding to presenilin, regulating Ca^{2+} homeostasis, controlling gene transcription, and furthermore, regulating other ion channels[27,29–32].

In Kv4 channels, KChIPs bind to the N-terminal side in a 4:4 stoichiometry and interact with the T1 domain of neighboring Kv4 α-subunits. Recent cryo-electron microscopy studies have shown that KChIP2 binds to the N-terminal side of one Kv4.2 α-subunit and also interacts with two C-terminal helices of the neighboring Kv4.2 α-subunit[33–35]. The Co-expression of Kv4 channels together with KChIPs results (with some exceptions) in enhanced surface expression and additionally modulate inactivation kinetics by slowing macroscopic current decay, accelerating the recovery from inactivation, and shifting the voltage dependence of inactivation positive.

While KChIPs are integral modulatory components of Kv4 channels that partially reconstitute the properties of I_{SA} from mammalian neurons, differences have been observed, suggesting the presence of additional modulatory elements.

Another modulator of Kv4 channels, called dipeptidyl aminopeptidase-like protein (DPPX or DPP6), was discovered by Nadal and colleagues[36]. DPP6 is a 115 kDa membrane integral protein with a short N-terminal cytoplasmic domain, a single transmembrane segment, and a large C-terminal domain lacking in protease activity[37]. Together with DPP10, which shares high sequence identity with DPP6, nine variants exist with a variable N-terminal domain and are widely expressed in different tissues as well as in different neuronal populations[38,39]. DPP6 proteins interact with Kv4 channels through the transmembrane segment with the S1 and S2 transmembrane segments of the Kv4 channel in a 4:4 stoichiometry[35]. Their variable N-terminal domain can interact with the cytoplasmic side of the channel complex and modulates the inactivation kinetics[28]. The co-expression of DPP with Kv4 channels results in enhanced surface expression and additionally modulate inactivation kinetics by acceleration macroscopic current decay, accelerating the recovery from inactivation, and shifting the voltage dependence of inactivation and voltage dependence of activation negative. The co-expression of Kv4 channels together with DPP and KChIP proteins results in a macromolecular ternary complex with a 4:4:4 stoichiometry (Figure1.1 B) that mediates currents, which resemble I_{SA} currents in neurons[40].

1.4 Kv4 complex interactions as supramolecular machinery – Aim of study

The association of Kv4 α-subunits with KChIP raises questions about the dynamic regulation of Kv4 channel complexes in response to intracellular Ca^{2+} fluctuations. Limited studies have reported indirect and partially conflicting findings. Wang and coworkers reported that elevation of Ca^{2+} in rat granule neurons increased I_{SA} peak amplitude, slowed macroscopic current inactivation, and shifted the voltage dependence of inactivation to potentials that were more negative[41]. Anderson and Co-workers reported a potential interaction between Kv4 channels, KChIP, and T-type voltage-gated Ca^{2+} channels (CaV3), where CaV3 channels are thought to serve as a physiological source of intracellular Ca^{2+}. Blocking CaV3 channels with mibefradil, and therefore reducing Ca^{2+} influx, resulted in a negative shift in the voltage dependence of inactivation and suggested a reduced KChIP effect[42,43].

These previous investigations into Kv/KChIP/Ca^{2+} interactions have predominantly relied on indirect methods that manipulate intracellular Ca^{2+} levels. However, these approaches lack precision in determining the exact intracellular Ca^{2+} concentration and may be influenced by additional intracellular components. Consequently, the precise acute modulation of the Kv4 complex through Ca^{2+} binding to KChIP has remained unclear.

The objective of the present study is to investigate the acute modulation of Kv4 channel complexes through direct internal application of Ca^{2+}. In addition, the study aims to investigate the association/dissociation of Kv4.2 and KChIP, as well as the trafficking and subcellular localization of these channel complexes. To achieve this, diverse experimental approaches will be employed to study the underlying molecular mechanisms of Kv4/KChIP modulation by internal Ca^{2+}.

This will involve utilizing C-terminal fluorophore-tagged Kv4.2 and KChIP in transiently transfected HEK293T cells, subjecting them to varying Ca^{2+} conditions post-transfection. Furthermore, the FRET efficiency of epitope-tagged constructs will be evaluated and optimized with different linker lengths for future studies of conformational changes in Kv4/KChIP channel complexes under fluctuating internal Ca^{2+} concentrations using transiently transfected cell lines and combining it with electrophysiological methods such as patch clamp fluorometry. This objective can be further divided into the following components:

1) Characterization of fluorophores mRuby3 and mClover3, construction of C-terminal-tagged Kv4.2-mClover3 and KChIP2-mRuby3 and determination of FRET efficiency of channel complexes with varying C-terminal linker lengths.
2) Electrophysiological evaluation of both wild type and epitope-tagged Kv4.2/KChIP channel complexes in two-electrode voltage clamp from *Xenopus* oocytes and, additionally, inside-out macro patches from *Xenopus* oocyte membranes.
3) Initial testing of combined electrophysiological recordings and fluorometry (patch clamp fluorometry) in epitope-tagged Kv4/KChIP channel complexes under varying intracellular Ca^{2+} concentrations in inside-out macro patches from *Xenopus* oocyte membranes (Please note that the present study will not showcase patch clamp fluorometry recordings, as this method yielded unsatisfactory results. Consequently, the main focus shifted to electrophysiological recordings).
4) Investigation of the trafficking and subcellular localization of epitope-tagged Kv4.2/KChIP channel complexes in transiently transfected HEK293 cells under different intracellular Ca^{2+} conditions using BAPTA-AM.

For the investigation of the acute modulatory effect of intracellular Ca^{2+} on Kv4.2/KChIP channel complexes, this study utilizes inside-out patches from *Xenopus* oocyte membranes, as well as mammalian cell lineage HEK293T. The study primarily focuses on the acute modulation of intracellular Ca^{2+} in the macroscopic inactivation kinetics, the recovery from inactivation, and the voltage dependence of steady-state inactivation. This objective can be further divided into the following parts:

1) The acute modulation in macroscopic inactivation kinetics and recovery from inactivation with varying internal Ca^{2+} concentrations in wild type Kv4.2 channel complexes studied in inside-out patches from *Xenopus* oocyte membranes.
2) The evaluation of the effect of patch excision on inactivation kinetics and recovery from inactivation in epitope-tagged Kv4.2 channel complexes in transiently transfected HEK293T cells.
3) The acute modulation in inactivation kinetics and recovery from inactivation with varying internal Ca^{2+} in epitope-tagged Kv4.2 channel complexes studied in inside-out patches from transiently transfected HEK293T cells.

2. Material

2.1 Chemicals, enzymes and supply material

The following materials were used in the experiments, unless otherwise specified. Chemicals were obtained from Sigma-Aldrich/Merck (Darmstadt), Roth (Karlsruhe) and ThermoFischer (Dreieich), while digestion enzymes were obtained from New England Biolabs (Frankfurt am Main) and ThermoFischer (Dreieich).
Oligonucleotides were synthesized by Eurofins (Hamburg) or ThermoFischer (Dreieich).
Cell culture media were obtained from Gibco Invitrogen (Karlsruhe).

Centrifugation steps were carried out using *Biofuge pico*, *Biofuge stratos* (Heraeus, Hanau), *5417R*, and *Concetrator Plus* (Eppendorf, Hamburg).
Bacterial cultures were incubated in either *Function line* (Heraeus, Hanau) or *ES-20* (Biosan, Riga), while cell lines were incubated in *HERA cell* (Heraeus, Hanau) and *NB203XL* (N-Biotek, Bucheon-si).

2.2 Buffer and solutions

Calculation of free Mg^{2+} and Ca^{2+} were made using WebmaxcS standard with the following settings: Temperature: +21°C, pH 7.2, Ionic strength 0.16.

***Xenopus* solutions**

OR1	75 mM NaCl, 5 mM Na pyruvate, 2 mM KCl, 2 mM $CaCl_2$, 1 mM $MgCl_2$, 5 mM HEPES, pH7.5 NaOH, sterile filtered
OR2	82.5 mM NaCl, 2 mM KCl, 1 mM $MgCl_2$, 5 mM HEPES, pH7.5 NaOH, sterile filtered
ND96	96 mM NaCl, 2 mM KCl, 1.8 mM $CaCl_2$, 1 mM $MgCl_2$, 5 mM HEPES, pH7.4 NaOH, sterile filtered
ND96 15mM Cl^-	7.4 mM NaCl, 88.6 mM Na-aspartate, 2 mM KCl, 1.8 mM $CaCl_2$, 1 mM $MgCl_2$, 5 mM HEPES, pH7.4 NaOH, sterile filtered

Oocyte shrinking buffer	200 mM K-aspartate, 20 mM KCl, 1 mM $MgCl_2$, 5 mM EGTA, 10 mM HEPES pH 7.4 KOH, sterile filtered
Internal solution (High Cl^-) (0 µM free Ca^{2+})	98 mM KCl, 0.5 mM $MgCl_2$, 1 mM EGTA, 10 mM HEPES pH 7.2 KOH, sterile filtered
Internal solution (High Cl^-) (10 µM free Ca^{2+})	98 mM KCl, 0.5 mM $MgCl_2$, 1 mM EGTA, 0.993 mM $CaCl_2$, 10 mM HEPES pH 7.2 KOH, sterile filtered
Internal solution (Low Cl^-) (0 µM free Ca^{2+})	138 mM KOH, 2 mM KCl, 5 mM EDTA, 5 mM HEDTA, 5.73 mM $MgMeSO_3$, 20 mM HEPES pH 7.2 $MeSO_3$, sterile filtered
Internal solution (Low Cl^-) (10 µM free Ca^{2+})	138 mM KOH, 2 mM KCl, 5 mM EDTA, 5 mM HEDTA, 4.97 mM $MgMeSO_3$, 5.55 mM $CaMeSO_3$ pH 7.2 $MeSO_3$, sterile filtered
External solution (Low Cl^-)	137 mM NaOH, 3.2 mM KCL, 1.2 mM $CaCl_2$ 1 mM $MgCl_2$, 20 mM HEPES pH 7.2 $MeSO_3$, sterile filtered

HEK293T solutions

Bath solution	150 mM KCl, 1 mM $MgCl_2$, 1.5 mM $CaCl_2$, 10 mM HEPES pH 7.2 KOH, sterile filtered
Internal solution (0 µM free Ca^{2+})	150 mM KCl, 1 mM $MgCl_2$, 1 mM EGTA, 10 mM HEPES pH 7.2 KOH, sterile filtered
Internal solution (10 µM free Ca^{2+})	150 mM KCl, 1 mM $MgCl_2$, 0.992 mM $CaCl_2$, 1 mM EGTA, 10 mM HEPES pH 7.2 KOH, sterile filtered
Internal solution (50 µM free Ca^{2+})	150 mM KCl, 1 mM $MgCl_2$, 1.05 mM $CaCl_2$, 1 mM EGTA, 10 mM HEPES pH 7.2 KOH, sterile filtered
External solution	150 mM NaCl, 3.5 mM KCl, 1 mM $MgCl_2$,1.2 mM $CaCl_2$, 10 mM HEPES pH 7.2 NaOH, sterile filtered

Imaging solution 1	150 mM NaCl, 1 mM $MgCl_2$, 1.5 mM $CaCl_2$, 10 mM HEPES pH 7.2 NaOH, sterile filtered
Imaging solution 2 (Ca^{2+} free)	150 mM NaCl, 1 mM $MgCl_2$, 10 mM HEPES, 30 µM BAPTA-AM, pH 7.2 NaOH, sterile filtered

2.3 Bacterial cultivating media

LB-Medium	10 g/L tryptone, 5 g/L yeast extract, 10 g/L NaCl, 100 mg/L carbenicillin
LB-Agar	35 g/L LB Agar (Lennox), 100 mg/L carbenicillin

2.4 Bacterial strains

Escherichia coli JM109	endA1, recA1, gyrA96, thi, hsdR17 (rk–, mk+), relA1, supE44, Δ(lac-proAB), [F´ traD36, proAB, laqIqZΔM15] (Hanahan,D. *et al.*, 1985)
Escherichia coli NEB® 5-alpha	fhuA2Δ(argF-lacZ)U169 phoA glnV44 Φ80Δ(lacZ)M15 gyrA96 recA1 relA1 endA1 thi-1 hsdR17 (New England BioLabs catalog C2987)

2.5 Cell lines

HEK293T	human primary embryonic kidney cell line 293 (ACC 305) carrying a plasmid containing the temperature sensitive mutant of SV-40 large T-antigen (tsA1609) (DSMZ Nr. ACC 635)
CHO-K1	Chinese hamster (*Cricetulus griseus*) ovary cell line derived as subclone from parental CHO cell line (DSMZ Nr. ACC 110)

2.6 Vectors

pcDNA3(-)	Expression vector used for heterologous expression in cultivated cell lines.
pGEM-HE Juel	T7 RNA transcription vector containing untranslated regions of β globin gene from *Xenopus laevis* and additional polyadenylation sequence.

2.7 Clones

hKv4.2	CCDS5776.1	Clone of human Kv4.2 α-subunit
hKChIP2b	CCDS41562.1	Clone of human KChIP2b splice variant
hKChIP3a	CCDS2013.1	Clone of human KChIP3a splice variant
hDPP6s	CCDS75684.1	Clone of human DPP6s splice variant
mClover3	Addgene, USA	Green fluorophore mClover3 in pKK vector (Plasmid #105797)
mRuby3	Addgene, USA	Red fluorophore mRuby3 in pKK vector (Plasmid #105795)

If not otherwise stated, clones for expression in CHO and HEK293T cells were inserted in pcDNA3(-) and for cRNA synthesis in pGEM-HE Juel.

3. Methods

3.1 Molecular Biology

3.1.1 Transformation of bacteria

The experimental procedure involved the use of JM109 competent cells, which were obtained from a stock stored at -80°C. The cells were thawed on ice, and 50 µL of competent cells were used for each clone. To this, 0.5-1 µg of plasmid DNA was added, and the mixture was incubated on ice for 30 minutes. The cells were then subjected to heat shock treatment at 42°C for 90 seconds, followed by incubation for 2 minutes on ice.

Following heat shock treatment, 300 µL of super optimal broth (SOC) medium were added to the cells, and they were incubated for 1 hour at 37°C with shaking at 300 RPM. To select for successful transformants, 100 µL of the transformed cells were plated on one quadrant of an LB-agar plate. The plate was then streaked from one quadrant to the next to dilute the colonies for single colonies. This ensured that each colony was derived from a single transformed cell and allowed for the isolation of individual clones for further analysis.

3.1.2 DNA isolation

3.1.2.1 Isolation of plasmid DNA from 7 mL bacterial culture

For Plasmid-DNA extraction a *QIAprep Spin Miniprep Kit* (Qiagen, Hilden) was used. The following used buffers P1, P2, N3, PB, and PE were part of the Miniprep Kit. Centrifugation steps were at done room temperature and at 13.300 RPM unless otherwise stated.

Bacterial colonies were picked with a sterile pipette-tip and transferred into a test tube (Sarstedt, Nümbrecht) containing 7 mL LB + carbenicillin. The tube was then incubated at 37°C overnight at 250 RPM to allow for bacterial growth.

The following day, the bacterial cells were pelleted by centrifugation at 7,000 x g for 5 minutes at 4°C. The supernatant was removed, and the bacterial pellet was resuspended in 250 µL of P1 buffer. Following, 250 µL P2 buffer were added and the mixture was inverted 3-5 times and incubated at room temperature for 5 minutes.

Next, 350 µL of N3 buffer were added to the mixture, immediately inverted, and then centrifuged for 13 minutes at 4°C. Meanwhile, spin column was washed with 500 µL of

PB buffer and centrifuged for 30 seconds. The flow-through was discarded, and 800 µL of the supernatant were added to the column and centrifuged for 60 seconds.
Afterwards, 500 µL of PE buffer were added to the column and centrifuged for 60 seconds. The flow-through was discarded, and 500 µL of PE buffer were added again and centrifuged for 60 seconds. The flow-through was discarded, and the column was centrifuged again to remove excess washing buffer. The column was then transferred to a clean 1.5 mL Eppendorf tube, and 50 µL of RNAse free water was added on the column and incubated for 2 minutes before being centrifuged for 2 minutes.
Finally, the isolated plasmid DNA was quantified through NanoDrop spectrophotometer (Implen, Munich) to determine its concentration and purity.

3.2.2.2 Isolation of plasmid DNA from 50 mL bacterial culture

Higher amounts of plasmid DNA were extracted using *QIAGEN Plasmid Midi Kit* (Qiagen, Hilden). Bacterial colonies were picked with a sterile pipette-tip and were transferred into an Erlenmeyer flask with baffles containing 50 mL LB + carbenicillin. The flask was then incubated at 37°C overnight at 180 RPM to allow for bacterial growth.
The following day plasmid extraction were carried out following the manufacturer instructions.
The DNA was quantified at the end through NanoDrop spectrophotometer to determine its concentration and purity and finally stored at -20°C.

3.2.2.3 Isolation of DNA fragments from agarose gels

For the Gel-Extraction the *QIAquick Gel Extraction Kit* (Qiagen, Hilden) was used.
Separated DNA segments from agarose gel electrophoresis were examined on a UV table and the fragment of interest was cut out of the gel and placed in a 2 mL Eppendorf Tube that had previously been weighed.
Following that, the appropriate quantity of QG buffer was added and processed in accordance with the manufacturer's instructions.

3.1.3 Agarose gel electrophoresis

To identify and analyze DNA fragments, a horizontal agarose gel was prepared by adding 0.7 - 1.5 % weight/volume agarose to 50 mL TBE buffer and heating it until the solution became clear. PeqGreen dye was used to visualize the DNA fragments by intercalating into the DNA and rendering it visible under UV light. The solution was allowed to cool until it reached hand warm temperature, then 3 µL of PeqGreen dye

were added and poured into the gel chamber to solidify. An appropriate quantity of 6x loading buffer were added to the DNA probes (5-15L) and transferred into the gel pockets and one pocket with 5 µL of 1Kb Plus DNA ladder (ThermoFischer). For RNA preparation 5 µL of RNA probe were added together with 2x RNA loading dye and incubated at 70°C or 10 minutes, prior to adding it into the gel pocket. 3.5 µL of *RiboRuler High Range RNA Ladder* (ThermoFischer) were added in one gel pocket. Gel electrophoresis was conducted with 110 V, 80 mA, and 3-6 W to separate the DNA fragments by size.

3.1.4 DNA Modification

3.1.4.1 Enzymatic restriction digestion

To perform DNA restriction digestion on plasmid DNA or PCR fragments, the required amount of DNA was taken and mixed with the appropriate restriction enzymes and 10x buffer according to the manufacturer's instructions. The resulting mixture was then incubated at a temperature of 37°C for 15-60 minutes. In the case of digestions with two restriction enzymes, the same procedure was pursued, but the total volume of enzymes did not exceed 10% of the total reaction volume.

3.1.4.2 Site directed mutagenesis

To perform amino acid substitutions, deletions, or insertions, the *Q5® Site-Directed Mutagenesis Kit* (New England Biolabs) was utilized. The primers used in this process were designed with 5' ends annealing back-to-back by employing the online tool provided by the manufacturer (NEBaseChanger.neb.com). All mutagenesis procedures were conducted in accordance with the manufacturer's instructions.

3.1.4.3 Construction of epitope-tagged proteins

Primer design and initial PCR

Firstly, a PCR was performed to obtain only the cDNA of the desired fluorophore and protein. For optimal expression, forward primers for Kv4.2 and KChIP2b were designed with an optimal Kozak consensus sequence located just before the translation start codon. Additionally, an EcoRI motif was incorporated prior to the Kozak sequence for easy integration into the pGEM-HEJuel vector. To allow for translation into the linker and fluorophore, reverse primers for Kv4.2 and KChIP2b were designed to exclude the stop codon (TGA/TAG/TAA). Reverse primers were designed to incorporate a flexible

linker of Gly-Gly-Ser-Gly-Gly-Ser-Gly and an additional BamHI recognition site within the linker sequence to facilitate easy exchange of either the fluorophore or the protein. Furthermore, this recognition site was used to verify the correct cloning. Additionally, the fluorophore forward primers were designed to overlap with the linker-sequence of the reverse primer, while reverse primers for fluorophores were designed to have a HindIII recognition site for easy integration into the pGEM-HE Juel vector (Figure 3.1).

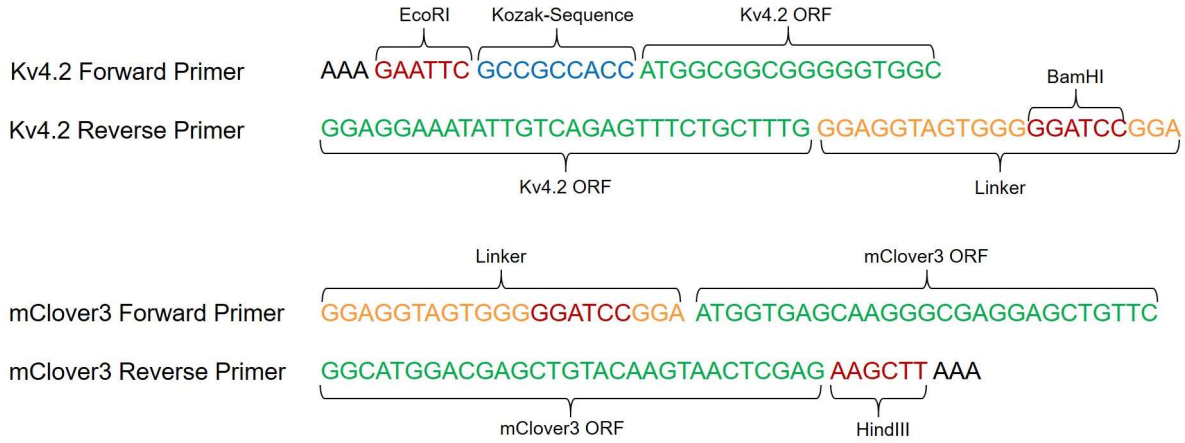

Figure 3.1: **Example of a primer design for construction of epitope-tagged proteins via recombinant PCR.**
Forward primers were used as seen in this figure whereas for the reverse primers their reverse-complementary sequence was used.

For the initial PCR the *Phusion High-Fidelity PCR Kit* (New England Biolabs) was used. The following reagents were added and the following PCR protocol was used:

Component	50 µL Reaction
Template DNA	50 ng
5x Phusion HF Buffer	10 µL
10 µM Forward Primer	2.5 µL
10 µM Reverse Primer	2.5 µL
10 mM dNTP's	1 µL
50 mM MgCl2	3 µL
Phusion DNA Polymerase	0.5 µL
RNAse free water	To 50 µL

Step	Temperature [°C]	Time	Number of Cycles
Initial denaturation	98	30 Seconds	1
Denaturation	98	10 Seconds	
Annealing	70	20 Seconds	30
Elongation	72	1 Minute	
Final elongation	72	10 Minutes	1
Hold	4	∞	

Following the completion of the PCR, the products were analyzed and separated from any by-products by running them on an agarose gel electrophoresis. The desired band was then excised and subjected to gel extraction. The Kv4.2 product was approximately 2000 base pairs in size, while KChIP2b, mClover3, and mRuby3 products were approximately 800 base pairs in size.

The concentration of the PCR products ranged from 20-60 ng/µL.

Recombinant PCR

To combine the protein with its corresponding fluorophore, an overlap PCR was performed to generate fusion templates, which were subsequently amplified in a second PCR.

For the overlap PCR, the following reagents were combined in a PCR tube.

The used volume of the PCR products depended on concentration and size. Here, an excess amount of Kv4.2 PCR product was used.

Component	50 µL Reaction
Kv4.2 PCR product	6 µL
mClover3 PCR product	3 µL
5x Phusion HF Buffer	10 µL
10 mM dNTP's	1 µL
50 mM $MgCl_2$	3 µL
Phusion DNA Polymerase	0.5 µL
H_2O	To 50 µL

Step	Temperature [°C]	Time	Number of Cycles
Initial denaturation	98	30 Seconds	1
Denaturation	98	10 Seconds	
Annealing	70	30 Seconds	10
Elongation	72	60 Seconds	
Final elongation	72	5 Minutes	1
Hold	4	∞	

Following the first PCR, 2.5 µL (0.5 µM) of Kv4.2 forward primer and mClover3 reverse primer were added to the PCR tube, and the tube was placed back into the cycler for the amplification PCR.

Step	Temperature [°C]	Time	Number of Cycles
Initial denaturation	98	30 Seconds	1
Denaturation	98	10 Seconds	
Annealing	70	30 Seconds	30
Elongation	72	90 Seconds	
Final elongation	72	10 Minutes	1
Hold	4	∞	

Following the completion of the PCR, the products were analyzed and separated from any by-products by running them on an agarose gel electrophoresis. The desired band was then excised and subjected to gel extraction. The Kv4.2-mClover3 product was approximately 2800 base pairs in size, while KChIP2b-mRuby3 1600 base pairs in size.

Integration in pGEM-HE Juel vector

The fusion constructs that were obtained earlier were inserted into the pGEM-HE Juel vector through a process that involved digesting both the vector and PCR products with EcoRI and HindIII. The resulting products were purified using the *QIAquick PCR Purification Kit* (Qiagen) according to the manufacturer's instructions, and the concentration of both the vector and insert were determined through NanoDrop spectrophotometer. The vector and insert were then ligated using the *Quick Ligation Kit* (New England Biolabs), and the following reagents were combined in a PCR tube.

Component	10 µL Reaction
Quickligase buffer	10 µL
Quickligase	1 µL
pGEM-HEJuel (vector)	2 µL
Kv4.2-mClover3 (insert)	7 µL

The reaction mixture was gently mixed and incubated at room temperature for 5 minutes before being transformed into competent cells, following the previously described protocol. Colonies were selected and subjected to a Miniprep as described before. A control digestion with BamHI was performed to confirm the presence of the correct inserts. With cutting sites located in the linker region and 5' upstream of the translation region, positive constructs were expected to yield two bands of approximately 2000 bp and 3600 bp for Kv4.2-mClover3 and 800 bp and 3600 bp for Kchip2b-mRuby3. The positive clones were subsequently subjected to further sequencing to confirm the correct insertion.

Cloning in pcDNA3(-):

To facilitate the expression of the fusion proteins and fluorophores mRuby3 and mClover3 in eukaryotic cells, they were cloned into the pcDNA3(-) vector. To accomplish this, the fusion constructs were subjected to PCR amplification with forward primers containing an overhang with an EcoRI recognition site and reverse primers containing an overhang with a HindIII recognition site. The PCR amplification was carried out by combining the following reagents in a PCR tube and the following PCR protocol was used.

Component	50 µL Reaction
Template DNA	50 ng
5x Phusion HF Buffer	10 µL
10 µM Forward Primer	2.5 µL
10 µM Reverse Primer	2.5 µL
10 mM dNTP's	1.5 µL
50 mM $MgCl_2$	3 µL
Phusion DNA Polymerase	0.5 µL
H_2O	To 50 µL

Step	Temperature [°C]	Time	Number of Cycles
Initial denaturation	98	30 Seconds	1
Denaturation	98	10 Seconds	
Annealing	63	20 Seconds	35
Elongation	72	30 Seconds	
Final elongation	72	10 Minutes	1
Hold	4	∞	

After PCR amplification, the products were purified with the *QIAquick PCR Purification Kit* (Qiagen) according to the manufacturer's instructions and were eluted in 44 µL RNAse free water. Next, 5 µL of 10x Cutsmart buffer, 2 µL of HindIII-HF and 2 µL of EcoRI-HF were added to the purified products, and they were incubated at 37°C for 1 hour. Simultaneously, the pcDNA3(-) vector was digested by combining 4 µg of the vector, 1 µL of HindIII-HF, 1 µL of EcoRI-HF, 2 µL of 10x Cutsmart buffer, and RNAse free water to a total volume of 20 µL. The products were then separated from any by-products by running them on an agarose gel electrophoresis. The desired band was excised and subjected to gel extraction, and DNA concentration was determined through NanoDrop spectrophotometer.

The purified vector and insert were then ligated together using the *Quick Ligation Kit*. For each construct, 10 µL of Quick ligase reaction buffer (2x), 1 µL of Quick Ligase, 8 µL of insert, and 1 µL of vector were mixed gently and incubated at room temperature for 5 minutes. 5 µL of the mixture was used for transformation, and the resulting clones were verified by control digestion and sequencing.

3.1.5 DNA sequencing

Sequencing was carried out for each clone to ensure that clones were all correctly assembled. This was accomplished by using the chain termination-based Sanger technique: A single-stranded DNA template, a DNA primer, a DNA polymerase, regular dNTPs, and modified di-deoxynucleotide triphosphates (ddNTPs) are used in the traditional chain termination technique. These altered nucleotides lack of the 3'-OH group, which is necessary to form a phosphodiester link between two nucleotides and prevents DNA strand elongation. When a modified ddNTP is inserted during DNA replication, the DNA polymerase enzyme is unable to incorporate additional normal dNTPs, which leads to the termination of the reaction. The fluorescent tags on the modified ddNTPs enable automated sequencing machines to identify them. The following chemicals from the *Applied Biosystems™ Sanger Sequencing Kit* (ThermoFischer) and PCR protocol were used for the reaction:

Component	10 µL Reaction
Plasmid DNA (0.1-0.5 µg/µL)	1 µL
Sequencing-buffer	2 µL
Sequencing primer (50-100 pM)	0.5 µL
H_2O	5.5 µL
BDT (Enzyme polymerase, tagged Nucleotides)	1 µL

Step	Temperature [°C]	Time	Number of Cycles
Initial denaturation	96	5 Minutes	1
Denaturation	96	30 Seconds	
Annealing	55	15 Seconds	29
Elongation	60	4 Minutes	
Final elongation	72	10 Minutes	1
Hold	4	∞	

Once the PCR procedure was complete, the DNA fragments need to be prepared for the sequencer. This was achieved by using a sodium acetate precipitation. To do this, 10 µL of the DNA sample were mixed with 10 µL of water, 2 µL of 3M sodium acetate, and 50 µL ethanol (100%). The resulting mixture was transferred into a 1.5 mL

Eppendorf tube and centrifuged at 13.300 RPM for 25 minutes at 4°C. The supernatant was then carefully removed and 100 µL of 70% ethanol were added to the tube. The mixture was briefly vortexed and centrifuged again at 13.300 RPM for 25 minutes at 4°C. The supernatant was carefully removed and the tube is placed in a vacuum concentrator for 10-15 minutes until all residual ethanol has been evaporated. Finally, 20 µL of HIDI-Formamid were added to the tube and briefly vortexed. The resulting samples were stored at -20°C in the dark until they were ready to be sequenced. Samples were given to the human genetics institute and sequenced. The sequenced samples were then analyzed by using the program Unipro UGENE (v.44).

3.1.6 *In vitro* cRNA synthesis

In order to inject the Kv4.2 channel and its β-subunits into *Xenopus* oocytes, plasmid DNA in pGEM-HEJuel vector must first be transcribed into RNA.

Linearization

Initially, the template DNA was linearized by incubating 2 µg of template DNA with 5 µL 10x Cutsmart-Buffer, 1.5 µL NotI or SalI, and 50 µL RNAse free water at +37°C for 15-30 minutes. A sample of 5 µL were taken from the reaction mixture and subjected to agarose gel electrophoresis to confirm that the template DNA has been linearized. Next, 5 µL of 3M sodium acetate and 125 µL of 100% ethanol were added to the remaining 45 µL of the reaction mixture, which was then incubated at -20°C for 30 minutes. The resulting mixture was centrifuged at 14,000 RPM for 20 minutes at 4°C, and the supernatant was carefully discarded. Then, 1 mL of 70% ethanol was added to the remaining pellet, shaken gently, and centrifuged again at 4°C for 10 minutes. The supernatant was carefully discarded again and placed into a vacuum concentrator for 10-15 minutes until all residual liquid evaporated.

Capping

The *T7 RiboMAX*™ (Promega, Walldorf) was used to synthesize cRNA. The amount of GTP in the random nucleotide mix (rNTP) were decreased, and *Ribo m^7G Cap Analog* (Promega) were later added to the mixture to improve the stability of cRNA.
From the Kit a nucleotide master mix were made by using 50 µL ATP/CTP/UTP and 6 µL GTP (20 mM) and 44 µL RNAse free water.

The following reagents were added to the previously used Eppendorf tube:

Component	Volume
RNAse free water	17 µL
rNTP's	15 µL
T7 buffer	10 µL
T7 enzyme mix	5 µL
Ribo m^7G Cap Analog (40 mM)	3.75 µL

The mixture was thoroughly shaken before being quickly centrifuged and incubated at 37°C for 4-5 hours. 4 µL of RQ1-DNAse were then added and incubated at 37°C for 15 Minutes. Then, 46 µL RNAse free water were added to the mixture.

RNA isolation

All following centrifugation steps have been carried out at 4°C and at 14.000 RPM.

The synthesized RNA was extracted and purified by adding 100 µL of Roti-Phenol to the solution. The mixture was vortexed for 30 seconds and centrifuged for 2 minutes. The top phase was transferred to a new 1.5 mL Eppendorf tube, and the previous step was repeated. After transferring the top layer into a new Eppendorf tube, 100 µL of chloroform were added. The solution was vortexed for 30 seconds and centrifuged for 2 minutes. The top layer was carefully transferred to a new Eppendorf tube. Subsequently, 10 µL of sodium acetate (3M) and 250 µL of ethanol (100%) were added. The solution was incubated on ice for 5 minutes to precipitate the RNA. The mixture was then centrifuged for 10 minutes, and the supernatant was discarded. Following this, 1 mL of ethanol (70%) was added to the remaining pellet. The solution was inverted several times and centrifuged for 5 minutes. The supernatant was carefully discarded of and the remaining pellet was dried in a vacuum concentrator for 10-15 minutes until all visible liquid had evaporated and the pellet became slightly clear. Finally, 100 µL of RNAse free water were added to the pellet and mixed until the pellet dissolved.

Additionally, some RNA extractions were performed using the *Monarch RNA Cleanup Kit (500 µg)* (New England Biolabs). After addition and incubation of the synthesized RNA mixture with RQ1-DNAse the mixture (without the addition of 46 µL of RNAse free water) was purified according to the manufacturer's instructions.

The concentration was measured through NanoDrop spectrophotometer and synthesized RNA was subjected to agarose gel electrophoresis.

3.2 Cell culture

3.2.1 Cell culture routine and poly-L-lysine coating

Chinese hamster ovary cells (CHO) and human embryonic kidney cells (HEK293T) were used as heterologous expression systems for electrophysiological recordings and fluorescence imaging. The CHO cells were cultured in MEM-alpha medium, while DMEM/F-12 was used for HEK cells. Both media were supplemented with 10% fetal calf serum and 1% penicillin-streptomycin-glutamine. The cells were cultivated in 75 mL cell culture flasks containing 60 mL medium at 37°C, 5% CO2 and 95% humidity in an incubator. The cultures were split 2-3 times per week depending on confluency.
To split the CHO cells, the old medium was first discarded, and then 2 mL of 0.05% trypsin-EDTA was added and incubated for 3 minutes at 37°C. After that, 3 mL of fresh medium was added, and the cells were separated by pipetting several times with a 10 mL serological pipette. The cells were then examined under a microscope to ensure proper separation and counted using a hemocytometer. To continue cell culture, $4x10^4$ cells/mL were transferred into a new culture flask and returned to the incubator. To prepare for additional experiments, the appropriate cell density of CHO cells was seeded onto a 35 mm cell culture dish and then placed in the incubator for further processing.

For HEK cells, the old medium was first discarded, and washed gently with 3 mL of PBS. After removing the PBS, 1.5 mL of 0.05% trypsin-EDTA was added and incubated for 2-3 minutes at 37°C. 3 mL of new medium was added and cells were treated similar as mentioned before.
In some experiments, cells needed to be placed on a glass cover slip coated with low molecular weight poly-L-lysine. To achieve this, 10mm glass cover slips were immersed in a 100 µg/mL poly-L-lysine solution for 30 minutes. The solution was then removed and the cover slips were allowed to air dry for 30 minutes.

3.2.2 Transient transfection

For electrophysiological experiments, $1x10^5$ - $1x10^4$ cells were grown on a 35 cell culture dish together with three glass cover slips which were covered in poly-L-lysine and transfected the following day using *Lipofectamine™ 2000 Transfection Reagent* (ThermoFischer). For each 35 mm culture dish, 3-5 µg of DNA and 3-5 µL of Lipofectamine were used. The Lipofectamine and DNA were diluted in 100 µL OPTI-

MEM and incubated at room temperature for 5 minutes. They were then mixed together, briefly vortexed, and incubated for an additional 30 minutes at room temperature. Next, 200 µL of the transfection reagent were added to the cells and incubated at 37°C for 3-5 hours. After incubation, the medium was replaced with fresh medium and incubated for 2-4 days before recording.

To conduct fluorescence experiments, either 1 $x10^5$ - $1x10^4$ cells were grown on 35 cell culture dishes or $1x10^4$ - $1x10^3$ cells were cultivated on 4 well µ-slides (Ibidi, Gräfelfing). The transfection process was the same as described before, using 0.5-3 µg of DNA and 2.5-4 µL of Lipofectamine. For the µ-slides, 50 µL of the transfection reagent were added to each well.

3.2.3 *Xenopus* oocyte preparation and cRNA injection

To obtain oocytes for electrophysiological experiments, female *Xenopus laevis* frogs were anesthetized in a Tricain solution (1.2 mg/L in tap water) for 10 - 20 minutes. Ovary lobes were surgically removed and placed in OR1 + 50 µg/mL gentamycin solution. After wound suturing the frog was placed back into fresh water without Tricain. The lobes were manually dissected into smaller string-like pieces and incubated in Ca^{2+}-free OR2 solution containing collagenase II (1.3 mg/ml) on a horizontal shaker at 100 RPM for 3-4 hours. After several wash steps with OR2 solution, the final wash was performed in OR1 with gentamicin solution, and the oocytes were transferred to a 20 cm culture dish. Unhealthy and oocytes other than stage V-VI were selected from the dish and incubated at +16 °C until RNA injection.

For injection, healthy Stage V-VI oocytes were selected and placed in OR2. Using the Nanoliter 2000 (World Precicion Instruments, Friedberg), each oocyte was injected with 50 nl and a total RNA injection of 1-20 ng was used. For TEVC recordings, *Xenopus* oocytes were injected with 5 ng wild type or epitope-tagged Kv4.2 cRNA. For Kv4.2/KChIP2 channel complexes *Xenopus* oocytes were injected with 1 ng wild type or epitope-tagged Kv4.2 together with 4 ng wild type or epitope-tagged KChIP2.

For inside-out recordings, *Xenopus* oocytes were injected with 4 ng Kv4.2 and respectively 8 ng of β-subunits DPP6 and KChIP to a total of 12 ng cRNA for Kv4.2/DPP and 18 ng cRNA for Kv4.2/DPP6/KChIP. Injected oocytes were transferred to 35 mm cell culture dishes with 5 mL OR1 + 50 µg/mL gentamicin and incubated at +16 °C for at least 2 days.

3.3 Electrophysiology

In the 1950's Kenneth Cole and Howard Curtis and independently Alan Hodgkin ad Andrew Huxley studied the physiology of ionic currents across the giant squid axon. During their research, they developed a technique, which involved the insertion of a pair of mini electrodes into the cell. One electrode monitors the voltage across the cell membrane while the other electrode injects a current to adjust the desired membrane potential, which can then be recorded. This allows a precise measurement and control of the membrane potential, enabling researchers to study ion channels responsible for the generation of action potentials[44,45]. This method later became the basis of the two-electrode voltage clamp (TEVC) technique, which has been refined and widely adopted to study large cells like *Xenopus* oocytes[46]. (Figure 3.2 A & B)

In the 1970's Bert Sakmann and Erwin Neher developed and refined the patch clamp technique as a means to study ion channels on biological membranes[47].

This versatile tool has proven useful for understanding ion channel behavior, with currents ranging from picoamperes to nanoamperes. The patch clamp technique involves placing a glass micropipette electrode against the cell membrane and applying gentle suction to establish a high resistance seal of several GΩ between the pipette and the membrane. This initial configuration is known as the cell-attached configuration, which isolates a small patch of the membrane from its surroundings.

From the cell-attached configuration, different variations can be established. By quickly excising the membrane, the inside-out configuration is achieved, exposing the intracellular side of the membrane to its surrounding environment. This allows for precise control and perfusion of solutions to study the effects on the ion channels. (Figure 3.2 C & D)

Alternatively, by applying suction to rupture the membrane, a direct electrical connection is formed between the pipette and the cell's cytoplasm, resulting in the whole-cell configuration. In this configuration, the entire cellular interior is accessible for investigation. Lastly, if an already ruptured membrane is excised, an outside-out patch is obtained, where the extracellular side of the membrane is exposed[48].

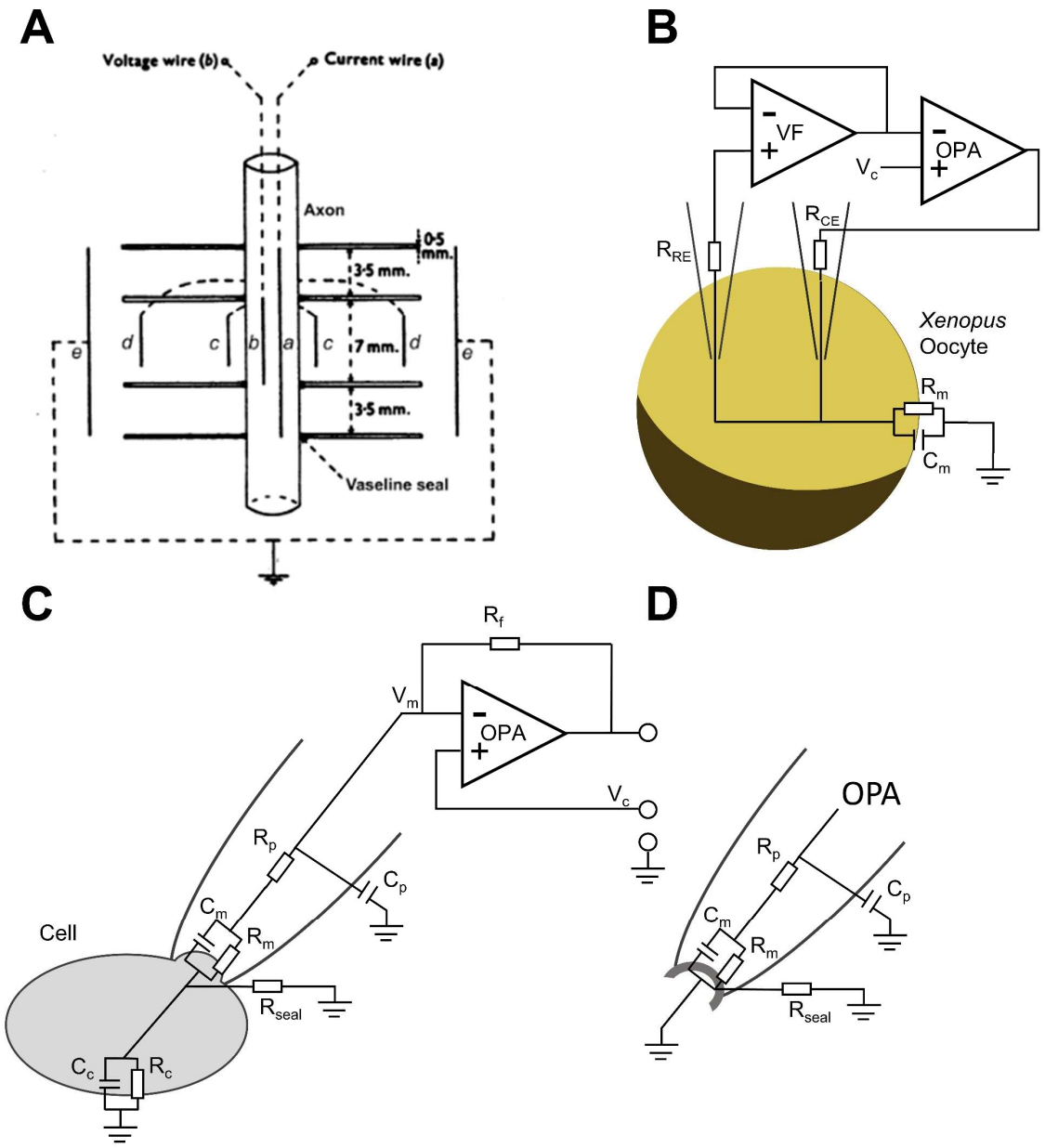

Figure 3.2: **Principle of voltage clamp**.
The two-electrode voltage clamp technique involves the use of two intracellular electrodes. One electrode, known as the reference electrode (R_{FE}), is responsible for monitoring the membrane potential (V_m) of the cell. It is connected to a voltage follower (VF), which serves as a buffer to isolate the circuit and has a high impedance. The output of the VF is connected to an operational amplifier (OPA). The VF ensures that its output matches the Vm measured by the reference electrode. The OPA then compares this output with the commanding potential (V_C). If there is a difference between V_m and V_C, the OPA generates an output current that is sent to the current electrode (R_{CE}). This current injection from the OPA to the R_{CE} helps to clamp the membrane potential to the commanded potential (V_C). Subsequently, this current injection can be recorded for further analysis[46]. The patch clamp technique bases on the same principle of voltage clamp, but in the absence of the voltage follower and using one patching electrode.
(**A**) Modified diagram from Hodgkin, Huxley and Katz showing the arrangement of internal and external electrodes a-e from two-electrode voltage clamp experiment in squid giant axon[45]. (**B**) Simplified circuit diagram of two-electrode voltage clamp in *Xenopus* oocytes. (**C**)Simplified circuit diagram of cell-attached configuration and inside-out configuration (**D**). R_{Ce} : current electrode, R_{RE} : reference electrode, R_f : feedback resistance, R_p : pipette resistance, R_m : membrane resistance, R_c : cell resistance, R_{seal} : seal resistance, C_p : pipette capacitance, C_m : membrane capacitance, C_c : cell capacitance, V_c : command potential, V_m : membrane potential, VF : voltage follower, OPA: operational amplifier.

All recordings were performed at room temperature (20-25°C). Functionality of fusion constructs were tested in *Xenopus* oocytes using two-electrode voltage clamp.
Electrophysiological experiments were performed using the patch clamp method in cell-attached configuration (CA) and inside-out configuration (IO) in HEK293T cells as well as *Xenopus* oocytes.

3.2.1 Two-electrode voltage clamp (TEVC) recording from *Xenopus* oocytes

The two-electrode voltage clamp recording station was mounted on a metal plate and the electrode holders were fastened to mechanical micromanipulators (Märzhäuser, Wetzlar). For visual monitoring, a binocular (*Stemi DV4spot*, Zeiss, Jena) was positioned above the recording chamber. Oocyte superfusion was achieved using a gravity-driven perfusion system. Microelectrodes were made from borosilicate glass (*GB150TF-8P*, Science Products, Hofheim) that was pulled with a vertical electrode puller (*L/M-3P-A*, List-Medical) and manually broken under a microscope. The pipettes were then filled with 3M KCl and inserted into the electrode holders. The electrode resistance varied between 0.1 and 0.2 MΩ. The electrode itself was a silver wire that was electrochemically chlorinated using 3M KCl (*ACl-01*, NPI, Tamm), while the bath electrode consisted of a silver wire with an AgCl pellet. Bath electrodes were placed in a separate chamber filled with 3M KCl and an agar bridge (2%, 3M KCl) was connecting the chamber with the main chamber. Recording signals were amplified by using a Turbo tec-03x amplifier (NPI, Tamm) and digitalized by an AD/DA converter (*IntruTECH LIH 8+8*, HEKA, Lambrecht) with a sampling frequency of 1 - 4 kHz.

3.2.2 *Xenopus* oocyte macropatch recordings

For *Xenopus* macropatch recording, a light-reflecting microscope (*Axioskop 2 FS*, Zeiss, Jena) was utilized. Thick-walled borosilicate glass pipettes (GB150-8P, Science Products, Hofheim) were pulled by a horizontal puller (*DMZ-puller*, Zeitz, Augsburg) to create an opening >10 µm, and the pipette tips were heat-polished (*MF-900*, Narishige, Japan) to the desired size. The tip resistance ranged from 0.8-2 MΩ, and the electrodes were controlled by a micromanipulator (*SM-1*, Luigs & Neumann, Ratingen). Recordings were made using an EPC10 (HEKA, Lambrecht) and recorded signals were filtered with a 10 kHz Bessel filter.
Macropatch superfusion was accomplished using a peristaltic pump (*Minipuls3*, Gilson, Berlin) and a valve-controlling unit (*ValvebankII*, Science Products, Hofheim). Excess liquid was drained using the same peristaltic pump, with the connection tubes reversed

to achieve the same inflow speed as the outflow speed. Ag/AgCl electrodes are made similar as mentioned before. The bath electrode was placed in a separate chamber filled with 1M KCl and both chambers were connected using an agar bridge (2%, 1M KCl).

The experimental procedure involved placing injected *Xenopus* oocytes first in a 35 mm cell culture dish containing 5 mL of oocyte shrinking buffer for 5-10 minutes until the vitelline layer was visible. The vitelline layer was then carefully removed using fine forceps (*Dumont #5SF*, Fine Science Tools, Heidelberg). After peeling the oocyte, it was transferred into a 35 mm cell culture dish filled with Ca^{2+}-free internal solution to wash away residual oocyte shrinking buffer. Subsequently, the oocyte was transferred to the recording chamber filled with Ca^{2+}-free internal solution. Pipettes were filled with external solution and placed in the electrode holder to achieve macro patches (inside-out configuration) by forming a GΩ seal and patch excision.

3.2.3 HEK293T patch clamp recordings

To record from HEK cells, an inverted microscope (*Axiovert 135*, Zeiss, Jena) was used, with a Hg-UV lamp (*HBO 50*, Zeiss, Jena) as the light source, and GFP and dsRED filter cubes to identify successfully transfected cells. Transiently transfected HEK cells expressed epitope-tagged constructs, which served as a marker. The microscope stage has an opening that can accommodate a 35mm cell culture dish. Thick-walled borosilicate glass pipettes were pulled using a horizontal pipette puller to create an opening of around 5-10 µm for the pipettes. The tip of each pipette was optically inspected and heat-polished with a microforge to the desired size. Depending on the membrane expression levels, the pipette tip resistance ranged from 1.5-3.5 MΩ. The pipettes were then filled with HEK293T external solution and placed in an electrode holder. The electrode itself was a silver wire that was electrochemically chlorinated using 3M KCl, while the bath electrode consisted of a silver wire with an Ag/AgCl pellet. Electrodes were controlled using an electric micromanipulator (*Patchman*, Eppendorf, Hamburg). Inside-out patch superfusion was accomplished using a peristaltic pump and a valve-controlling unit, with excess solution drained using a suction pump.

In the experimental procedure, a cover slip was first removed from the 35 mm cell culture dish and washed in a 35 mm dish with 5 mL of bath solution to remove any residual cultivating medium. The cleaned cover slip was then transferred to a recording chamber filled with bath solution and gently pressed in the center of the dish to hold it

in place. Pipettes were carefully placed near the cell membrane of the cells to form a GΩ seal. At this point, recordings were made in the cell-attached configuration before patch excision, or the patch was immediately excised and perfused with Ca^{2+}-free internal solution.

All recorded signals were filtered with a 10 kHz Bessel filter. The analog signals from the EPC9 were digitized with an ITC16 AD/DA converter (HEKA, Lambrecht) and sampled at frequencies ranging from 4-50 kHz.

3.3.4 Stimulation protocols and data analysis

For programing and recording of stimulation protocols the Software Patchmaster (v.2x91, HEKA, Lambrecht) was used. Further analysis was made by using Fitmaster (v.2x91, HEKA, Lambrecht), Microsoft Excel 2013 (Microsoft, USA), Kaleidagraph (v.4 and v.5, Synergy Software, USA) and GraphPad Prism (v.9.5.1, GraphPad, USA).

3.3.4.1 Macroscopic inactivation kinetics

All recordings used V_m = -80 mV as holding potential.

To investigate the decay kinetics of the currents, a depolarizing pulse at +40 mV was preceded by a hyperpolarizing pre-pulse at -100 mV for 1 second, with a 5-second interval between each pulse protocol at holding potential. A minimum of 3 repeats were obtained in the cell-attached configuration. In the inside-out configuration, a minimum of 5 repeats were recorded until a steady peak current and inactivation kinetic were observed, with a maximum of 20 repeats. To refine the data and eliminate any potential artifacts, a separate second pulse protocol was applied with a hypopolarizing step at -15 mV for 1 second and a depolarizing step to +40 mV for 2 seconds, with a 5-second interval at its holding potential between each protocol. Both protocols shared the same sampling frequency, and the second trace was subtracted from the first trace to reduce endogenous channel current and leak current.

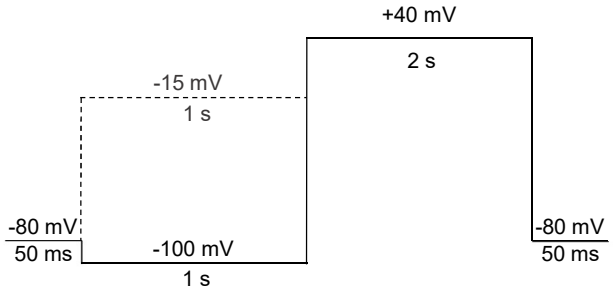

Figure 3.3: **Stimulation protocol for current inactivation kinetics.**
Initially, the membrane potential was set to -100 mV to ensure maximal channel availability following a depolarizing pulse to +40 mV for two seconds. A second stimulation protocol was conducted, where the prepulse is set to -15 mV to inactivate all availability Kv4.2 channel complexes. The second recording was subtracted from the first recording to reduce endogenous channel current and leak current.

The current decay was fitted using a double exponential function:

$$I = A_0 + A_1 e^{-\frac{t}{\tau_1}} + A_2 e^{-\frac{t}{\tau_2}}$$

I : Current

A : Relative amplitude

t : Time

τ : Time constant

3.3.4.2 Recovery from inactivation

Here, a double pulse protocol was utilized to determine the fractional recovery from inactivation.

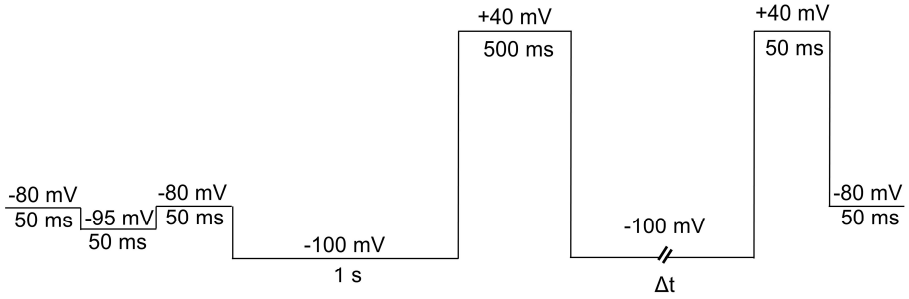

Figure 3.4: **Stimulation protocol for recovery from inactivation**.
Initially, the membrane potential was pulsed from the holding potential to -95 mV, which is the potassium reversal potential, therefore showing only leak current. This leak current was then subtracted offline from test pulse and control pulse. After that, a 1-second prepulse was administered to -100 mV, followed by a depolarization step to +40 mV for 500 ms ($I_{control}$). A hyperpolarizing step was applied to -100 mV with varying time intervals to allow channels to recover, and a second pulse to +40 mV for 50 ms was performed to determine the availability of the channels (I_{test}). The first interpulse interval ranged from 1.25 ms to 5 ms and was incremented by a factor of 2.

Test and control pulse were leak subtracted by using the mean current from the -95 mV pulse and calculated as followed:

$$\mathrm{I}_{\mathrm{leak}(+40)} = \frac{\bar{\mathrm{I}}_{-95\ \mathrm{mV}}}{-95} * 40$$

$\mathrm{I}_{\mathrm{leak}(+40)}$: calculated leak current at +40

$\bar{\mathrm{I}}_{-95\ \mathrm{mV}}$: mean current at -95 mV

After leak subtraction of both pulses, the test pulse was normalized to its control pulse ($I_{test}/I_{control}$). The normalized current amplitudes were graphed against the interpulse interval and data points were analyzed using an open single exponential function:

$$\frac{I_{test}}{I_{control}} = \left(A_{max} - A_{offset}\right) - e^{\left(-\frac{t}{\tau_{rec}}\right)} + A_{offset}$$

A_{max} : normalized maximal amplitude

A_{offset} : normalized offset amplitude

t : time

τ_{rec} : time constant for recovery

Data points were then corrected by subtracting A_{offset} and divided by (A_{max}-A_{offset}).

3.3.4.3 Voltage dependence of steady-state inactivation

A double pulse protocol was utilized to determine the voltage dependence of steady-state inactivation.

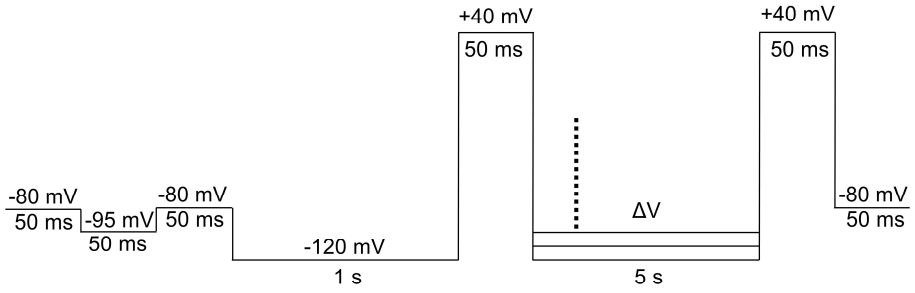

Figure 3.5: **Stimulation protocol for voltage dependence of steady-state inactivation**.
The first step was to pulse the membrane potential from the holding potential to -95 mV, which is the reversal potential of potassium, to subtract leak currents from the test and control pulse. Next, a 1-second prepulse was applied to -120 mV, followed by a depolarization step to +40 mV ($I_{control}$). A conditioning pulse was then administered for 5 seconds, starting at -120 mV and increasing by +10 mV per repeat. Next, a second depolarization step at +40 mV for 50 ms was performed (I_{test}). The prepulse and conditioning pulse were adjusted depending on the patch configuration and channel complex expressed, ranging from -120 mV to -100 mV.

Test and control pulse were leak subtracted by using the mean current from the -95 mV pulse a calculated as described before.

After leak subtraction of both pulses, the test pulse was normalized to its control pulse ($I_{test}/I_{control}$). The normalized current amplitudes were graphed against the conditioning pulse voltage and data points were analyzed using a single open Boltzmann function:

$$\frac{I_{test}}{I_{control}} = \frac{(A_{max} - A_{offset})}{1 + e^{\left(\frac{V_{m-V_{1/2}}}{k}\right)}} + A_{offset}$$

A_{max} : Normalized maximal amplitude

A_{offset} : Normalized offset amplitude

V_m : Membrane potential

$V_{1/2}$: Voltage of half maximal inactivation

k : Slope factor

Data points were then corrected by subtracting A_{offset} and divided by (A_{max}-A_{offset}).

3.4 Fluorescence microscopy

Fluorescence is a phenomenon in which a substance absorbs light at a certain wavelength and then emits light at a longer wavelength. Fluorescence is often used to study the distribution and behavior of molecules within cells. Fluorescent probes, such as fluorescent proteins and dyes, can be introduced into cells and used to label specific structures or the molecules themselves. These labeled structures can then be visualized using fluorescence microscopy.

When two fluorescent proteins are in close proximity (1-10 nm) a physical phenomenon called Förster resonance energy transfer (FRET) occurs. FRET is a way to measure the distance between the donor and acceptor molecules with high spatial and temporal resolution. When a molecule is excited by light, it enters an excited state and can either emit light (fluorescence) or transfer its energy to a nearby molecule. In FRET, the excited state energy is transferred from one molecule (the donor) to another (the acceptor) through non-radiative dipole-dipole coupling. The FRET efficiency depends on the spectral overlap between the donor emission and the acceptor absorption spectra as well as the distance between both fluorophores.

In this study, mClover3 and mRuby3 were chosen as a FRET pair to determine protein – protein interaction between Kv4.2 and KChIP.

3.4.1 Fluorescence imaging with the PolychromeV

The imaging system utilized in the study consisted of a light-reflecting microscope (*Axioskop 2 FS*, Zeiss, Jena) microscope equipped with a monochromator (*PolychromeV*, Till Photonics, USA) as light source. Image capture was performed using a CCD camera (*Ixon+EM*, Andor Oxford Instruments,United Kingdom) that was mounted on top of the microscope. Light source and camera were controlled by open source program Micromanager (v. 1.4.22). The following filtercubes were used:

mClover3 (donor)	483/25 H bandpass	H507 LPXR flat beam splitter	524/32 H bandpass
mRuby3 (acceptor)	560/32 H bandpass	H581 LP beam splitter	607/40 H bandpass
FRET	483/25 H bandpass	H507 LPXR flat beam splitter	607/40 H bandpass

3.4.1.1 Photostability and bleedthrough values

Photostability

CHO cells were transfected with 0.5 µg mClover3 or mRuby3 cDNA. Cells were incubated for 48 h after transfection. Prior to the measurements cultivating medium was switched to imaging solution +5 mM glucose. Cells were bleached at λ = 488 nm for mClover3 and λ = 560 nm for mRuby3 for 600 seconds and pictures were taken every 5 seconds. The mean grey value for every cell within the region of interest was calculated for each time point and normalized to the initial intensity. Half-life time $t_{1/2}$ were determined by one phase decay.

$$Int(t) = e^{\left(-\frac{t}{\tau}\right)}$$

Int : Intensity

t : time

τ : time constant

Determination of bleedthrough values

Bleedthrough values were determined using the method described by Zal & Gascoigne[49].

$$a = \frac{Int_{FRET(mRuby3)}}{Int_{acceptor(mRuby3)}}$$

$$b = \frac{Int_{donor(mRuby3)}}{Int_{acceptor(mRuby3)}}$$

$$c = \frac{Int_{acceptor(mClover3)}}{Int_{donor(mClover3)}}$$

$$d = \frac{Int_{FRET(mClover3)}}{Int_{donor(mClover3)}}$$

$Int_{FRET(mRuby3)}$: Intensity of mRuby3 with FRET-Filtercube

$Int_{acceptor(mRuby3)}$: Intensity of mRuby3 with mRuby3-Filtercube

$Int_{donor(mRuby3)}$: Intensity of mRuby3 with mClover3-Filtercube

$Int_{acceptor(mClover3)}$: Intensity of mClover3 with mRuby3-Filtercube

$Int_{donor(mClover3)}$: Intensity of mClover3 with mClover3-Filtercube

$Int_{FRET(mClover3)}$: Intensity of mClover3 with FRET-Filtercube

3.4.1.2 FRET efficiency with acceptor photobleaching

Acceptor photobleaching of cells was conducted to determine the FRET efficiency, which is calculated, based on the ratio of donor fluorescence increase following complete acceptor photo bleaching. CHO cells were transfected with both Kv4.2-mClover3 constructs and KChIP2b-mRuby3 constructs containing varying linker lengths (0, 2, 4, 7 amino acids) at a 1:5 ratio, and imaged 48 hours later. The cells were placed in an imaging solution and an initial image was taken using the mClover3/mClover3 filtercube with λ = 488 nm and the mRuby3/mRuby3 filtercube with λ = 550 nm. The cells were then subjected to photobleaching for 20 minutes using the

mRuby3/mRuby3 filter cube setting with λ = 550 nm. Following this, images were captured again using the previously described settings.
Using ImageJ (v. 1.53e), the images were subjected to analysis, and the average gray values were determined for each cell in every image, while maintaining a consistent region of interest for each cell.
As the photobleaching of mRuby3 was incomplete after 20 minutes, a partial acceptor photobleaching correction factor was calculated for each experiment.

$$Cf = 1 + \frac{Int_{acceptor}^{post}}{Int_{acceptor}^{pre}}$$

Cf : partial acceptor photo bleaching correction factor

$Int_{acceptor}^{post}$: Intensity of acceptor after acceptor bleaching

$Int_{acceptor}^{pre}$: Intensity of acceptor prior acceptor bleaching

The FRET efficiency was then calculated as followed:

$$F_{eff} = \frac{\left(Int_{donor}^{post} - Int_{donor}^{pre}\right)}{Int_{donor}^{post}} * Cf$$

F_{eff} : Fret efficiency

Int_{donor}^{pre} : Intensity of donor prior acceptor bleaching

Int_{donor}^{post} : Intensity of donor after acceptor bleaching

From there, several construct combinations were further analyzed using fluorescence lifetime imaging (FLIM).

3.4.2 Fluorescence-lifetime imaging microscopy (FLIM)

FLIM is a method that detects the decay time of fluorescence emission from fluorophores, which absorb light energy and emit it back as fluorescence with a specific lifetime. FRET can impact FLIM by modifying the fluorescence lifetime of the donor molecule. During FRET, the excited donor molecule transfers its energy to a neighboring acceptor molecule that then produces fluorescence. Consequently, the fluorescence lifetime of the donor molecule is reduced.

CHO cells were seeded out at µ-slides with 4 wells with a cell count of $1x10^4$ per well and transfected as previously described and measurements were taken 48h after transfection. Prior to imaging, the culture medium was changed to imaging solution and measurements were performed at the UKE Microscopy Imaging Facility (UMIF) using the Abeerior STED expert line microscope (in confocal mode).

Analysis of raw data were made using a script kindly provided by Antonio Virgilio Faila from the UMIF resulting in a mean fluorescence lifetime for each conducted experiment.

FRET efficiency was calculated using the following equation:

$$F_{eff} = 1 - \left(\frac{\tau_{donor,FRET}}{\tau_{donor,alone}}\right)$$

F_{eff} : FRET efficiency

$\tau_{donor,FRET}$: time constant fluorescence lifetime of mClover3 expressed as FRET pair with mRuby3

$\tau_{donor,alone}$: time constant fluorescence lifetime of mClover3 expressed alone

3.4.3 Fluorescence imaging with LSM800

Epitope-tagged proteins were transiently transfected in HEK cells and imaged 48 h after transfection. The first group of cells was incubated under standard conditions in cultivating medium, while the second group was incubated in cultivating medium containing 30 µM BAPTA-AM, a highly selective Ca^{2+} chelator capable of penetrating the cell membrane.

3.4.3.1 Nuclear and plasma membrane staining

To prepare for imaging, both the cell membrane and nucleus were stained using the *CellBrite® Steady Membrane Staining Kit 405* (Biotinum, USA) and *SYTO™ Deep Red Nucleic Acid Stain* (ThermoFischer). The staining solutions were prepared on the day of imaging, with the membrane stain and enhancer being diluted to a 1x concentration in the imaging solution as instructed by the manufacturer. The nuclear stain was added to the staining solution at a 1.5x concentration. The cultivating medium was removed, and 100 µL of staining solution was added and incubated at +37°C for 1 h. The staining solution was removed, and 200 µL of imaging solution were added to the well. For the Ca^{2+}-free group, Ca^{2+}-free imaging solution was used, and the final step involved Ca^{2+}-free imaging solution + 30 µM BAPTA-AM.

3.4.3.2 Data acquisition and image processing

The localization of epitope-tagged proteins was examined using a laser scanning microscope (*LSM800*, Zeiss, Jena) equipped with an oil-immersion 63x objective (*Plan-Apochromat 63x/1.4 Oil DIC M27*, Zeiss, Jena). The corresponding images were controlled by Zeiss Zen software (v.3.7), which was also utilized for image processing. To begin, one drop of immersion oil (*Immersol 518F*, Zeiss, Jena) was placed onto the objective, and a µ-slide was secured on the objective table. The mRuby3 channel was excited using λ = 561 nm with 4.8% laser intensity, and detection was set to 560 - 650 nm with a pinhole size of 51 µm. For mClover3, excitation was set to λ = 488 nm with 1.5% laser intensity, and detection was set to 500-570 nm with a pinhole size of 45 µm. To visualize the cell membrane stain, excitation was set to λ = 405 nm with 3.5 - 5% intensity, and detection was set from 400 - 500 nm with a pinhole size of 38 nm. Finally, nuclear staining was visualized by exciting at λ = 640 nm with 5 - 10% laser intensity, and detection was set to 640 - 700 nm with a pinhole size of 100 µm. Each channel was imaged separately.

Images were then background subtracted, which was performed using the built-in method of ZEN blue software with a rolling ball radius of 25 pixels.

4. Results

4.1 Characteristics of fluorophores and FRET efficiency

Fluorescence characteristics were determined for mRuby3 and mClover3 as well as bleedthrough values for the used filter cube setup. In addition, FRET efficiencies were analyzed and tested for different linker lengths in epitope-tagged Kv4.2 and KChIP2.

4.1.1 Photobleaching half time for mClover3 and mRuby3 expressed in CHO cells

CHO cells were transfected with either mClover3 or mRuby3 cDNA. Images were taken every 5 seconds while cells were continuously bleached at their respective wavelengths (mClover3: λ = 488 nm, mRuby3: λ = 560 nm).

For mClover3 the photostability showed a half-time $t_{1/2}$ = 96.6 ± 8.5 s (n = 13) and for mRuby3 $t_{1/2}$ = 571.3 ± 28.1 s (n = 8). Additionally, mRuby3 intensity decreased substantially in the first 5 seconds instead of a continuous single exponential decay (Figure 4.1)

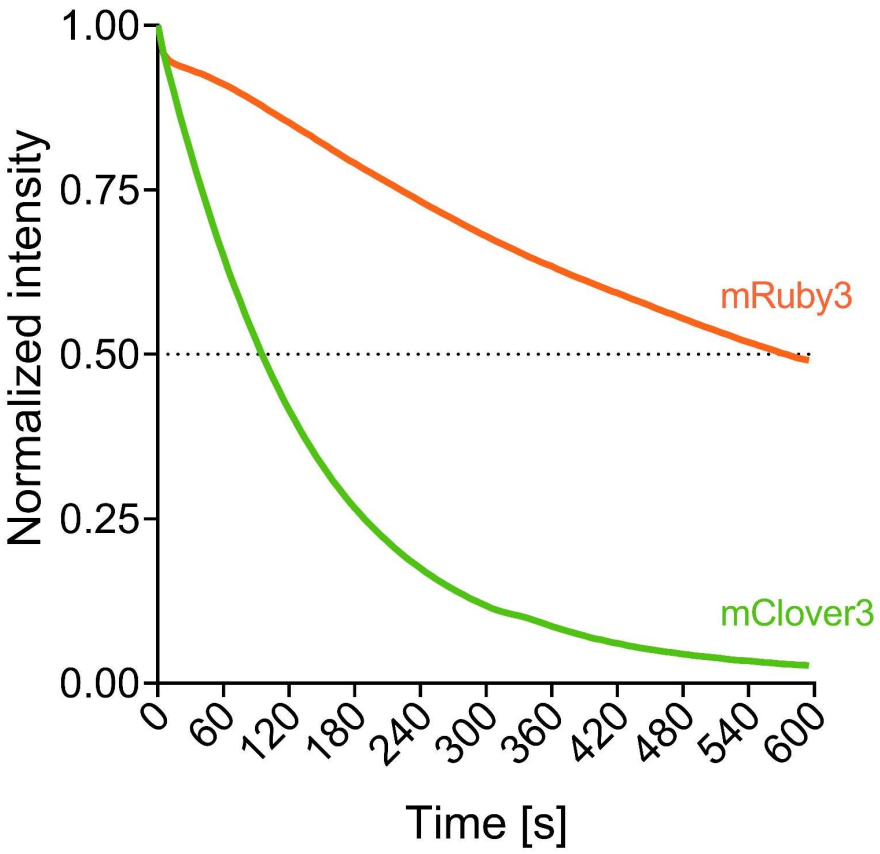

Figure 4.1: **Photostability of fluorophores mClover3 and mRuby3.**
Fluorophores mClover3 and mRuby3 expressed in CHO cells were continuously illuminated with their respective excitation wavelength and every 5 seconds a picture was taken. Background subtracted mean grey values were normalized to initial picture. Data were fitted using a single exponential decay.

4.1.2 Determination of bleedthrough values

Bleedthrough values for PolychromeV and filter cubes resulted in a = 0.125 ± 0.014 and b = 0 (n = 15) as bleedthrough from mRuby3 in the FRET filter cube as direct excitation of mRuby3. For mClover3 bleedthrough values resulted in c = 0 and d = 0.097 ± 0.015 (n = 18) as tail emission.

4.1.3 Acceptor photobleaching

Epitope-tagged Kv4.2^{C} and KChIP2^{R} with different linker lengths resulted in the following FRET efficiencies when mRuby3 was bleached:

Table 4.1: **FRET efficiency by acceptor photobleaching of Kv4.2^{C} and KChIP2^{R} in CHO cells.** All entries describe mean ± SD.

	Kv4.2^{C} **L0**	Kv4.2^{C} **L2**	Kv4.2^{C} **L4**	Kv4.2^{C} **L7**
KChIP2^{R} **L0**	5.6 ± 0.6 % (n = 3)	10.5 ± 7.6 % (n = 3)	N.A.	8.9 ± 1.7 % (n = 3)
KChIP2^{R} **L2**	9.5 ± 3.9 % (n = 3)	10.4 ± 8.8 % (n = 2)	10.0 ± 10.7 % (n = 3)	10.4 ± 2.0 % (n = 2)
KChIP2^{R} **L4**	7.8 ± 3.9 % (n = 3)	10.5 ± 2.3 % (n = 3)	10.1 ± 4.6 % (n = 3)	25.4 ± 12.8 % (n = 4)
KChIP2^{R} **L7**	4.8 ± 2.8 % (n = 3)	7.1 ± 1.7 % (n = 3)	11.4 ± 4.6 % (n = 6)	11.8 ± 7.0 % (n = 6)

For all tested constructs, FRET was observed, and it was noticed that the FRET efficiency increased with longer linker lengths. To further investigate this trend, the constructs with four and seven amino acid linker lengths were analyzed more closely using fluorescence-lifetime microscopy.

4.1.4 Fluorescence-lifetime imaging microscopy (FLIM)

Fluorescence-lifetime imaging was used as a second approach to determine FRET efficiency in epitope-tagged Kv4.2 ($Kv4.2^C$) and KChIP2 ($KChIP2^R$). Acceptor photobleaching resulted in great variance between the data. Therefore, FLIM measurements could potentially increase its accuracy.

Here, fluorescence lifetime was reduced substantially when $Kv4.2^C$ and $KChIP2^R$ were measured, reinforcing previously determined FRET efficiencies. Additionally, free cytosolic mRuby3 also significantly reduced fluorescence lifetime in $Kv4.2^C$ L4. Comparing all permutations of $Kv4.2^C$ and $KChIP2^R$ revealed no significant differences between linker lengths, but a trend is visible favoring higher linker lengths.

Table 4.2: **Fluorescence-lifetime of $Kv4.2^C$ co-expressed with wild type or epitope-tagged KChIP2 studied in CHO cells.**
The fluorescence-lifetime of mClover3 substantially decreased when co-expressed with mRuby3. Groups were analyzed using a one-way ANOVA followed by a Dunnett post hoc test. Resulting FRET efficiencies were compared using one-way ANOVA followed by a Tukey post hoc test. Asterisks show significant differences in Fluorescence lifetime compared to mClover3. # show significant differences in FRET efficiency compared to epitope-tagged $KV4.2^C$ co-expressed with wild type KChIP2 and mRuby3. All entries describe mean ± SD. Two symbols : p<0.01, three symbols : p<0.001, four symbols : p<0.0001

	mClover3	**$Kv4.2^C$ L4 + KChIP2 + mRuby3**	**$Kv4.2^C$ L4 + $KChIP2^R$ L4**	**$Kv4.2^C$ L4 + $KChIP2^R$ L7**	**$Kv4.2^C$ L7 + $KChIP2^R$ L4**	**$Kv4.2^C$ L7 + $KChIP2^R$ L7**
Fluorescence lifetime [ns]	3.43 ± 0.06	3.30 ± 0.05 **	3.09 ± 0.05 ****	3.09 ± 0.06 ****	3.06 ± 0.08 ****	2.99 ± 0.08 ****
	(n = 5)	(n = 7)	(n = 8)	(n = 8)	(n = 8)	(n = 8)
FRET efficiency		3.7 ± 2.4 %	10.0 ± 2.2 % ###	9.9 ± 2.3 % ###	10.9 ± 2.8 % ####	12.8 ± 2.7 % ####

Taken together, the mClover3 and mRuby3 fluorophores are functional and were further used to generate the epitope-tagged Kv4.2 and KChIP2 constructs. Epitope-tagged $Kv4.2^C$ and $KChIP2^R$ exhibited FRET when co-expressed together, favoring higher linker lengths. Therefore, $Kv4.2^C$ and $KChIP2^R$ with a linker length of seven amino acids were further used. Next, the functionality of $Kv4.2^C$ and $KChIP2^R$ constructs was tested.

4.2 Electrophysiological characteristics of epitope-tagged Kv4.2 (Kv4.2^{C}) and KChIP2 (KChIP2^{R}) constructs

Peak amplitude and macroscopic inactivation kinetics

The injection of Kv4.2 cRNA into *Xenopus* oocytes resulted in the expression of functional channels, as evidenced by the appearance of a typical A-type current with a peak current amplitude of 4.86 ± 1.04 µA (n = 8) in response to a depolarizing step from -100 mV to +40 mV (Figure 4.2). Inactivation kinetics were analyzed by using a double exponential fitting procedure, which showed a fast inactivation constant Tau1 of 22.8 ± 1.6 ms and a slow inactivation component Tau2 of 328 ± 22 ms. Kv4.2^{C} expressed in *Xenopus* oocytes showed similar characteristics with a peak current amplitude of 4.97 ± 1.37 µA (n = 7), a fast inactivation component Tau1 of 23.5 ± 2.6 ms and a slow inactivation component Tau2 of 336 ± 23 ms (Figure 4.3).

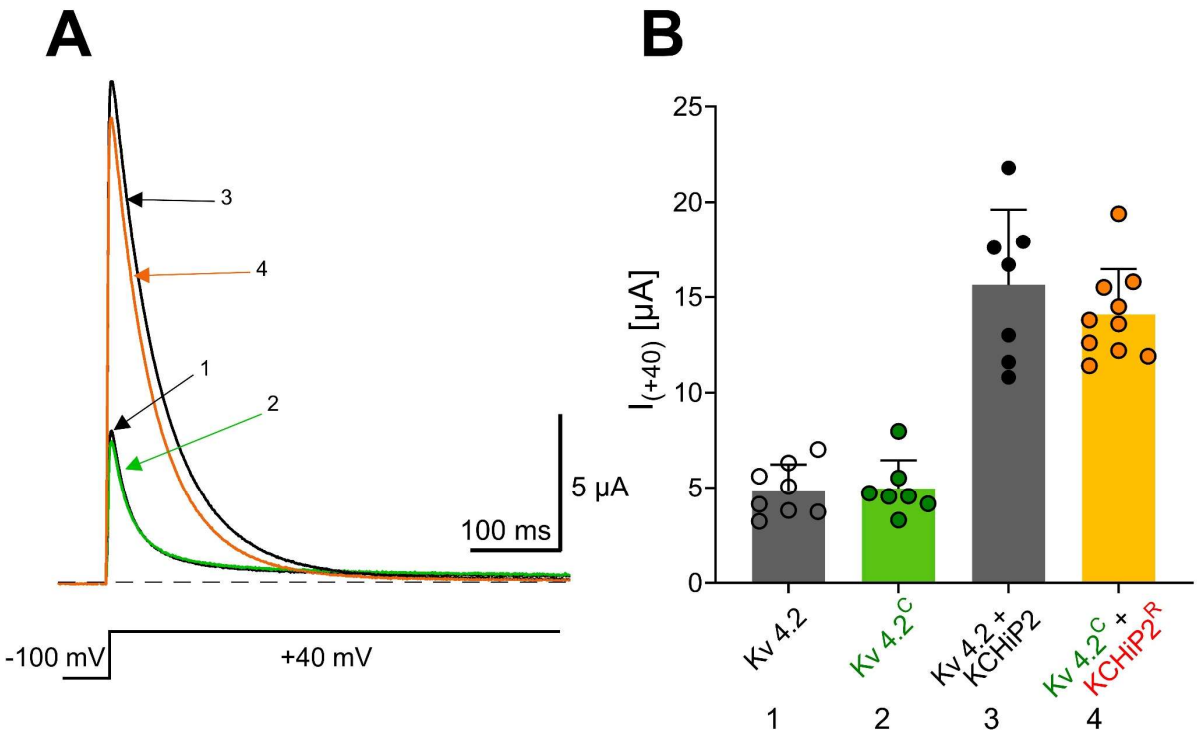

Figure 4.2: **Functional expression of wild type and epitope-tagged Kv4.2 and Kv4.2/KChIP2 channel complexes studied in *Xenopus* oocytes.**
1: Kv4.2 alone (white circles), **2**: Kv4.2-mClover3 (Kv4.2^{C}) alone (green circles), **3**: Kv4.2 co-expressed with KChIP2 (black circles), **4**: Kv4.2^{C} co-expressed with KChIP2-mRuby3 (KChIP2^{R}) (orange circles). (**A**) Macroscopic current recorded by two-electrode voltage clamp. (**B**) Peak current amplitudes of wild type and epitope-tagged Kv4.2 or Kv4.2/KChIP2 channel complexes. Bars show mean ± SD.

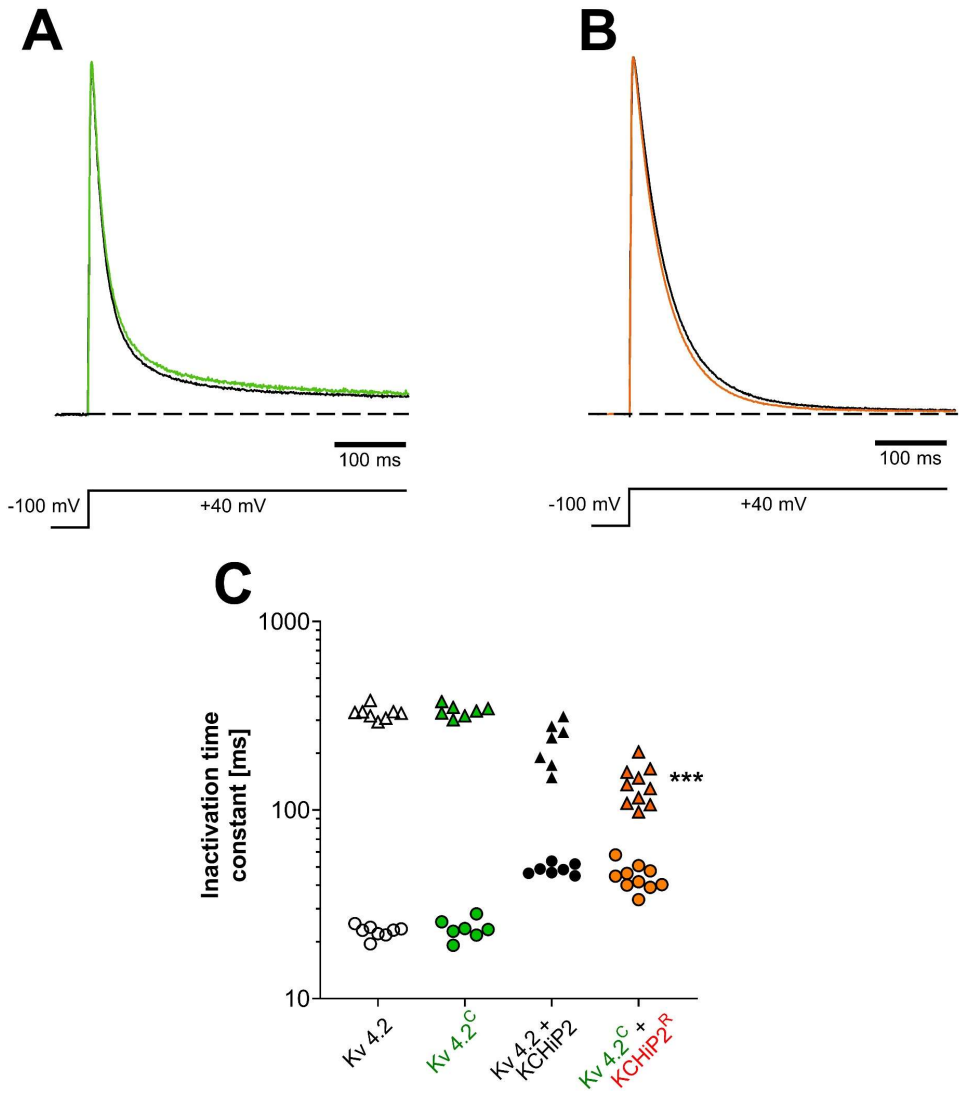

Figure 4.3: **Effect of epitope-tagging on the macroscopic inactivation kinetics on Kv4.2 and Kv4.2/KChIP2 channel complexes studied in *Xenopus* oocytes.**
Currents were measured by applying voltage steps from -100 mV to +40 mV under two-electrode voltage clamp showing normalized A-type current produced by (**A**) Kv4.2 (black trace, white symbols), $Kv4.2^{C}$ (green trace & symbols) and (**B**) Kv4.2/KChIP2 (black trace & symbols) and $Kv4.2^{C}$/$KChIP2^{R}$ (orange trace & symbols) channel complexes (**B**). (**C**) Inactivation time constants were obtained by using a double exponential fitting procedure, which resulted in a fast inactivation time constant Tau1 (**Circles**) and slow inactivation time constant Tau2 (**Triangles**).
Epitope-tagged constructs were compared with the wild type using an unpaired Students t-test. *** $p<0.001$.

Co-expression of Kv4.2 with KChIP2 showed a significant increase in peak current amplitude to 15.63 ± 3.68 µA (n = 7, $p<0.0001$) (Figure 4.2). In addition, Tau1 was significantly higher with 48.6 ± 2.9 ms ($p<0.0001$), while Tau2 was lower with 230 ± 56 ms ($p < 0.01$). $Kv4.2^{C}$ co-expressed with $KChIP2^{R}$ resulted in a similar peak current amplitude of 14.07 ± 2.27 µA with Tau1 of 44.1 ± 6.5 ms, but significantly lower Tau2 of 137 ± 31 ms (n = 10, $p<0.001$) compared to wild type Kv4.2/KChIP2 channel complexes (Figure 4.3).

Recovery from inactivation

Recovery kinetics were obtained by applying a double pulse protocol from -100 mV to +40 mV with varying time intervals between depolarizing pulses. When Kv4.2 was expressed alone, the time constant of recovery from inactivation showed a Tau_{Rec} of 122 ± 18 ms, while Kv4.2^{C} showed a slightly lower Tau_{Rec} of 113 ± 15 ms (n.s.). Co-expression with KChIP2 showed a significant decrease in Tau_{Rec} for both wild type (19.1 ± 2.4 ms, $p<0.0001$) and epitope-tagged channel complexes (17.6 ± 2.3 ms, $p<0.0001$, n = 6), with no significant differences observed between the wild type and tagged constructs (Figure 4.4).

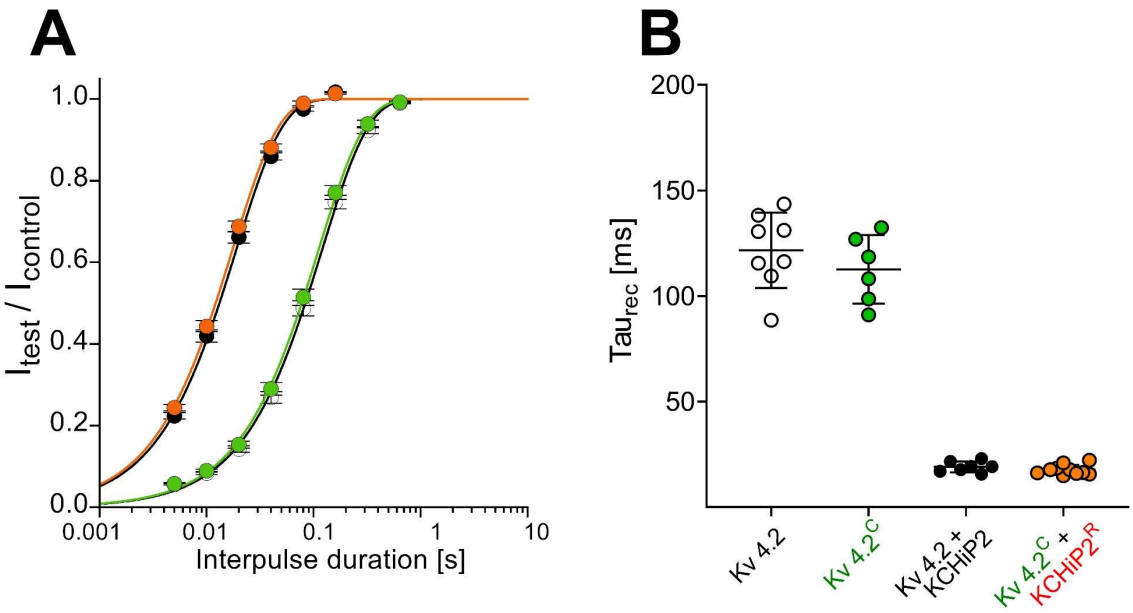

Figure 4.4: **Effect of epitope-tagging on the recovery kinetics on Kv4.2 and Kv4.2/KChIP2 channel complexes studied in *Xenopus* oocytes.**
(**A**) Recovery kinetics of Kv4.2 (black trace, white symbols), Kv4.2^{C} (green trace & symbols), Kv4.2/KChIP2 (black trace & symbols) and Kv4.2^{C}/KChIP2^{R} (orange trace & symbols) channel complexes. (**B**) Recovery kinetics were analyzed using a single exponential fit resulting in a recovery time constant Tau_{Rec}. Tau_{Rec} values of wild type and epitope-tagged constructs were compared using an unpaired Students t-test.

Voltage dependence of steady-state inactivation

In terms of the voltage dependence of steady-state inactivation, Kv4.2 alone exhibited a half-maximal inactivation ($V_{1/2\ inact}$) at -68.4 ± 0.9 mV, with a slope factor k_{inact} of 6.3 ± 0.8 mV. The addition of the C-terminal mClover3 tag to Kv4.2 significantly showed a shift in the half maximal inactivation to a more positive potential with a $V_{1/2\ inact}$ of -66.3 ± 0.9 mV ($p<0.05$) and a slope factor k of 6.6 ± 0.6 mV. Co-expression of Kv4.2 with KChIP2 showed a positive shift of $V_{1/2\ inact}$ to 54.7 ± 2.0 mV ($p<0.0001$) and a reduced slope factor k_{inact} of 4.8 ± 0.7 mV ($p<0.001$). Kv4.2^{C} co-expressed with KChIP2^{R} showed a similar positive shift of $V_{1/2\ inact}$ to -55.4 ± 1.6 mV, but with a significantly lower slope factor k_{inact} of 4.1 ± 0.5 mV ($p<0.05$) when compared to the wild type counterpart (Figure 4.5).

Concluding so far, epitope-tagging of Kv4.2 and KChIP2 do not seem to greatly influence the Kv4.2/KChIP2 channel complex and its biophysical properties.

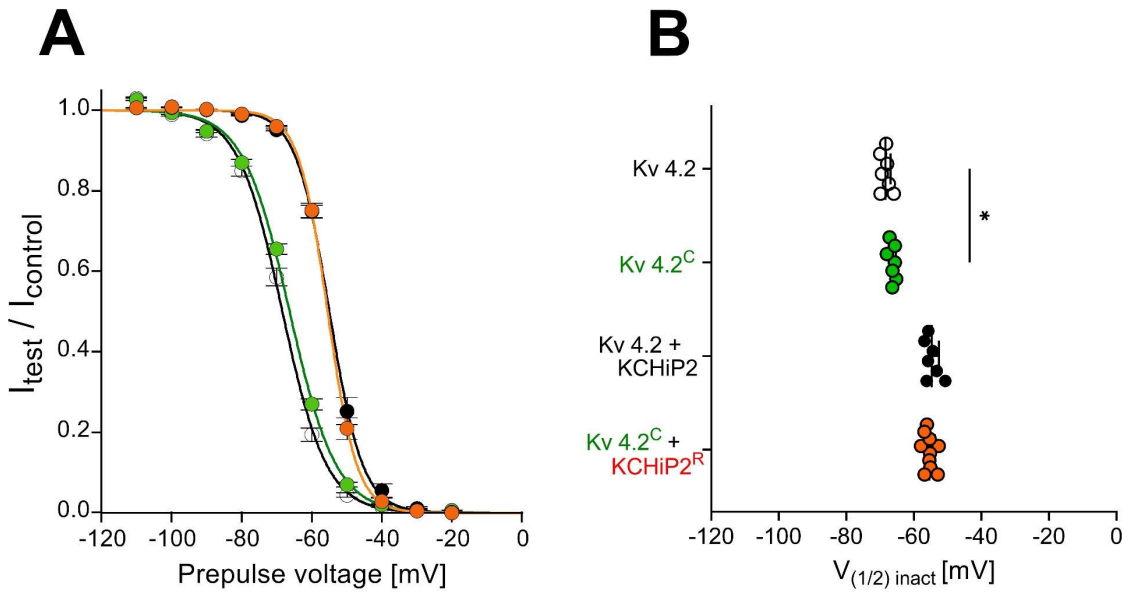

Figure 4.5: **Effect of epitope-tagging on the voltage dependence of steady-state inactivation on Kv4.2 and Kv4.2/KChIP2 channel complexes studied in *Xenopus* oocytes.**
(**A**) Voltage dependence of steady-state inactivation of Kv4.2 (black trace, white symbols), Kv4.2^{C} (green trace & symbols), Kv4.2/KChIP2 (black trace & symbols) and Kv4.2^{C}/KChIP2^{R} (orange trace & symbols) channel complexes. (**B**) Steady-state inactivation were analyzed using a single Boltzmann function resulting in $V_{1/2\ inact}$ values. Wild type and epitope-tagged constructs were compared using an unpaired Students t-test. *$p<0.05$.

Table 4.3: **Electrophysiological properties of wild type and epitope-tagged Kv4.2 and Kv4.2/KChIP2 channel complexes studied in *Xenopus* oocytes.** Wild type and epitope-tagged constructs were compared using an unpaired Students t-test. All entries describe mean ± SD. *p<0.05, ***p<0.001

	$I_{(+40)}$ [µA]	Tau1 [ms]	%Tau1	Tau2 [ms]	%Tau2	Tau_{Rec} [ms]	$V_{1/2\ inact}$ [mV]	k_{inact} [mV]
Kv4.2	4.86 ± 1.04 (n = 8)	22.8 ± 1.6	92 ± 1	328 ± 22	8 ± 1	122 ± 18 (n = 8)	-68.4 ± 1.32 (n = 7)	6.3 ± 0.8
$Kv4.2^{C}$	4.97 ± 1.37 (n = 7)	23.5 ± 2.6	92 ± 1	336 ± 23	8 ± 1	113 ± 15 (n = 6)	-66.3 ± 0.9 * (n = 6)	6.6 ± 0.6
Kv4.2 + KChIP2	15.63 ± 3.68 (n = 7)	48.6 ± 2.9	96 ± 2	230 ± 56	4 ± 2	19.1 ± 2.4 (n = 7)	-54.7 ± 2.0 (n = 7)	4.8 ± 0.7
$Kv4.2^{C}$ + $KChIP2^{R}$	14.07 ± 2.27 (n = 10)	44.2 ± 6.5	94 ± 2	137 ± 31 ***	6 ± 2	17.6 ± 2.3 (n = 10)	-55.4 ± 1.6 (n = 10)	4.1 ± 0.5 *

4.3 Ca^{2+}-related effects in *Xenopus* oocyte inside-out macro patches

In order to investigate the influence of Ca^{2+} on Kv4.2/KChIP channel complexes, we utilized macro patches from *Xenopus* oocytes. Following cRNA injection, oocytes were incubated for at least two days, after which the vitelline layer was removed and glass electrodes were used to excise patches. First, control experiments were conducted with uninjected oocytes. The subsequent analysis focused on Ca^{2+}-related effects on Kv4.2 channels co-expressed with DPP6 and KChIP. The co-expression of DPP6 was deemed necessary due to its significant trafficking effect, allowing for recordings with a high signal-to-noise ratio and a more physiologically relevant approach.

4.3.1 Effect of internal application of Ca^{2+} on control *Xenopus* oocyte macro patches

Before investigating Kv4.2 channel complexes in *Xenopus* macro patches, Ca^{2+} buffered solutions were applied to uninjected *Xenopus* oocyte macro patches. These oocytes naturally express Ca^{2+}-activated chloride channels that are asymmetrically distributed in the oocyte plasma membrane, with the highest density in the animal pole[50]. Therefore, macro patches were exclusively recorded from patches in the vegetative pole. When a high chloride solution with 10 µM Ca^{2+} was applied to patches from the vegetative pole, a stable bidirectional current was induced in macro patches up to several 100 pA (Figure 4.6A). To minimize chloride conductance, a minimal chloride solution base was used where most chloride was substituted with methylsulfonate. The application of low chloride solution with 10 µM Ca^{2+} showed minimal conductance of less than 50 pA in recorded patches, which was reversible when switched back into a Ca^{2+}-free solution (Figure 4.6B).

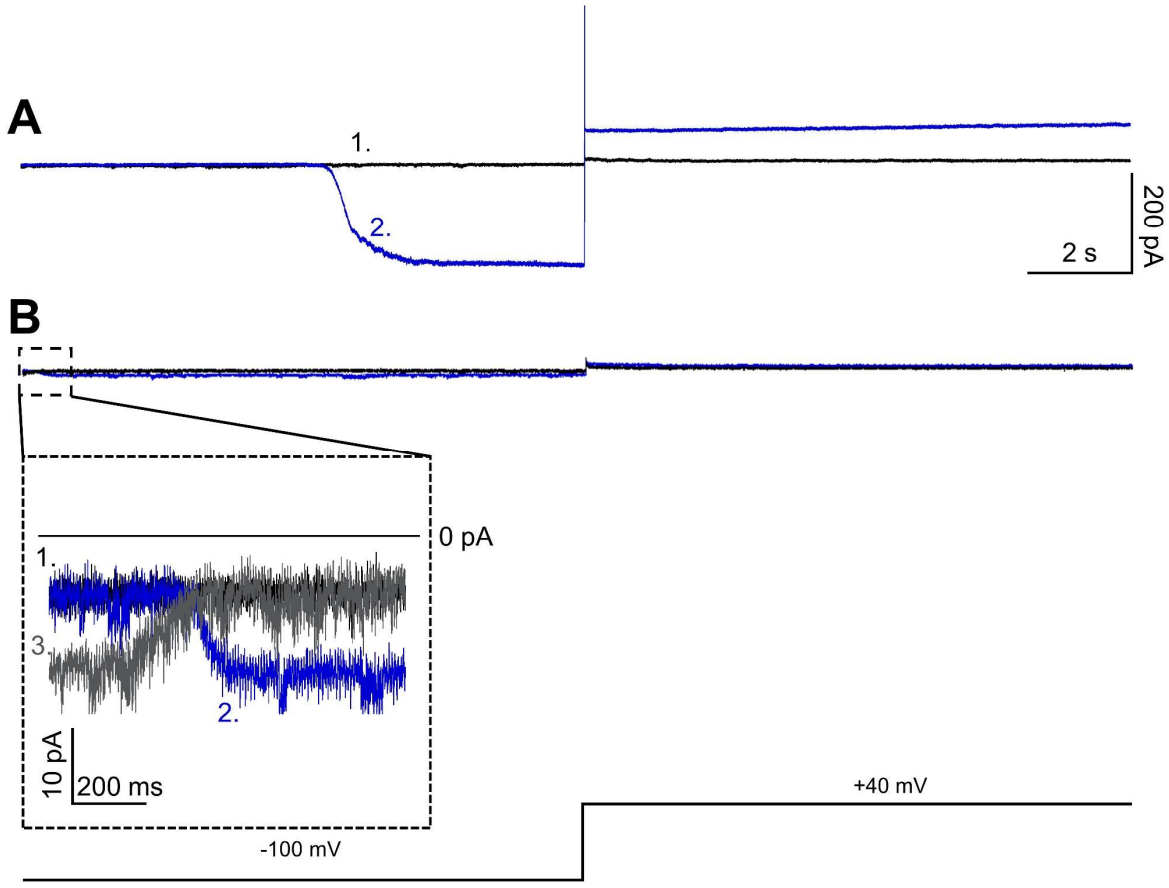

Figure 4.6: **Endogenous Ca^{2+}-induced currents in *Xenopus* oocytes control inside-out macro patches.**
(**A**) Representative current recording in a high chloride solution. Currents were recorded by applying voltage steps from -100 mV to +40 mV under Ca^{2+}-free condition (black & grey) and in 10 µM Ca^{2+} (blue). (**B**) Current recording in low chloride solution.

4.3.2 Ca^{2+}-related effects on Kv4.2 co-expressed with KChIP3

Macroscopic inactivation kinetics

Next, cytosolic Ca^{2+}-related effects in Kv4.2 were investigated by co-expressing Kv4.2, DPP6 and KChIP3 in macro patches and the influence of epitope-tagging was studied. Currents were measured and protocols were applied prior to switching to a 10 µM Ca^{2+} solution. The wild type binary complex Kv4.2/DPP6 showed a Tau1 of 14.6 ± 1.2 ms and Tau2 of 241 ± 36 ms (n = 10). The epitope-tagged Kv4.2^{C}/DPP6 channel complex showed similar macroscopic inactivation kinetics (n = 12, n.s.) (Figure 4.7A). Application of 10 µM Ca^{2+} showed no significant change in inactivation kinetics in both groups, and comparing Ca^{2+}-related effects between wild type and epitope-tagged binary complexes showed no significant differences between them (Figure 4.7B).

Co-expression with KChIP3, resulting in a ternary complex Kv4.2/DPP6/KChIP3, showed a Tau1 of 32.3 ± 9.7 ms and Tau2 of 105 ± 22 ms (n = 11) for wild type constructs. Epitope-tagged Kv4.2^{C}/DPP6/KChIP3 channel complexes, also showed similar macroscopic inactivation kinetics (n = 11, n.s.). The co-expression of KChIP2 as well as KChIP3 slowed macroscopic inactivation in the absence and presence of DPP6. Notably, application of 10 µM Ca^{2+} resulted in faster inactivation reflected by a significant decrease in Tau1. This effect was observed in both wild type and Kv4.2^{C} ternary complexes. Comparing Ca^{2+}-related effects between wild type and epitope-tagged constructs showed no significant differences. Therefore, it was concluded that C-terminal tagging of Kv4.2 has no significant effect on macroscopic inactivation kinetics or Ca^{2+}-related effects in macroscopic inactivation.

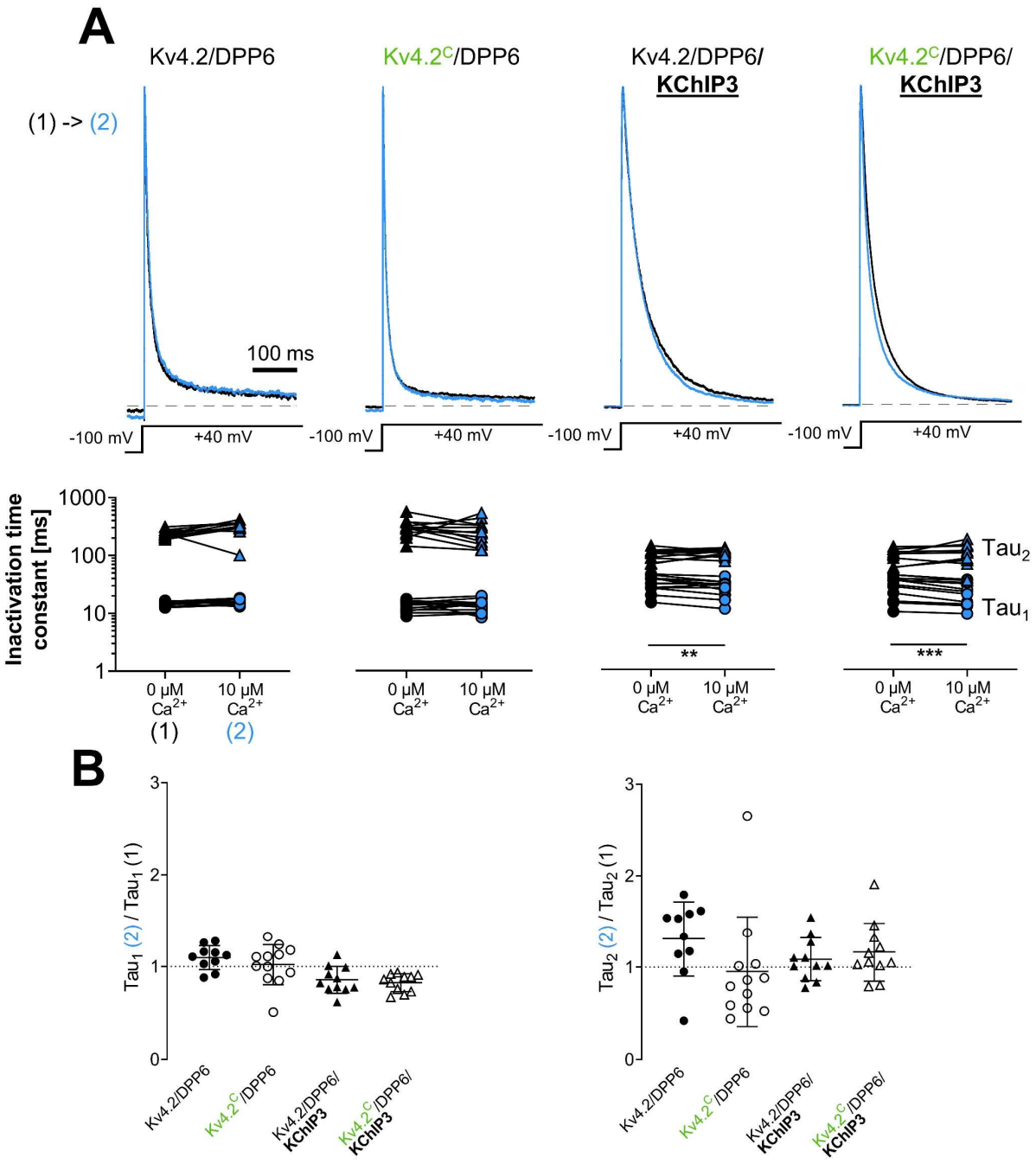

Figure 4.7: **Macroscopic inactivation kinetics of wild type and epitope-tagged Kv4.2 channel complexes studied in inside-out macro patches from *Xenopus* oocyte membranes.**
(**A**) Normalized currents in Ca^{2+}-free solution (black) and 10 µM Ca^{2+} (blue) and inactivation kinetics of macroscopic current analyzed using a double exponential fitting procedure. Fast inactivation component Tau1 is shown as circles, and slow inactivation component Tau2 is shown as triangles.
(**B**) Ratio of paired Tau1 and Tau2 values from Ca^{2+}-free solution and 10 µM Ca^{2+}. Ca^{2+} application were tested for significance via a ratio paired Students t-test. Epitope-tagged constructs were compared to their wild type counterpart by unpaired Students t-test. **p<0.01, ***p<0.001

Recovery from inactivation

Concerning the recovery from inactivation, wild type binary complexes Kv4.2/DPP6 exhibited a Tau_{Rec} of 87.9 ± 21.1 ms (n = 10). The application of 10 µM Ca^{2+} led to an increase in Tau_{Rec} to 96.6 ± 23.7 ms, although this was not statistically significant (p= 0.0875). Kv4.2^{C}/DPP6 showed a Tau_{Rec} of 104 ± 18 ms. Application of 10 µM Ca^{2+} significantly increased Tau_{Rec} to 122 ± 27 ms ($p<0.01$, n = 11).

Co-expression with KChIP3 accelerated the recovery from inactivation. Kv4.2/DPP6/KChIP3 showed a Tau_{Rec} of 54.8 ± 10.4 ms. Application of 10 µM Ca^{2+} showed a significant increase of Tau_{Rec} to 64.5 ± 10.7 ms ($p<0.01$, n = 9). Epitope-tagged Kv4.2^{C}/DPP6/KChIP3 showed a Tau_{Rec} of 46.1 ms ± 10.5 and application of 10 µM Ca^{2+} also increased Tau_{Rec} significantly to 59.5 ± 13.1 ms ($p<0.0001$, n = 10). Comparing the relative changes in Tau_{Rec} when Ca^{2+} is applied revealed no significant differences between wild type and epitope-tagged channel constructs (Figure 4.8).

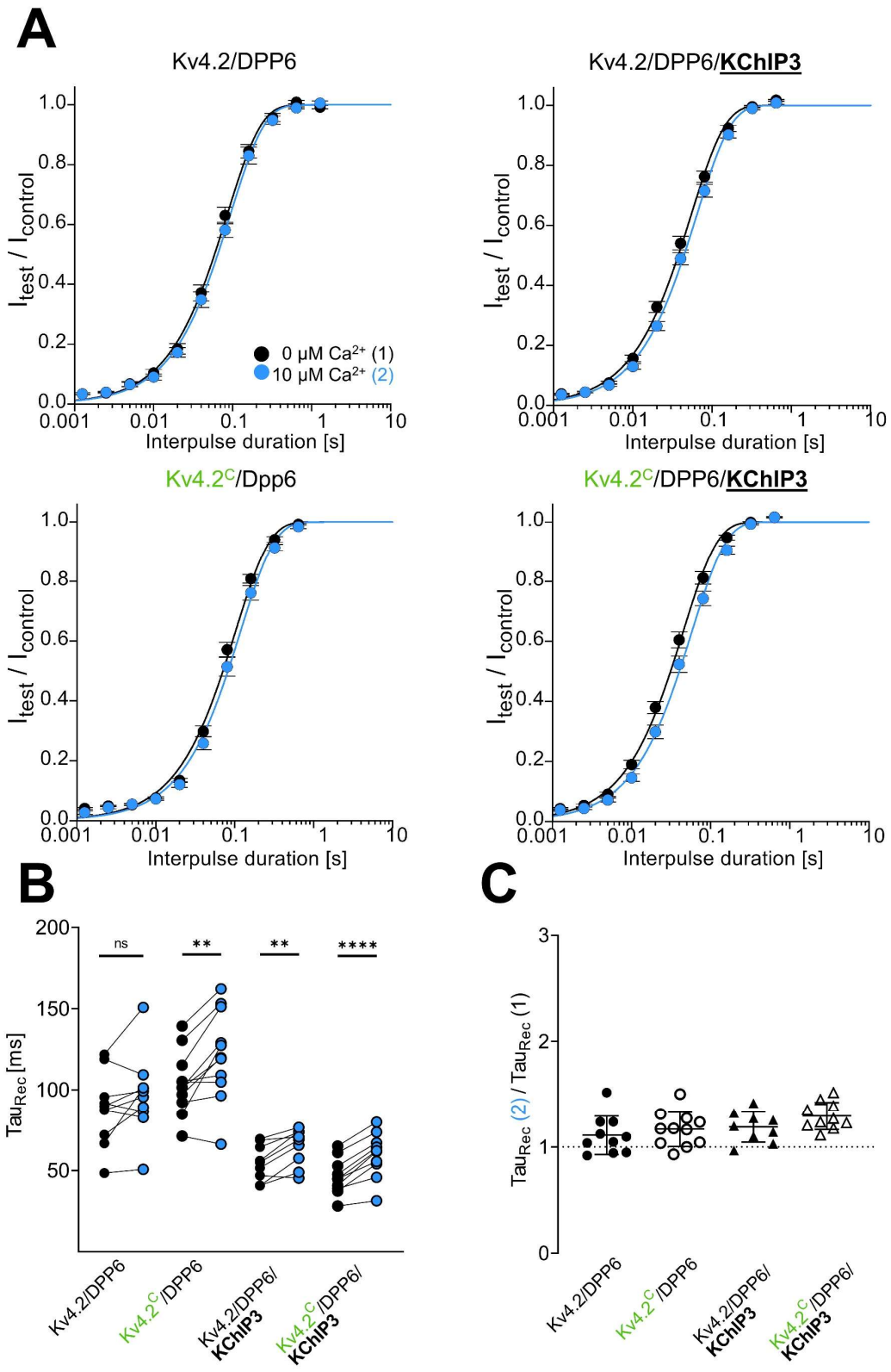

Figure 4.8: **Recovery from inactivation of wild type and epitope-tagged Kv4.2 channel complexes studied in inside-out macro patches from *Xenopus* oocyte membranes.**
(**A**) Recovery kinetics of wild type and epitope-tagged Kv4.2 co-expressed with DPP6 and KChIP3 in Ca^{2+}-free solution (black) and 10 µM Ca^{2+} (blue). (**B**) Recovery kinetics were analyzed using a single exponential fit and individual pairs are shown. Pairs were compared using a paired ratio Students t-test. (**C**) Relative changes of Tau_{Rec}. Epitope-tagged constructs were compared to their wild type counterpart by unpaired Students t-test. **p<0.01, ****p<0.0001

Voltage dependence of steady-state inactivation

The investigation of the voltage dependence of steady-state inactivation revealed a consistent negative shift in $V_{1/2\ inact}$ across all cases when 10 µM Ca^{2+} were applied to the internal side of inside-out patches. Kv4.2/DPP6 exhibited a Ca^{2+}-induced shift in $V_{1/2\ inact}$ of -3.7 ± 2.1 mV, from -95.2 ± 3.4 mV to -98.9 ± 3.5 mV ($p<0.01$, $n = 9$). Kv4.2^{C}/DPP6 showed a smaller shift in $V_{1/2\ inact}$ of -2.1 ± 1.8 mV, from -95.7 ± 3.6 mV to -97.8 ± 3.5 mV ($p<0.01$, $n = 10$).

Kv4.2/DPP6/KChIP3 showed a shift in voltage dependence of steady-state inactivation of -2.8 ± 1.1 mV, from -95.6 ± 3.5 mV to -98.4 ± 3.3 mV ($p<0.001$, $n = 7$). For Kv4.2^{C}/DPP6/KChIP3, the Ca^{2+}-induced shift in $V_{1/2\ inact}$ was -3.8 ± 2.1 mV, from -93.1 ± 2.5 mV to -96.9 ± 2.9 mV ($p<0.01$, $n = 7$). Comparison of the shifts in $V_{1/2\ inact}$ between wild type and epitope-tagged channel complexes did not show any significant differences (Figure 4.9).

In conclusion, epitope-tagging of Kv4.2/DPP6 and Kv4.2/DPP6/KChIP3 channel complexes did not significantly alter Ca^{2+}-related effects in either macroscopic inactivation kinetics or voltage dependence of steady-state inactivation. Kv4.2^{C}/DPP6 channel complexes showed a significant Ca^{2+}-induced effect in the recovery from inactivation. Comparing their relative effects to the wild type channel complexes showed no significant difference, concluding that epitope-tagging did not influence channel functionality and can be further utilized in future studies.

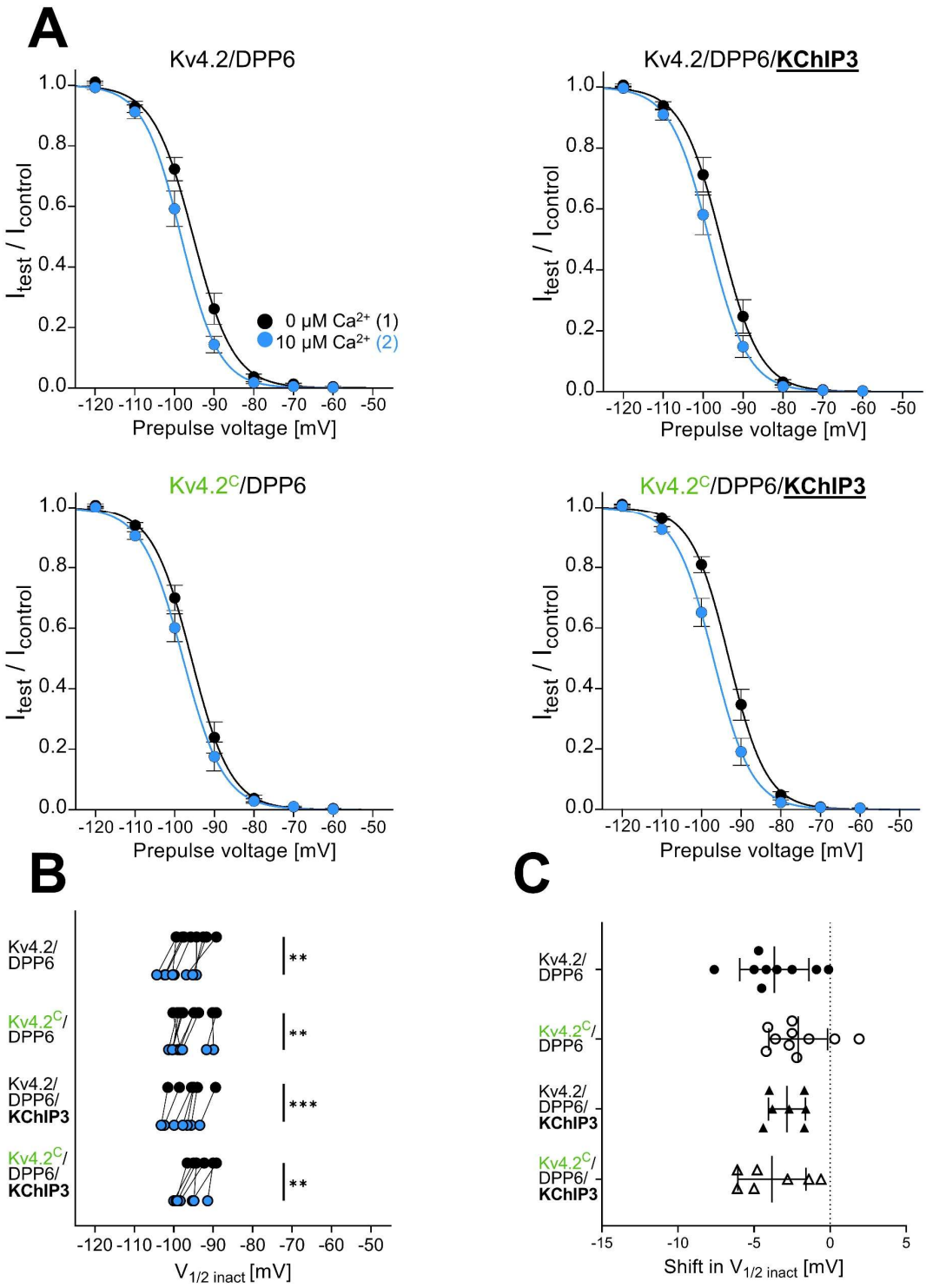

Figure 4.9: **Voltage dependence of steady-state inactivation of wild type and epitope-tagged Kv4.2 channel complexes studied in inside-out macro patches from *Xenopus* oocyte membranes.**
(**A**) Voltage dependence of steady-state inactivation in wild type and epitope-tagged Kv4.2 co-expressed with DPP6 and KChIP3 in Ca^{2+}-free solution (black) and 10 µM Ca^{2+} (blue). (**B**) Voltage dependence of steady-state inactivation was analyzed using a single Boltzmann fit and individual pairs are shown. Pairs were compared using a paired Students t-test. (**C**) Shift in $V_{1/2\ inact}$. Epitope-tagged constructs were compared to their wild type counterpart by unpaired Students t-test. **p<0.01, ***p<0.001

Table 4.4: **Electrophysiological properties of wild type and epitope-tagged Kv4.2/DPP6 and Kv4.2/DPP6/KChIP3 channel complexes studied in *Xenopus* oocytes inside-out macro patches.**
Wild type and epitope-tagged constructs were compared using an unpaired Students t-test. All entries describe mean ± SD.

	Tau1 [ms]	Rel. change Tau1	Tau2 [ms]	Rel. change Tau2	Tau_{Rec} [ms]	Rel. change Tau_{Rec}	$V_{1/2\ inact}$ [mV]	Shift in $V_{1/2\ inact}$ [mV]
Kv4.2/DPP6	(n = 10)				(n = 10)		(n = 9)	
(1) 0 µM Ca^{2+}	14.6 ± 1.2		241 ± 36		87.9 ± 21.1		-95.2 ± 3.4	
(2) 10 µM Ca^{2+}	15.9 ± 1.7	1.10 ± 0.13	309 ± 82	1.31 ± 0.40	96. 6 ± 23.7	1.11 ± 0.17	-98.9 ± 3.5	3.7 ± 2.1
Kv4.2^{C}/DPP6	(n = 12)				(n = 11)		(n = 9)	
(1) 0 µM Ca^{2+}	13.2 ± 2.6		289 ± 96		104 ± 18		-95.7 ± 3.6	
(2) 10 µM Ca^{2+}	13.3 ± 3.1	1.02 ± 0.22	254 ± 115	0.95 ± 0.60	122 ± 27	1.17 ± 0.16	-97.8 ± 3.7	2.1 ± 1.8
Kv4.2/DPP6/ KChIP3	(n = 11)				(n = 9)		(n = 7)	
(1) 0 µM Ca^{2+}	32.3 ± 9.7		105 ± 22		54.8 ± 10.4		-95.6 ± 3.5	
(2) 10 µM Ca^{2+}	27.4 ± 8.4	0.86 ± 0.14	110 ± 16	1.08 ± 0.23	64.5 ± 10.7	1.19 ± 0.14	-98.4 ± 3.3	2.8 ± 1.1
Kv4.2^{C}/DPP6/ KChIP3	(n = 11)				(n = 10)		(n = 7)	
(1) 0 µM Ca^{2+}	28.6 ± 11.0		98 ± 29		46.1 ± 10.5		-93.1 ± 2.5	
(2) 10 µM Ca^{2+}	23.5 ± 9.5	0.83 ± 0.10	113 ± 42	1.17 ± 0.32	59.5 ± 13.1	1.29 ± 0.12	-96.9 ± 2.9	3.8 ± 2.1

4.3.3 Ca^{2+}-related effects on Kv4.2 co-expressed with DPP6 and different KChIP subtypes in *Xenopus* oocyte inside-out macro patches

The objective of this investigation was to analyze the effects on Ca^{2+} of Kv4.2/DPP6 channel complexes co-expressed with either KChIP2 or KChIP3 and compare the two KChIP subtypes. Kv4.2/DPP6 served as control. Excised patches were perfused with Ca^{2+}-free internal solution until stable currents have formed as starting condition. Stimulation protocols were applied as the primary control. Then the perfusion solution was switched to a 10 µM Ca^{2+} internal solution, and the same stimulation protocols were reapplied. Finally, the patches were perfused again with a Ca^{2+}-free internal solution and stimulation protocols were again applied as a secondary control.

Macroscopic inactivation kinetics

In the absence of Ca^{2+}, the binary complex Kv4.2/DPP6 exhibited macroscopic inactivation kinetics with a time constant Tau1 of 14.6 ± 1.3 ms and Tau2 of 241 ± 38 ms (n = 12). The ternary complex Kv4.2/DPP6/KChIP2 showed a fast inactivation time constant Tau1 of 21.6 ± 4.8 ms and a slow inactivation time constant Tau2 of 93 ± 32 ms (n = 8) and Kv4.2/DPP6/KChIP3 channel complexes in Tau1 of 32.0 ± 9.8 ms and Tau2 of 103 ± 23 ms (n = 12).

With internal application of 10 µM Ca^{2+} no significant effects were observed on the inactivation time constants Tau1 and Tau2, neither in the binary complexes nor in the ternary complexes with KChIP2 or KChIP3. However, removal of Ca^{2+} caused a significant reduction in the fast inactivation time constant Tau1 for Kv4.2/DPP6/KChIP2 and Kv4.2/DPP6/KChIP3. For Kv4.2/DPP6/KChIP2 ternary complexes, Tau1 is reduced from 20.6 ± 5.8 ms to 15.7 ± 3.7 ms ($p<0.01$) and for Kv4.2/DPP6/KChIP3 ternary complexes from 28.4 ± 9.0 ms to 22.7 ± 7.2 ms ($p<0.01$). In both cases, the reductions in Tau1 were significant compared to the control value under condition (1) (Figure 4.10).

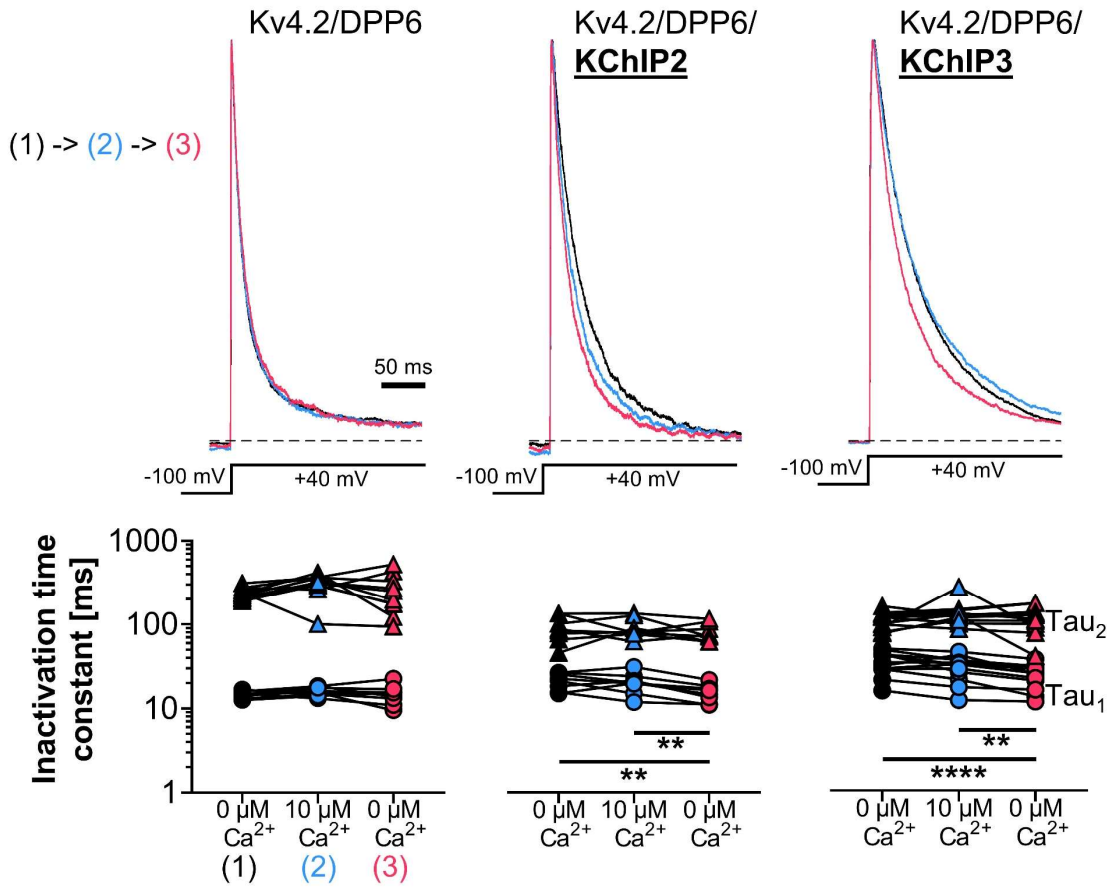

Figure 4.10: **Effect of internal Ca^{2+} on the macroscopic current inactivation on Kv4.2/DPP6 channel complexes co-expressed with KChIP studied in *Xenopus* oocyte inside-out macro patches.**
Normalized currents in Ca^{2+}-free solution (black and red trace) and 10 µM Ca^{2+} solution (blue trace). Inactivation kinetics were analyzed using a double exponential fitting procedure. Individual values are shown in triplets from 0 µM Ca^{2+} (1) to 10 µM Ca^{2+} (2) to 0 µM Ca^{2+} (3). Triplets were analyzed using repeated measures ANOVA with a Tukey post hoc test. **p<0.01, ****p<0.0001.

Although there was apparently no direct Ca^{2+}-induced effect during the initial application, significant differences appeared in the comparison of the relative changes in Tau1 between the studied groups. The relative changes in Tau1 and Tau2 between each condition were calculated and compared to each other. The relative change in Tau1 for Kv4.2/DPP6 channel complexes from Ca^{2+}-free solution (1) to 10 µM Ca^{2+} (2) is 1.100 ± 0.130 and significantly differs from KV4.2/DPP6/KChIP3 which showed a relative change in Tau1 of 0.897 ± 0.196 ($p<0.05$) (Figure 4.11).

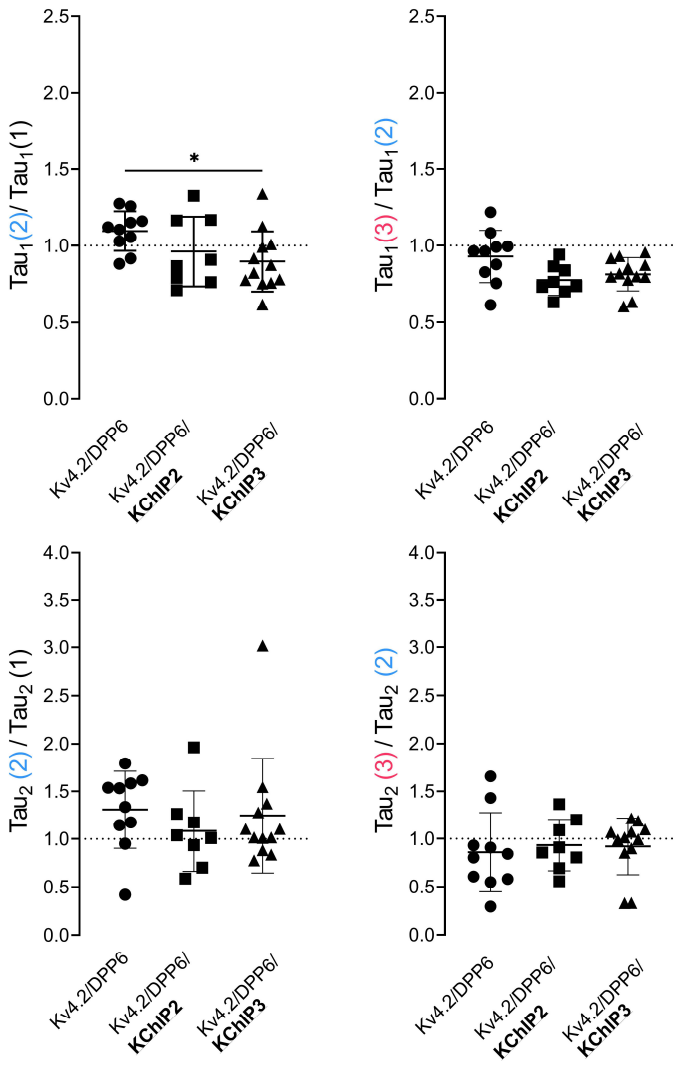

Figure 4.11: **Relative changes in macroscopic inactivation kinetics of Kv4.2 channel complexes studied in *Xenopus* oocyte inside-out macro patches.**
Inactivation time constant pairs were put in relation to the application or withdrawal of 10 µM Ca^{2+}. The resulting relative changes in inactivation kinetics were analyzed using one-way ANOVA with a Tukey post hoc test. *p<0.05.

Recovery from inactivation

Next, Ca^{2+}-induced effects on the recovery from inactivation were investigated. Kv4.2/DPP showed, in the absence of Ca^{2+}, a Tau_{Rec} of 87.9 ± 22.2 ms (n = 10). The fastest recovery from inactivation with a Tau_{Rec} of 25.5 ± 7.4 ms (n = 8) was obtained for the ternary complexes Kv4.2/DPP6/KChIP. For Kv4.2/DPP6/KChIP3 channel complexes, a Tau_{Rec} of 54.8 ± 11.0 ms (n = 9) was obtained. The internal application of Ca^{2+} showed a significant increase in Tau_{Rec} for both ternary complexes. (Figure 4.12A)

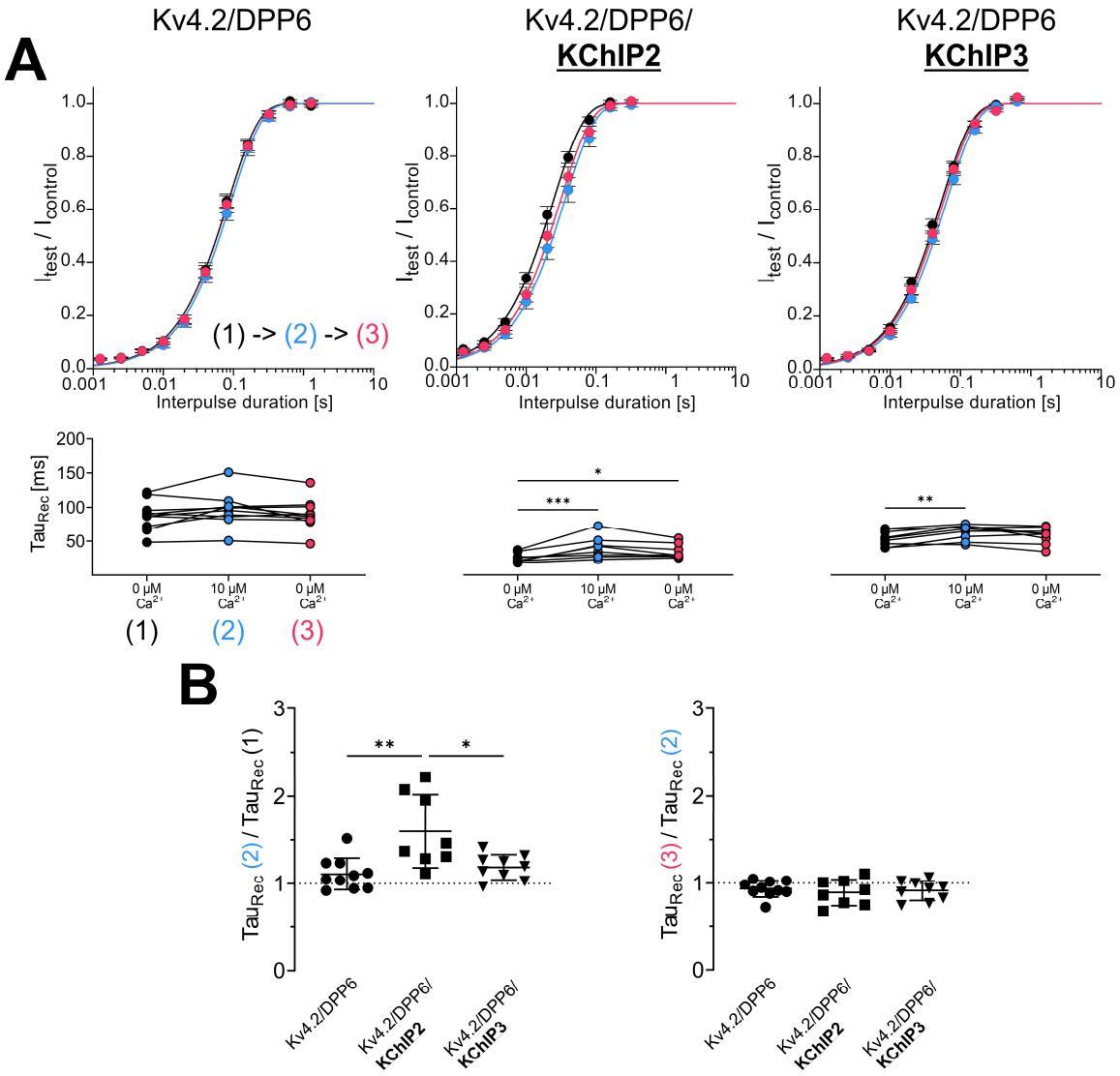

Figure 4.12: **Effects of internal Ca^{2+} on the recovery from inactivation on Kv4.2/DPP6 co-expressed with KChIP studied in *Xenopus* oocyte inside-out macro patches.**
(**A**) Recovery from inactivation in Ca^{2+}-free solution (black, red) and 10 µM Ca^{2+} (blue). Recovery from inactivation was analyzed using single exponential fit and individual values are shown in triplets. Triplets were analyzed using repeated measures ANOVA with a Tukey post hoc test.
(**B**) Relative change in Tau_{Rec} values when 10 µM Ca^{2+} was applied or withdrawn. Groups were analyzed using one-way ANOVA followed by Tukey post hock test. *p<0.05, **p<0.01, ***p<0.001

For Kv4.2/DPP6/KChIP2 channel complexes, Tau_{Rec} increased by a factor of approximately 1.60 from 25.5 ± 7.4 ms to 40.8 ± 16.4 ms ($p<0.001$), which was not significantly reversible upon withdrawal of Ca^{2+}. Withdrawal of Ca^{2+} resulted in a reduction in Tau_{Rec} to 35.0 ± 11.1 ms (n.s., $p=0.17$), which was significantly different from the initial Ca^{2+}-free condition ($p<0.05$). The internal application of 10 µM Ca^{2+} in Kv4.2/DPP6/KChIP3 channel complexes showed a significant increase in Tau_{Rec} by a factor of approximately 1.19 from 54.8 ± 11.0 ms to 64.5 ± 11.4 ms ($p<0.01$), and withdrawal of Ca^{2+} had no significant effect. The relative changes in Tau_{Rec} between each condition showed that 10 µM Ca^{2+} reduced Tau_{Rec} in all studied groups. Kv4.2/DPP6/KChIP2 channel complexes showed the strongest effect, which was significantly different from both Kv4.2/DPP6 and Kv4.2/DPP6/KChIP3 channel complexes, indicating that Ca^{2+}-dependent effects differ between KChIP families. (Figure 4.12B).

Voltage dependence of steady-state inactivation

Furthermore, an examination of the voltage dependence of steady-state inactivation showed a $V_{1/2\ inact}$ of -95.2 ± 3.6 mV (n = 9) for Kv4.2/DPP6 in the absence of Ca^{2+}. Kv4.2/DPP6/KChIP2 showed a more positive $V_{1/2\ inact}$ of -82.3 ± 3.2 mV (n = 7) and Kv4.2/DPP6/KChIP3 showed a $V_{1/2\ inact}$ of -95.6 ± 3.8 mV (n = 7). Upon application of 10 µM Ca^{2+}, the voltage dependence of inactivation shifted significantly to a more negative potential for all channel complexes. Kv4.2/DPP6 shifted by -3.7 mV from -95.2 ± 3.6 mV to -98.9 ± 3.7 mV ($p<0.001$). Kv4.2/DPP6/KChIP2 showed the strongest shift of -6.5 mV from -82.3 ± 3.2 mV to -89.3 ± 2.4 mV ($p<0.001$) and Kv4.2/DPP6/KChIP3 showed a shift in $V_{1/2\ inact}$ of -2.8 mV from -95.6 ± 3.8 to -98.4 ± 3.6 mV ($p<0.0001$). Although there were no significant differences in the absolute shifts in $V_{1/2\ inact}$ among each group, withdrawal of Ca^{2+} caused a significant shift to a more positive potential only in ternary complexes with KChIP3 ($p<0.01$).

Similar to the previous results, withdrawal of Ca^{2+} did not restore the initial value observed in condition (1) in the studied groups. For Kv4.2/DPP6 and Kv4.2/DPP6/KChIP2, the internal application of 10 µM Ca^{2+} had an irreversible effect on $V_{1/2\ inact}$, while Kv4.2/DPP6/KChIP3 channel complexes displayed a reversible effect but were significantly different from the control value. Among the studied groups, $V_{1/2\ inact}$ were in between the control value in condition (1) and condition (2). (Figure 4.13)

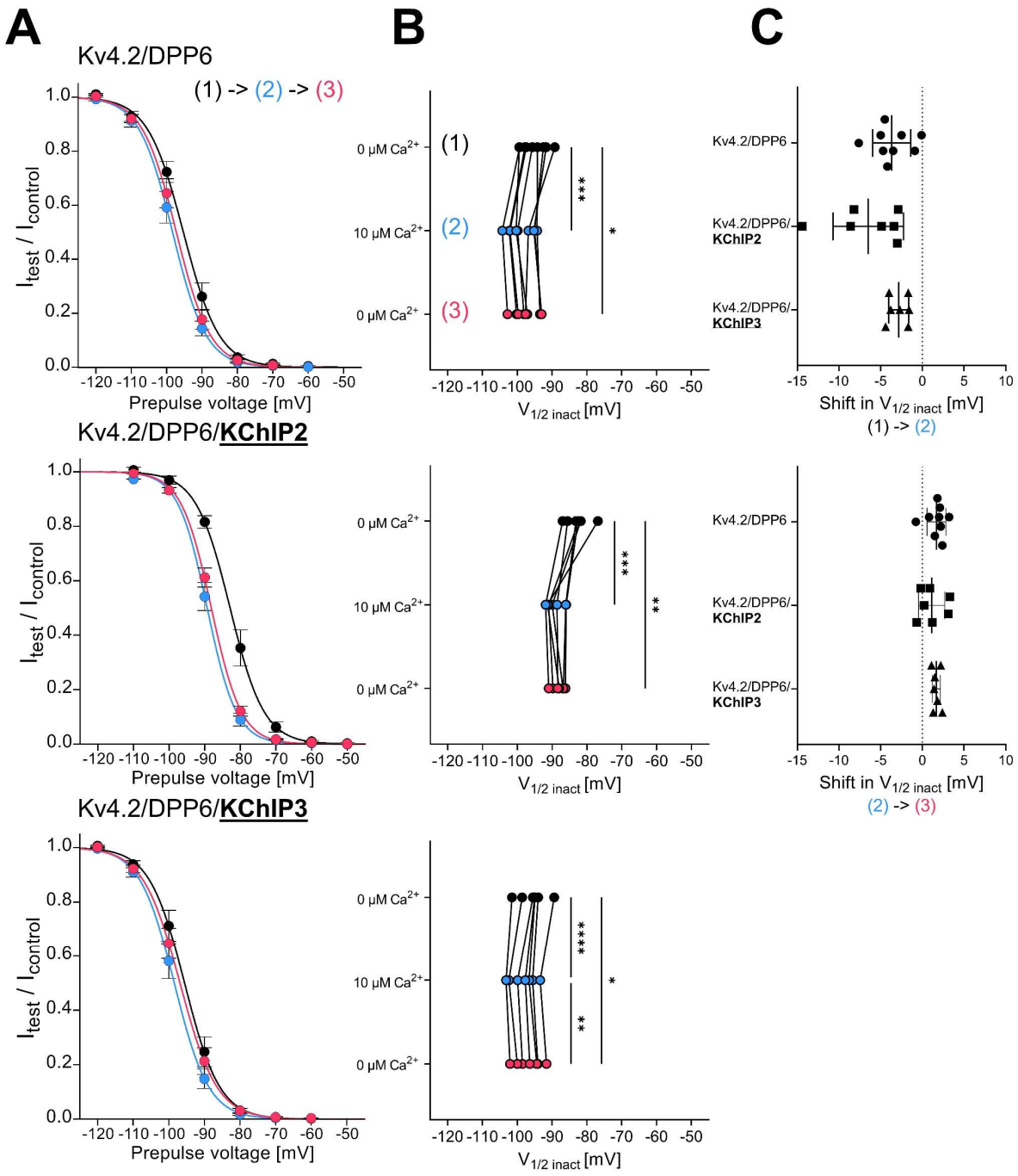

Figure 4.13: **Effects of internal Ca^{2+} on the voltage dependence of steady-state inactivation on Kv4.2/DPP6 channel complexes co-expressed with KChIP studied in *Xenopus* oocyte inside-out macro patches.**
(**A**) Voltage dependence of steady-state inactivation in Ca^{2+}-free solution (black, red) and in 10 µM Ca^{2+} solution (blue). (**B**) Data were fitted using a single Boltzmann fit. The individual $V_{1/2\ inact}$ values are shown as triplets. Triplets were analyzed using repeated measures ANOVA followed by a Tukey post hoc test. (**C**) Shift in $V_{1/2\ inact}$ when 10 µM Ca^{2+} were applied or withdrawn. Groups were analyzed using a one-way ANOVA followed by a Tukey post hoc test. *p<0.05, **p<0.01, *** p<0.001, ****p<0.0001

Table 4.5: **Electrophysiological properties and Ca^{2+}-dependent effects on Kv4.2 channel complexes studied in *Xenopus* oocyte inside-out macro patches.**
* indicate for significant Ca^{2+}-related effect.
# indicate for significant differences between both Ca^{2+}-free solution recordings (1) and (3).
K indicate for significant differences in effect between Kv4.2/DPP6/KChIP2 and Kv4.2/DPP6/KChIP3,
D indicate for significant differences between Kv4.2/DPP6 and Kv4.2/DPP6/KChIP2 or Kv4.2/DPP6/KChIP3.
All entries describe mean ± SD. One symbol : p<0.05, two symbols : p<0.01, three symbols : p<0.001, four symbols : p<0.0001.

	Tau1 [ms]	Rel. change Tau1	Tau2 [ms]	Rel. change Tau2	Tau_{Rec} [ms]	Rel. change Tau_{Rec}	$V_{1/2\ inact}$ [mV]	Shift in $V_{1/2\ inact}$ [mV]
Kv4.2/DPP6	(n = 12)				(n = 10)		(n = 9)	
(1) 0 µM Ca^{2+}	14.6 ± 1.3		241 ± 38		87.9 ± 22.2		-95.2 ± 3.6	
(2) 10 µM Ca^{2+}	15.9 ± 1.8	1.10 ± 0.12	309 ± 86	1.31 ± 0.41	96.6 ± 25.0	1.11 ± 1.18	-98.9 ± 3.7 ***	-3.7 ± 2.3
(3) 0 µM Ca^{2+}	14.8 ± 3.5	0.93 ± 0.17	257 ± 138	0.86 ± 0.42	89.8 ± 22.5	0.94 ± 0.10	-97.2 ± 3.5 #	1.7 ± 1.1
Kv4.2/DPP6/ KChIP2	(n = 8)				(n = 8)		(n = 7)	
(1) 0 µM Ca^{2+}	21.6 ± 4.8		93 ± 32		25.5 ± 7.4		-82.8 ± 3.2	
(2) 10 µM Ca^{2+}	20.6 ± 5.8	0.96 ± 0.23	93 ± 27	1.08 ± 0.42	40.8 ± 16.4 ***	1.60 ± 0.42 DD,K	-89.3 ± 2.4 ***	-6.5 ± 4.2
(3) 0 µM Ca^{2+}	15.7 ± 3.7 **,##	0.78 ± 0.10	83 ± 21	0.93 ± 0.27	35.0 ± 11.1	0.89 ± 0.15	-88.2 ± 1.7 ##	1.1 ± 1.6
Kv4.2/DPP6/ KChIP3	(n = 12)				(n = 9)		(n = 7)	
(1) 0 µM Ca^{2+}	32.0 ± 9.8		103 ± 23		54.8 ± 11.0		-95.6 ± 3.8	
(2) 10 µM Ca^{2+}	28.4 ± 9.0	0.90 ± 0.20 D	122 ± 42	1.25 ± 0.60	64.5 ± 11.4 **	1.19 ± 0.14	-98.4 ± 3.6 ****	-2.8 ± 1.2
(3) 0 µM Ca^{2+}	22.7 ± 7.1 **,####	0.81 ± 0.11	106 ± 35	0.92 ± 0.23	59.0 ± 12.3 #	0.91 ± 0.11	-96.7 ± 3.7 **,#	1.7 ± 0.5

4.4 Electrophysiological recordings in HEK293T cells

In order to gain a better understanding of the effects of Ca^{2+} on Kv4 channel complexes, the experiments presented previously were repeated in HEK293T inside-out patches. The previous experiments did not provide conclusive results, likely due to factors such as endogenous channel expression, a non-physiological low chloride concentration in recording solutions, and the use of non-mammalian model organism. Thus, it was important to examine the channel complexes in a more physiological environment.

Before continuing to investigate Ca^{2+}-related effects on Kv4.2 channel complexes, solutions were applied to HEK293T cells transfected with BK channels. BK channels consists of four alpha subunits forming one pore unit. Each alpha unit consists of seven transmembrane domains, which resemble those of voltage-gated K^+ channels. Additionally, a Ca^{2+}-sensing domain is located in the C-terminal region on the intracellular side. Application of Ca^{2+} shifted open probability to more negative potentials[51]. Their binding affinity has been determined between 1-10 µM Ca^{2+}, making it an ideal positive control for Ca^{2+} application effects.

In the following chapters, epitope-tagged constructs were utilized, allowing for the easy detection of transfected cells using simple fluorescent filter cubes. Only cells with an even distribution of Kv4.2 and KChIP along the cell membrane were selected for recording. Our results have already shown that epitope-tagging did not significantly alter channel kinetics or the effects of internally applied Ca^{2+}. Moreover, the effects of patch excision were examined.

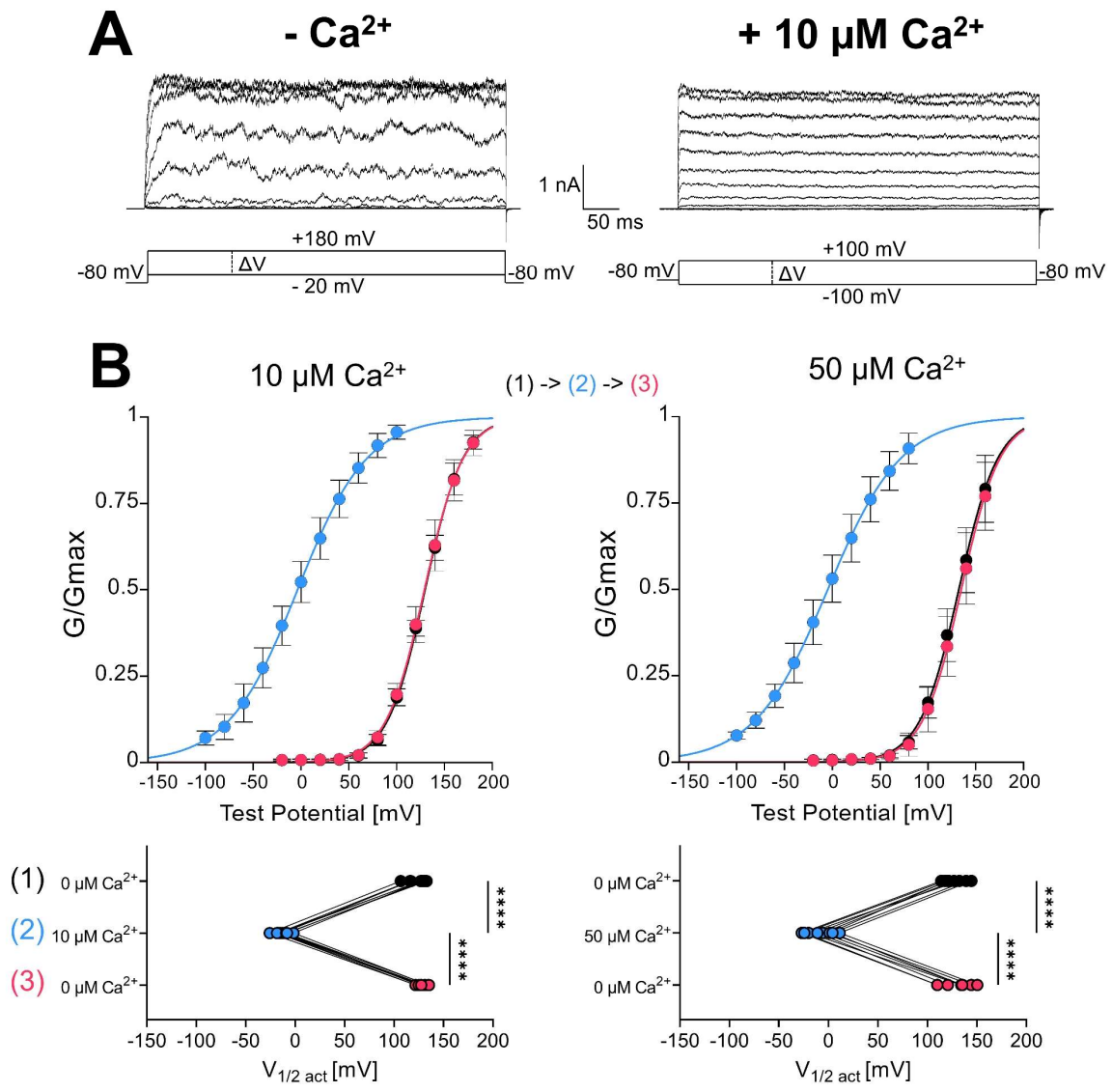

Figure 4.14: **Effects of internal Ca^{2+} application on the voltage dependence of activation of BK channels studied in HEK293T inside-out patches.**
(**A**) Representative current family of BK channels in HEK293 inside-out patches in Ca^{2+}-free solution and 10 µM Ca^{2+}.(**B**)Voltage dependence of activation of BK channels in Ca^{2+}-free solution (black, red) and in 10 or 50 µM Ca^{2+} (red). Voltage dependence of activation was calculated using a single Boltzmann fit and individual values are shown as triplets. Triplets were analyzed using repeated measures ANOVA followed by a Tukey post hoc test. ****p<0.0001.

In the present study, internal application of either 10 µM or 50 µM Ca^{2+} solution resulted in a shift in the activation potential of BK channels. In a Ca^{2+}-free environment, BK channels showed a half-maximal conductance ($V_{1/2\ act}$) at a potential of +128 ± 5 mV. Application of 10 µM Ca^{2+} led to a shift in $V_{1/2\ act}$ to -13.0 ± 7.1 mV (n = 9, p<0.0001). This effect was fully reversible when Ca^{2+} was depleted (p<0.0001). Similar effects were observed on the application of a 50 µM Ca^{2+} internal solution. (Figure 4.14).

4.4.1 Effect of patch excision on Kv4.2^{C} channel complexes in Ca^{2+}-free environment

Initially, HEK293T cells were recorded in the cell-attached configuration. Afterwards, patches were excised and recordings were repeated to determine the effects of removing a patch from the cytoplasm to the bath solution and perfused with Ca^{2+}-free internal solution. A high K^{+} solution (see Material & Methods) was used to record HEK cells in cell-attached configuration, which shifts the resting membrane potential to around 0 mV.

Macroscopic inactivation kinetics

A depolarizing voltage step from -100 mV to +40 mV showed a fast inactivation component Tau1 of 11.1 ± 3.6 ms and a slow inactivation component Tau2 of 359 ± 91 ms (n = 21) for Kv4.2^{C}/DPP6 channel complexes in the cell-attached configuration. Patch excision and perfusion with Ca^{2+}-free solution resulted in a significant reduction on both inactivation components and showed a Tau1 of 7.4 ± 2.2 ms ($p<0.0001$) and a Tau2 of 281 ± 155 ms ($p<0.05$). For Kv4.2^{C}/KChIP2^{R} channel complexes, a significant reduction in both inactivation time constants was also observed. Tau1 reduced from 45.5 ± 23.4 ms to 17.3 ± 6.3 ms ($p<0.01$) and Tau2 from 136 ± 52 ms to 80 ± 25 ms ($p<0.01$, n = 13). In ternary complexes, patch excision showed a significant decrease in Tau1 but no noticeable differences in Tau2. In Kv4.2^{C}/DPP6/KChIP2^{R} channel complexes, Tau1 decreased from 31.8 ± 14.1 ms to 20.8 ± 6.8 ms ($p<0.05$, n = 17) and in Kv4.2^{C}/DPP6/KChIP3^{R} channel complexes, Tau1 decreased from 56.8 ± 14.9 ms to 29.8 ± 9.1 ms ($p<0.0001$, n = 22). (Figure 4.15A)

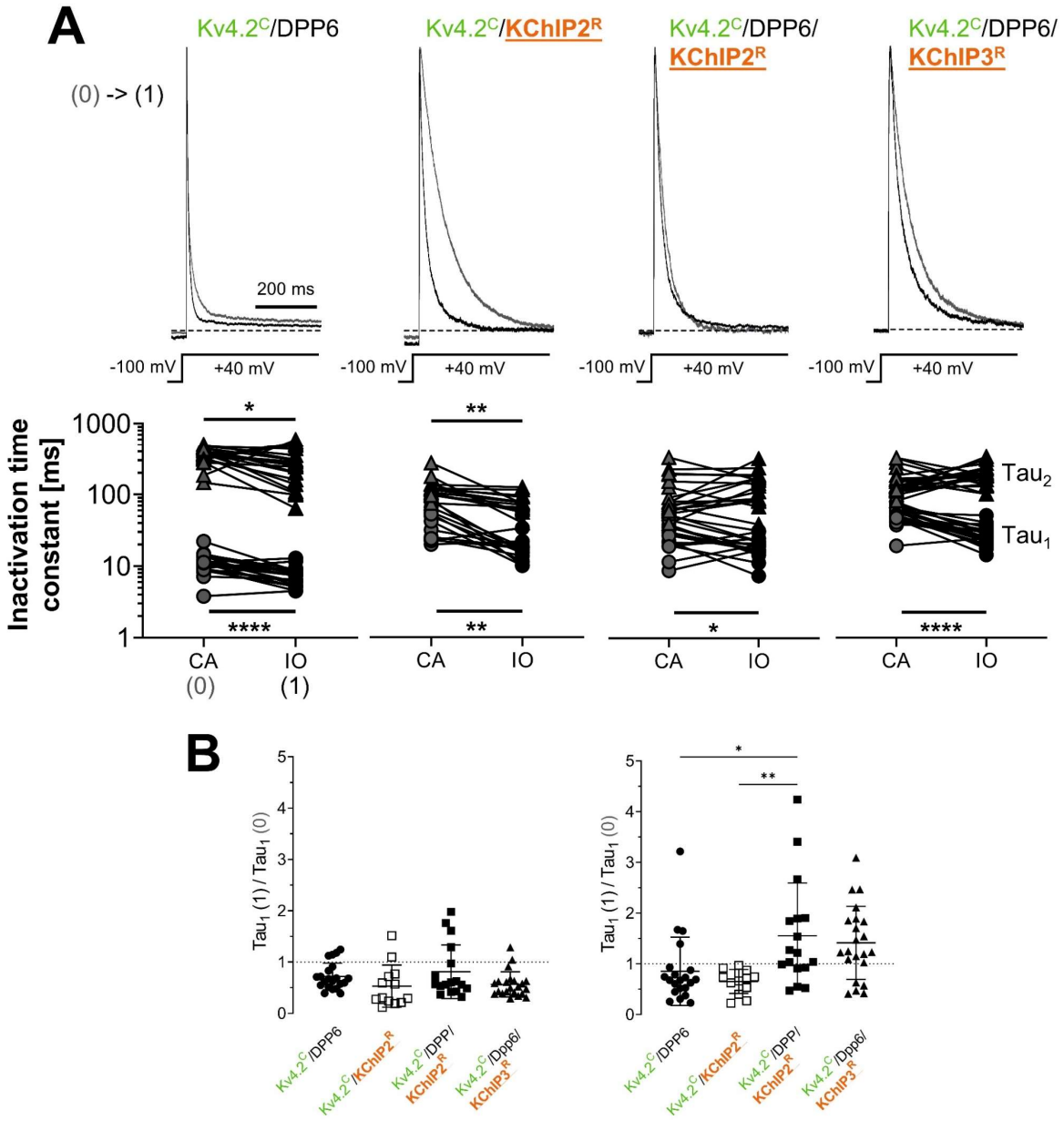

Figure 4.15: **Effects of patch excision on the macroscopic inactivation kinetics on Kv4.2^{C} channel complexes studied in HEK293T cells in cell-attached configuration to inside-out patches.**
(**A**) Normalized currents in cell-attached (**CA**) configuration (grey traces) and inside-out (**IO**) configuration perfused with Ca^{2+}-free internal solution (black). Inactivation components are shown as pairs where fast inactivation component Tau1 shown as circles and slow inactivation component Tau2 as triangles. Pairs were analyzed using ratio paired Students t-test. (**B**) Relative changes in Tau1 and Tau2 due to patch excision. Groups were analyzed using a one-way ANOVA followed by a Tukey post hoc test. *p<0.05, **p<0.01, ****p<0.0001.

The comparison of the relative changes in inactivation components between each condition resulted in no significant differences between the groups in Tau1. The relative change of Tau2, due to patch excision, resulted in opposite effects: Binary complexes decreased in Tau2, while ternary complexes increased in Tau2 (Figure 4.14B).

Recovery from inactivation

Patch excision resulted in a significant decrease in Tau_{Rec} for all studied groups. $Kv4.2^{C}$/DPP6 channel complexes showed the mildest effect, with a ~1.28-fold increase in Tau_{Rec} from 74.9 ± 16.8 ms to 93.3 ± 23.0 ms ($p<0.01$, n = 13). Involvement of KChIP drastically increased the observed effect, with the $Kv4.2^{C}$/$KChIP2^{R}$ channel complexes showing an increase in Tau_{Rec} from 37.2 ± 9.4 ms to 80.9 ± 34.5 ms ($p<0.0001$, n = 12). Ternary complexes showed the highest relative change in Tau_{Rec}, with a similar factorial increase of ~2.97. For the $Kv4.2^{C}$/DPP6/KChIP3 ternary complexes, Tau_{Rec} showed an increase from 20.8 ± 9.4 ms to 59.4 ± 24.2 ms ($p<0.0001$, n = 14) and for the $Kv4.2^{C}$/DPP6/KChIP2 ternary complexes, Tau_{Rec} showed an increase from 11.7 ± 2.8 ms to 33.9 ± 17.4 ms ($p<0.0001$, n = 15) (Figure 4.16 A/B). Examination of the relative changes revealed that the observed effect is heavily influenced by KChIP co-expression. Co-expression of $Kv4.2^{C}$/DPP6 together with either KChIP2 or KChIP3 significantly increased the relative effect ($p<0.001$) without a distinctive difference between KChIP families (Figure 4.16C).

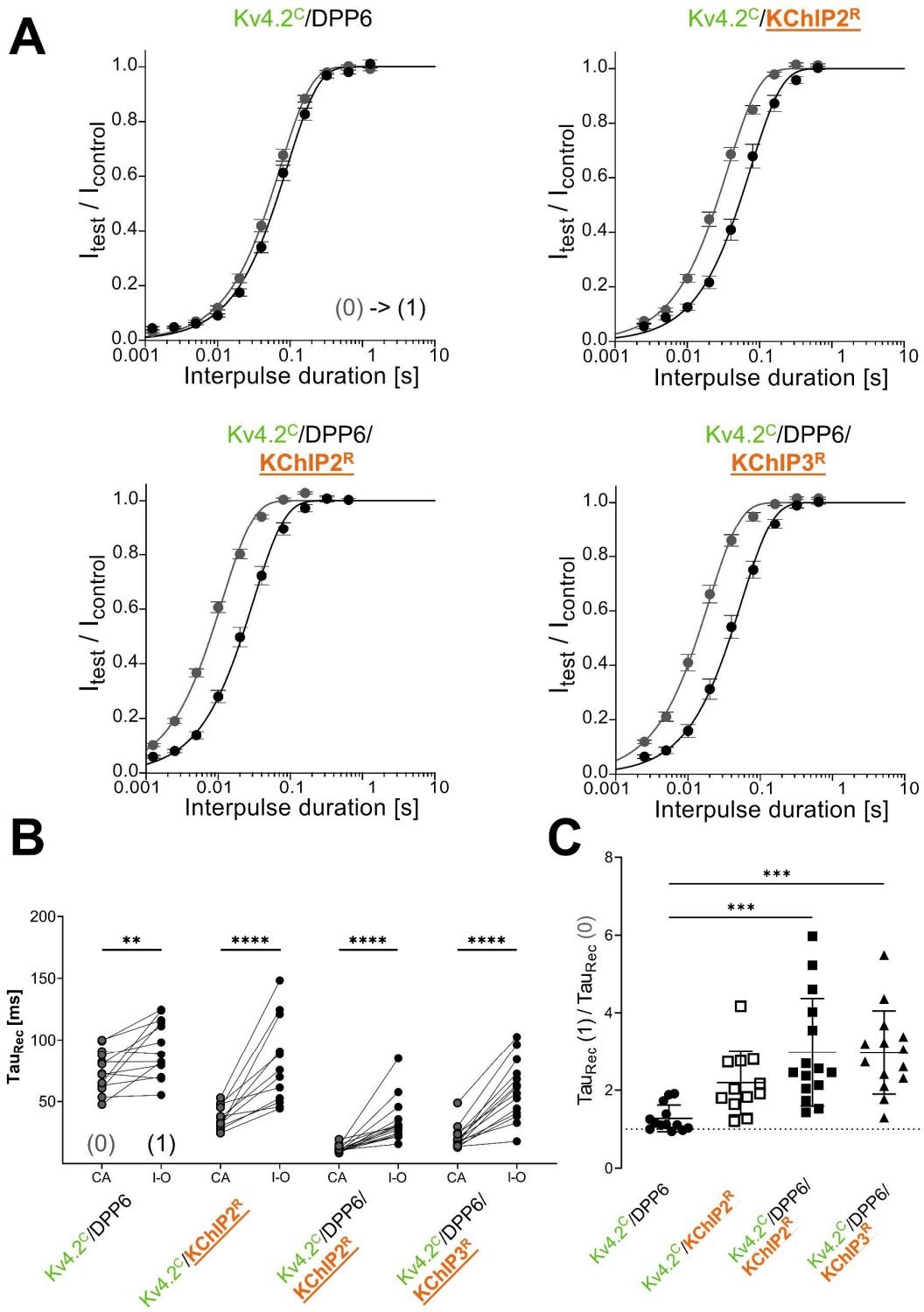

Figure 4.16: **Effects of patch excision on the recovery from inactivation on Kv4.2 channel complexes studied in HEK293T cells in cell-attached configuration to inside-out patches.** (**A**) Recovery from inactivation in cell-attached configuration (**CA**) (grey) and in inside-out configuration (**IO**) perfused with Ca^{2+}-free internal solution (black). (**B**) Data were analyzed using a single exponential fit and individual values are shown as pairs. Pairs were compared using a ratio paired Students t-test. (**C**) Relative changes in Tau_{Rec} due to patch excision. Groups were analyzed using one-way ANOVA followed by a Šídák multiple comparisons test. **p<0.01,***p<0.001, ****p<0.0001

Voltage dependence of steady-state inactivation

Focusing on the voltage dependence of inactivation, in all studied groups, the $V_{1/2\ inact}$ showed a shift to a more negative potential after patch excision. Kv4.2^{C}/DPP6 showed the least shift with -11.9 ± 5.1 mV from -78.7 ± 3.9 mV to -90.6 ± 5.7 mV ($p<0.0001$, $n = 14$). Kv4.2^{C}/KChIP2^{R} showed the strongest shift with -23.8 ± 6.0 mV from -59.9 ± 6.0 mV to -83.6 ± 4.5 mV ($p<0.0001$, $n = 10$). A negative shift of -19.9 ± 5.2 mV from -62.7 ± 3.6 mV to -82.6 ± 4.5 mV ($p<0.0001$, $n = 14$) was obtained for the ternary complex Kv4.2^{C}/KChIP2^{R}/DPP6. Similar for the KChIP3^{R} ternary complexes, the observed shift was -18.6 ± 5.7 mV from -72.3 ± 5.7 mV to -91.0 ± 7.7 mV ($p<0.0001$, $n = 22$ (Figure 4.17).

Similar to the recovery kinetics, the observed effect of patch excision was heavily influenced by KChIP co-expression, without observable differences between KChIP families.

Concluding so far, patch excision notably changed the biophysical properties of Kv4.2^{C} channel complexes. Patch excision showed an accelerated macroscopic inactivation and a decrease in the fast inactivation time constant Tau1 without notable differences among all studied groups. Additionally, the recovery from inactivation was slower, and a negative shift in the voltage dependence of steady-state inactivation was observed for all studied groups. The mildest effects were observed in binary complexes Kv4.2^{C}/DPP6, while co-expression with KChIP notably enhanced the effects without differences between KChIP2 and KChIP3.

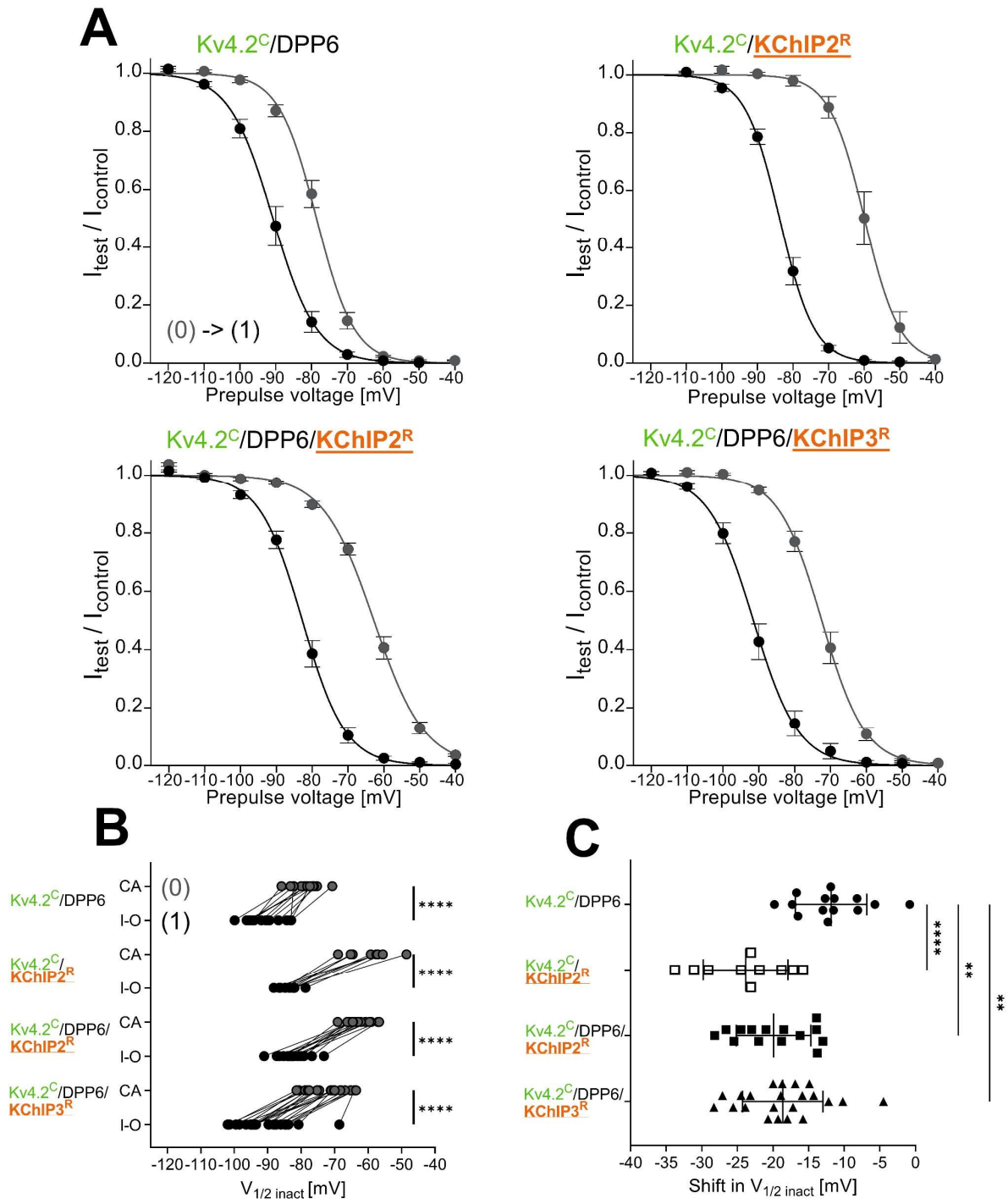

Figure 4.17: **Effects of patch excision on the voltage dependence of steady-state inactivation on Kv4.2 channel complexes studied in HEK293T cells in cell-attached configuration to inside-out patches.**
(**A**) Voltage dependence of steady-state inactivation in cell-attached configuration (**CA**) (grey) and in inside-out configuration (**IO**) perfused with Ca^{2+}-free internal solution (black). (**B**) Data were analyzed using a single Boltzmann fit and individual $V_{1/2\ inact}$ values are shown in pairs. Pairs were analyzed using paired Students t-test. (**C**) Shift $V_{1/2\ inact}$ due to patch excision. Groups were analyzed using one -way ANOVA followed by a Šídák multiple comparisons test. **p<0.01. ****p<0.0001

Table 4.6: **Electrophysiological properties and effects of patch excision on Kv4.2 channel complexes studied in HEK293T cells.**
* indicate for significant patch excision related effect.
^{K} indicate for significant differences between Kv4.2^{C}/DPP6/KChIP2^{R} and Kv4.2^{C}/DPP6/KChIP3^{R},
^{T} indicate for significant differences between Kv4.2^{C}/KChIP2^{R} and Kv4.2^{C}/DPP6/KChIP2^{R},
^{D} indicate for significant differences between Kv4.2^{C}/DPP6 and Kv4.2^{C}/DPP6/KChIP2 or Kv4.2^{C}/DPP6/KChIP3^{R}.
All entries describe mean ± SD. One symbol : p<0.05, two symbols : p<0.01, three symbols : p<0.001, four symbols : p<0.0001.

	Tau1 [ms]	**Rel. change Tau1**	**Tau2 [ms]**	**Rel. change Tau2**	**Tau_{Rec} [ms]**	**Rel. change Tau_{Rec}**	**$V_{1/2\ inact}$ [mV]**	**Shift in $V_{1/2\ inact}$ [mV]**
Kv4.2^{C}/DPP6	(n = 21)				(n = 13)		(n = 14)	
(0) Cell-attached	11.1 ± 3.6		359 ± 91		74.9 ± 16.8		-78.7 ± 3.9	
(1) Inside-out (ø Ca^{2+})	7.4 ± 2.2 ****	0.72 ± 0.26	281 ± 155 *	0.85 ± 0.67	93.3 ± 23.0 **	1.28 ± 0.34	-90.6 ± 5.7 ****	-11.9 ± 5.1
Kv4.2^{C}/KChIP2^{R}	(n = 13)				(n = 12)		(n = 10)	
(0) Cell-attached	45.5 ± 23.4		134 ± 52		37.2 ± 9.4		-59.9 ± 6.0	
(1) Inside-out (ø Ca^{2+})	17.3 ± 6.3 **	0.53 ± 0.41	80 ± 25 **	0.65 ± 0.24	80.9 ± 34.5 ****	2.19 ± 0.82	-83.7 ± 2.8 ****	-23.8 ± 6.0 DDDD
Kv4.2^{C}/DPP6/ KChIP2^{R}	(n = 17)				(n = 15)		(n = 14)	
(0) Cell-attached	31.8 ± 14.1		132 ± 93		11.7 ± 2.8		-62.7 ± 3.6	
(1) Inside-out (ø Ca^{2+})	20.8 ± 6.8 *	0.81 ± 0.52	159 ± 82	1.55 ± 1.04 TT,D	33.9 ± 17.4 ****	2.98 ± 1.39 DD	-82.6 ± 4.5 ****	-19.9 ± 5.2 DD
Kv4.2^{C}/DPP6/ KChIP3^{R}	(n = 22)				(n = 14)		(n = 22)	
(0) Cell-attached	56.8 ± 14.9		179 ± 80		20.8 ± 9.4		-72.3 ± 5.7	
(1) Inside-out (ø Ca^{2+})	29.8 ± 9.1 ****	0.56 ± 0.25	213 ± 71	1.41 ± 0.72	59.4 ± 24.2 ****	2.97 ± 1.07 DD	-91.0 ± 7.7 ****	-18,6 ± 5,7 DD

4.4.2 Ca^{2+}-related effects on Kv4.2 channel complexes in HEK293T inside-out patches

This chapter will focus on the Ca^{2+}-induced effects on inside-out patches from HEK293T cells. The currents from excised patches were first recorded in Ca^{2+}-free internal solution before 10 µM or 50 µM Ca^{2+} internal solution were applied and recorded again. Lastly, patches were perfused again with Ca^{2+}-free internal solution, and currents were recorded a third time as a second control.

Macroscopic inactivation kinetics in 10 µM Ca^{2+}

The macroscopic inactivation kinetics of the binary complex $Kv4.2^{C}$/DPP6 showed a fast inactivation time constant Tau1 of 6.8 ± 2.0 ms and a slow inactivation time constant Tau2 of 360 ± 100 ms (n = 16). No observable effects were present for both inactivation time constants when either Ca^{2+} was applied or depleted again, but overall, Tau1 significantly increased when going from the starting condition(1) to the final condition (3). $Kv4.2^{C}$/$KChIP2^{R}$ showed a decrease of Tau1 from 19.3 ± 7.1 ms to 15.6 ± 4.6 ms ($p<0.05$, n = 13) ms after application of 10 µM Ca^{2+} while Tau2 remained unaffected.

In ternary $Kv4.2^{C}$/DPP6/$KChIP2^{R}$ complexes, application of 10 µM Ca^{2+} led to a decrease of Tau1 from 18.6 ± 4.1 ms to 15.5 ± 5.2 ms ($p<0.01$) and no effect was present with the depletion of Ca^{2+}. For Tau2 no notable effects were observed when either Ca^{2+} was applied or depleted again, but overall, Tau2 significantly increased when going from the starting condition(1) to the final condition (3).

Ternary complexes $Kv4.2^{C}$/DPP6/$KChIP3^{R}$ showed a decrease of Tau1 from 28.5 ± 10.0 ms to 24.6 ± 8.7 ms ($p<0.01$, n = 26) and was unaffected with the depletion of Ca^{2+}. Tau2 remained unaffected from Ca^{2+} application and depletion. (Figure 4.18)

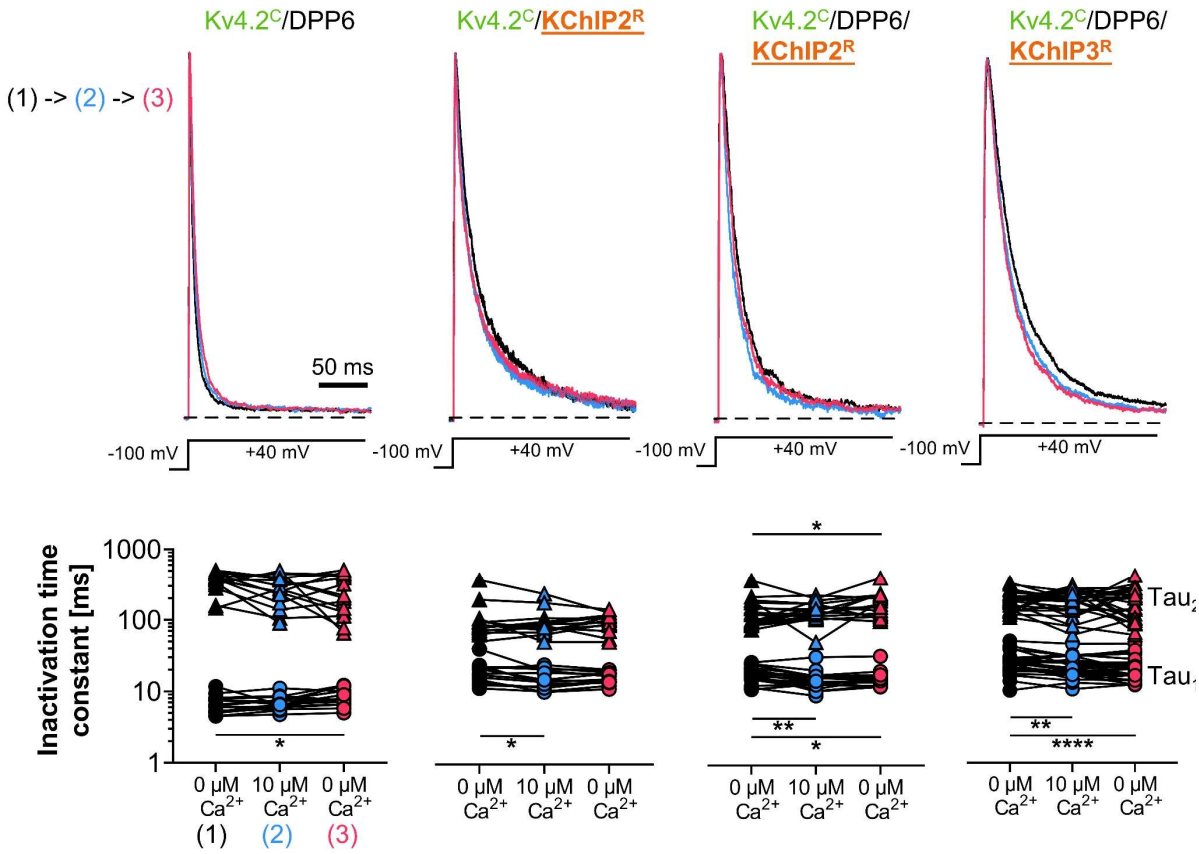

Figure 4.18: **Effects of internal 10 µM Ca^{2+} on the macroscopic current inactivation on $Kv4.2^C$ channel complexes studied in HEK293T inside-out patches.**
Normalized currents in Ca^{2+}-free solution (black and red trace) and 10 µM Ca^{2+} solution (blue trace). Inactivation kinetics were analyzed using a double exponential fitting procedure. Individual values are shown in triplets from 0 µM Ca^{2+} (1) to 10 µM Ca^{2+} (2) to 0 µM Ca^{2+} (3). Triplets were analyzed using repeated measures ANOVA (or mixed effects analysis, when values are missing) with a Tukey post hoc test. *p<0.05, **p<0.01, ****p<0.0001.

Further investigation of the relative changes showed that KChIP co-expression had a dominant effect on the Ca^{2+}-mediated reduction in Tau1. In the presence of KChIP3, however, a reduction of Tau1 was observed with depletion of Ca^{2+}.

No noticeable differences were observed in the relative change of Tau2 among the studied groups. (Figure 4.19)

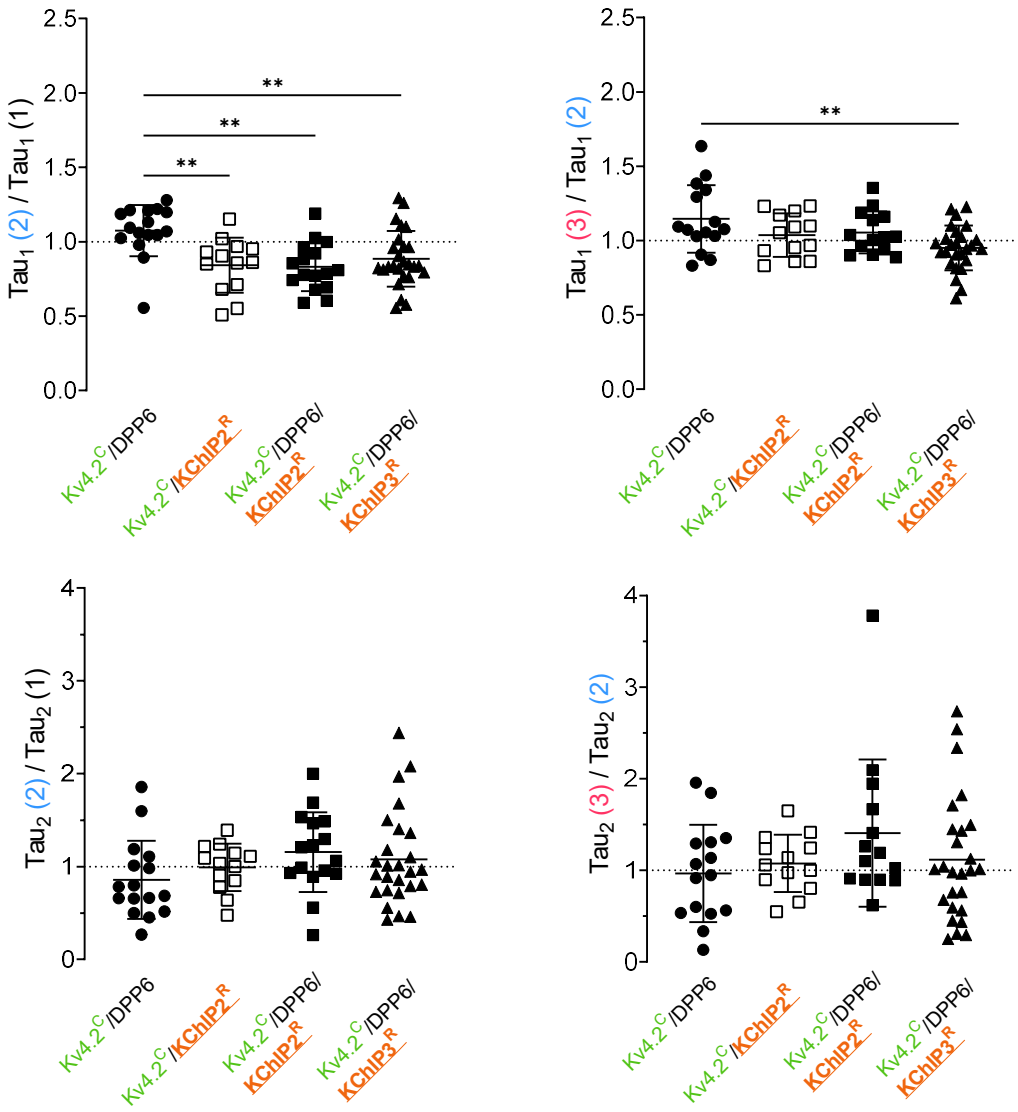

Figure 4.19: **Relative changes in macroscopic inactivation kinetics of Kv4.2^{C} channel complexes studied in HEK293T inside-out patches.**
Inactivation time constant pairs were put in relation due to application or withdrawal of 10 µM Ca^{2+}. The resulting relative changes in inactivation kinetics were analyzed using one-way ANOVA followed by a Tukey post hoc test. **p<0.01

Recovery from inactivation in 10 µM Ca^{2+}

Internal application of 10 µM Ca^{2+} on the binary complexes $Kv4.2^{C}$/DPP6 resulted in a significant increase of Tau_{Rec} from 94.9 ± 26.5 ms to 118 ± 31 ms ($p<0.05$, n = 9) which persisted when Ca^{2+} was depleted. $Kv4.2^{C}$/$KChIP2^{R}$ channel complexes showed a Tau_{Rec} of 59.8 ± 20.1 ms and application of 10 µM Ca^{2+} did not influence Tau_{Rec}. However, the depletion of Ca^{2+} led to a substantial increase in Tau_{Rec} from 58.9 ± 16.7 ms to 69.9 ± 21.3 ms ($p<0.001$, n = 13). For ternary complexes $Kv4.2^{C}$/DPP6/$KChIP2^{R}$, application of 10 µM Ca^{2+} resulted in a significant increase in Tau_{Rec} from 28.3 ± 8.0 ms to 35.6 ± 8.6 ms ($p<0.05$, n = 11) and for $Kv4.2^{C}$/DPP6/$KChIP3^{R}$ channel complexes, neither application nor depletion of Ca^{2+} altered the recovery from inactivation (n = 26).

Looking further into their relative changes in Tau_{Rec}, the observed effects were present with the co-expression of DPP6. $KChIP2^{R}$ co-expression did not influence the Ca^{2} induced effects, and the effect in $Kv4.2^{C}$/DPP6/$KChIP2^{R}$ channel complexes seemed to be mostly mediated through DPP6. $KChIP3^{R}$, however, did seem to suppress the Ca^{2+}-induced effect in ternary complexes. (Figure 4.20)

Voltage dependence of steady-state inactivation in 10 µM Ca^{2+}

For the voltage dependence of steady-state inactivation, $Kv4.2^{C}$/DPP6 channel complexes showed a half maximal potential $V_{1/2\ inact}$ of -89.9 ± 5.1 mV and the application of 10 µM Ca^{2+} shifted $V_{1/2\ inact}$ negative to -91.8 ± 5.0 mV ($p<0.05$, n = 10). Depletion of Ca^{2+} did not show any notable effect. For $Kv4.2^{C}$/$KChIP2^{R}$ and $Kv4.2^{C}$/DPP6/$KChIP2^{R}$, no notable Ca^{2+}-induced effects were observed. However, internal application of 10 µM Ca^{2+} on $Kv4.2^{C}$/DPP6/KChIP3 channel complexes resulted in a negative shift in $V_{1/2\ inact}$ from -92.5 ± 6.1 mV to -94.1 ± 5.6 mV, but no noticeable effect was present when Ca^{2+} was depleted. ($p<0.05$, n = 21). The comparison of their shift in $V_{1/2\ inact}$ showed no notable differences among the studied groups. (Figure 4.21)

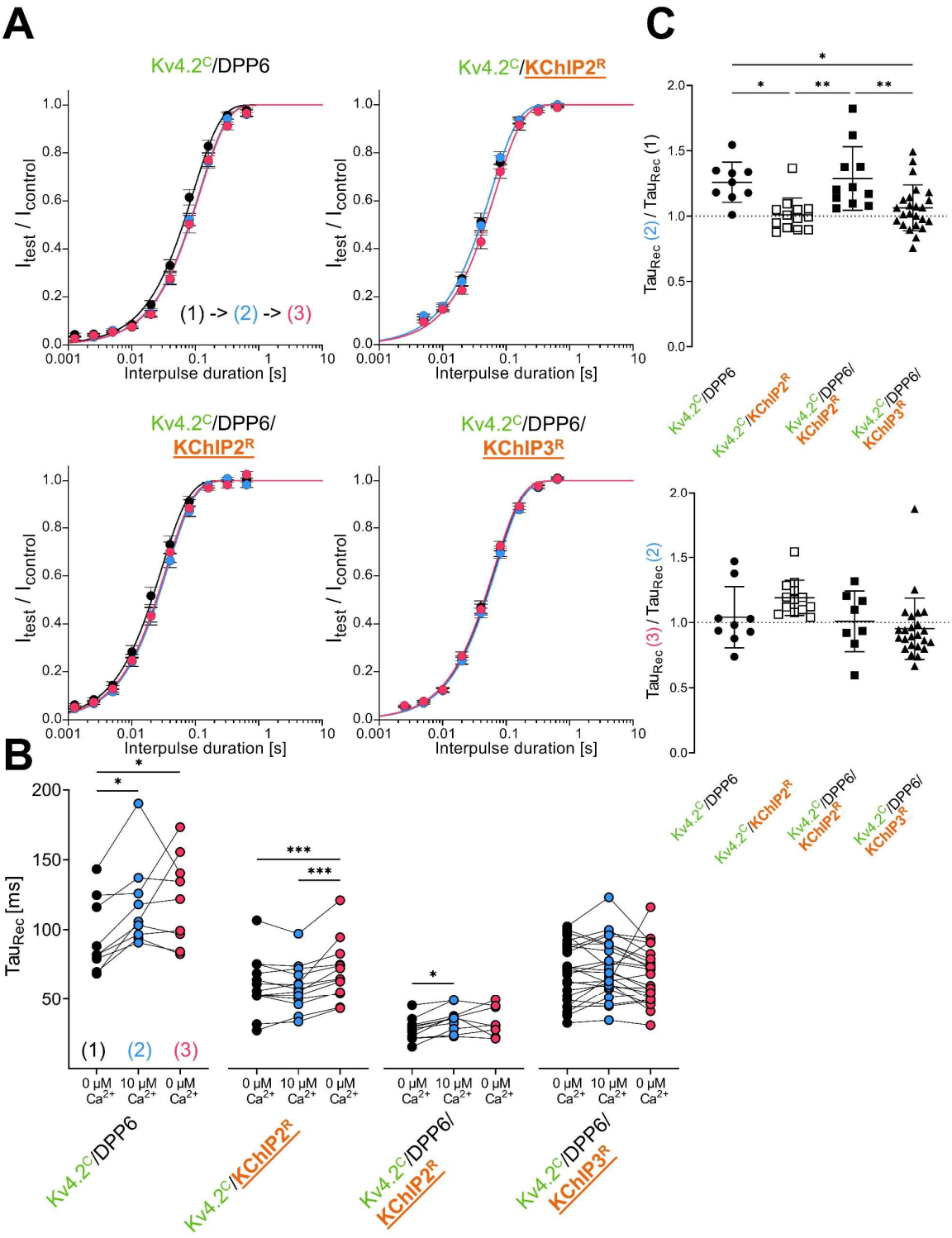

Figure 4.20: **Effects of internal Ca^{2+} on the recovery from inactivation on Kv4.2^{C} channel complexes studied in HEK293T inside-out patches.**
(**A**) Recovery from inactivation in Ca^{2+}-free solution (black, red) and 10 µM Ca^{2+} (blue).
(**B**) Recovery from inactivation were analyzed using single exponential fit and individual values are show in triplets. Triplets were analyzed using repeated measures ANOVA (or mixed effects analysis, when values are missing) followed by Tukey post hoc test. (**C**) Relative change in Tau_{Rec} values when 10 µM Ca^{2+} was applied or withdrawn. Groups were analyzed using one-way ANOVA followed by a Šídák multiple comparisons test. *p<0.05, **p<0.01, ***p<0.001

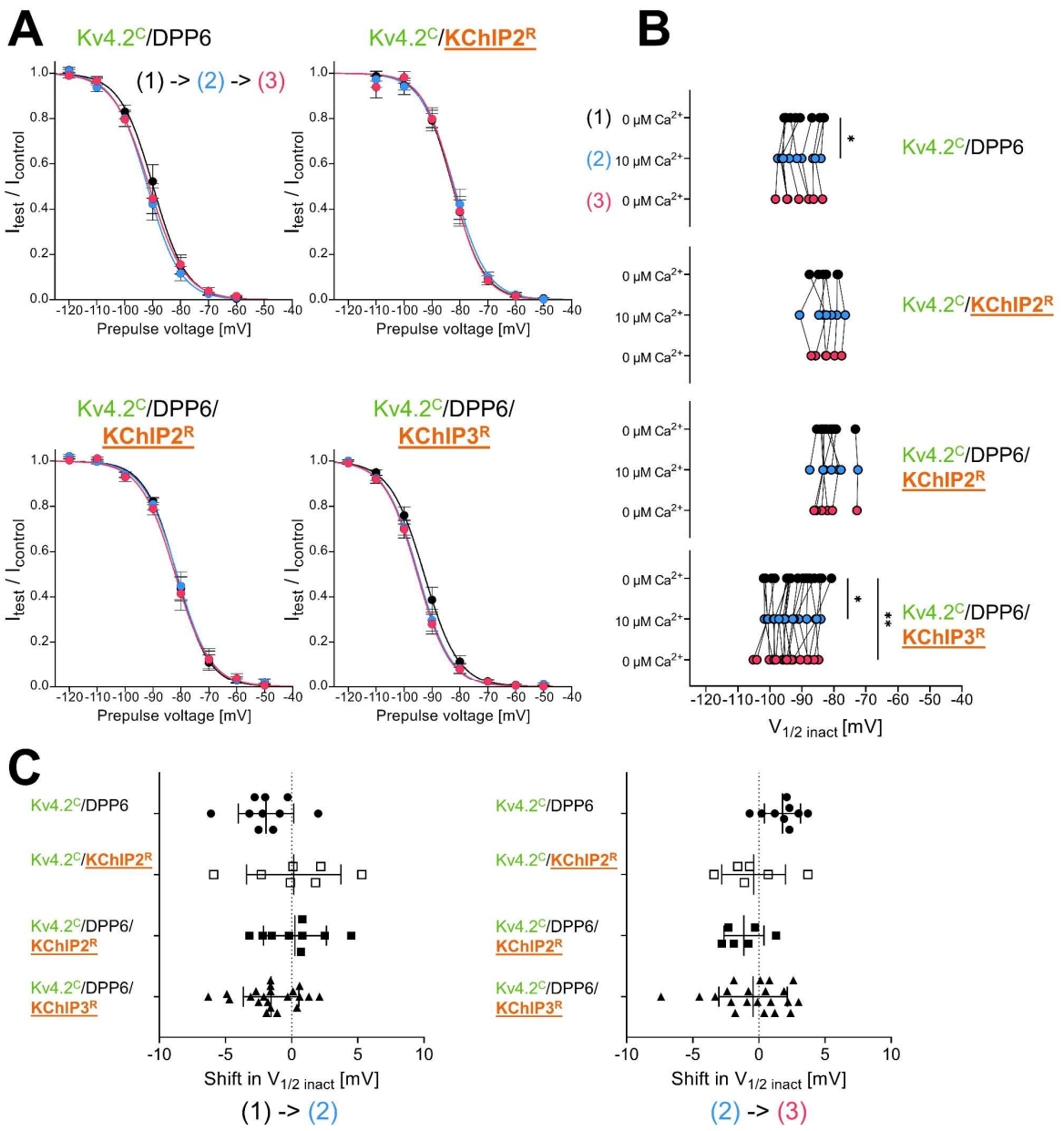

Figure 4.21: **Effects of internal Ca^{2+} on the voltage dependence of steady-state inactivation in Kv4.2^{C} channel complexes studied in HEK293T inside-out patches.**
(**A**) Voltage dependence of steady-state inactivation in Ca^{2+}-free solution (black, red) and 10 µM Ca^{2+}. **(B**) Data were analyzed using a single Boltzmann fit and individual $V_{1/2\ inact}$ values are shown in triplets. Triplets were analyzed using repeated measures ANOVA (or mixed effects analysis, when values are missing) followed by Tukey post hoc test. (**C**) Shift $V_{1/2\ inact}$ due to application or withdrawal of 10 µM Ca^{2+}. Groups were analyzed using one-way ANOVA followed by a Šídák multiple comparisons test. *p<0.05, **p<0.01

Table 4.7: **Electrophysiological properties and effects of 10 µM Ca^{2+} on Kv4.2 channel complexes studied in HEK293T cells inside-out patches.**
Number of experiments may vary due to patch breakage. If not otherwise stated number count is displayed at the top of the column of values.
* indicate for significant Ca^{2+}-related effect.
# indicate for significant differences between both Ca^{2+}-free solution recordings (1) and (3).
K indicate for significant differences between $Kv4.2^C$/DPP6/$KChIP2^R$ and $Kv4.2^C$/DPP6/$KChIP3^R$,
T indicate for significant differences between $Kv4.2^C$/$KChIP2^R$ and $Kv4.2^C$/DPP6/$KChIP2^R$,
D indicate for significant differences between $Kv4.2^C$/DPP6 and $Kv4.2^C$/DPP6/KChIP2 or $Kv4.2^C$/DPP6/$KChIP3^R$.
All entries describe mean ± SD. One symbol : p<0.05, two symbols : p<0.01, three symbols : p<0.001, four symbols : p<0.0001.

	Tau1 [ms]	**Rel. change Tau1**	**Tau2 [ms]**	**Rel. change Tau2**	**Tau_{Rec} [ms]**	**Rel. change Tau_{Rec}**	**$V_{1/2\ inact}$ [mV]**	**Shift in $V_{1/2\ inact}$ [mV]**
$Kv4.2^C$/DPP6	(n = 16)				(n = 9)		(n = 10)	
(1) 0 µM Ca^{2+}	6.8 ± 2.0		36 ± 100		94.9 ± 26.5		-89.9 ± 5.1	
(2) 10 µM Ca^{2+}	7.1 ± 1.6	1.07 ± 0.17	295 ± 129	0.86 ± 0.42	118 ± 31 *	1.26 ± 0.15	-91.8 ± 5.0 *	-1.9 ± 2.1
(3) 0 µM Ca^{2+}	8.1 ± 2.1 # (n = 15)	1.15 ± 0.23	276 ± 160	0.97 ± 0.53	121 ± 33 #	1.04 ± 0.24	-90.9 ± 4.9 (n = 9)	1.8 ± 1.4
$Kv4.2^C$/$KChIP2^R$	(n = 13)				(n = 13)		(n = 7)	
(1) 0 µM Ca^{2+}	19.3 ± 7.1		107 ± 81		59.8 ± 20.1		-82.6 ±3.2	
(2) 10 µM Ca^{2+}	15.6 ± 4.6 *	0.84 ± 0.18 DD	96 ± 49	0.99 ± 0.26	58.9 ± 16.7	1.01 ± 0.13 D	-82.4 ± 4.6	0.2 ± 3.6
(3) 0 µM Ca^{2+}	15.7 ± 3.0	1.04 ± 0.15	94 ± 26	1.08 ± 0.31	69.9 ± 21.3 ***,###	1.19 ± 0.24	-82.5 ± 3.6 (n = 6)	-0.4 ± 2.4
$Kv4.2^C$/DPP6/ $KChIP2^R$	(n = 16)				(n = 11)		(n = 9)	
(1) 0 µM Ca^{2+}	18.6 ± 4.1		145 ± 75		28.3 ± 8.0		-81.3 ± 3.6	
(2) 10 µM Ca^{2+}	15.5 ± 5.2 **	0.83 ± 0.16 DD	146 ± 44	1.16 ± 0.43	35.6 ± 8.6 *	1.29 ± 0.24 TT	-81.0 ± 4.4	0.2 ± 2.4
(3) 0 µM Ca^{2+}	16.6 ± 5.1 # (n = 14)	1.06 ± 0.14	190 ± 79 #	1.41 ± 0.81	34.1 ± 10.8 (n = 8)	1.01 ± 0.23	-81.7 ± 4.9 (n = 6)	-1.1 ± 1.5
$Kv4.2^C$/DPP6/ $KChIP3^R$	(n = 26)				(n = 24)		(n = 21)	
(1) 0 µM Ca^{2+}	28.5 ± 10.0		215 ± 67		70.0 ± 21.7		-92.5 ± 6.1	
(2) 10 µM Ca^{2+}	24.6 ± 8.7 **	0.89 ± 0.19 DD	218 ± 81	1.08 ± 0.51	72.7 ± 20.7	1.06 ± 0.18 D,KK	-94.1 ± 5.6 *	-1.6 ± 2.1
(3) 0 µM Ca^{2+}	23.4 ± 9.4 ####	0.95 ± 0.15 DD	212 ± 106	1.12 ± 0.68	68.0 ± 20.2	0.95 ± 0.24	-94.5 ± 5.6 ##	-0.4 ± 2.5

Macroscopic inactivation kinetics in 50 µM Ca^{2+}

Following the application of higher Ca^{2+} concentrations on inside-out patches, binary complexes Kv4.2^{C}/DPP6, Kv4.2^{C}/KChIP2^{R}, and ternary complexes Kv4.2^{C}/DPP6/KChIP2^{R} were studied without KChIP3^{R} ternary complexes. The internal application of 50 µM Ca^{2+} did not induce any effects among the studied groups. Only for Kv4.2^{C}/DPP6 channel complexes, the application of 50 µM Ca^{2+} resulted in a decrease of Tau2 from 422 ± 177 ms to 331 ± 130 ms ($p<0.05$, n = 11). No other Ca^{2+}-induced effects were observed among the studied groups. For Kv4.2^{C}/DPP6/KChIP2^{R} channel complexes, no notable effects were observed for Tau2 when either Ca^{2+} was applied or depleted, but overall Tau2 significantly increased when going from the starting condition (1) to the final condition (3). (Figure 4.22)

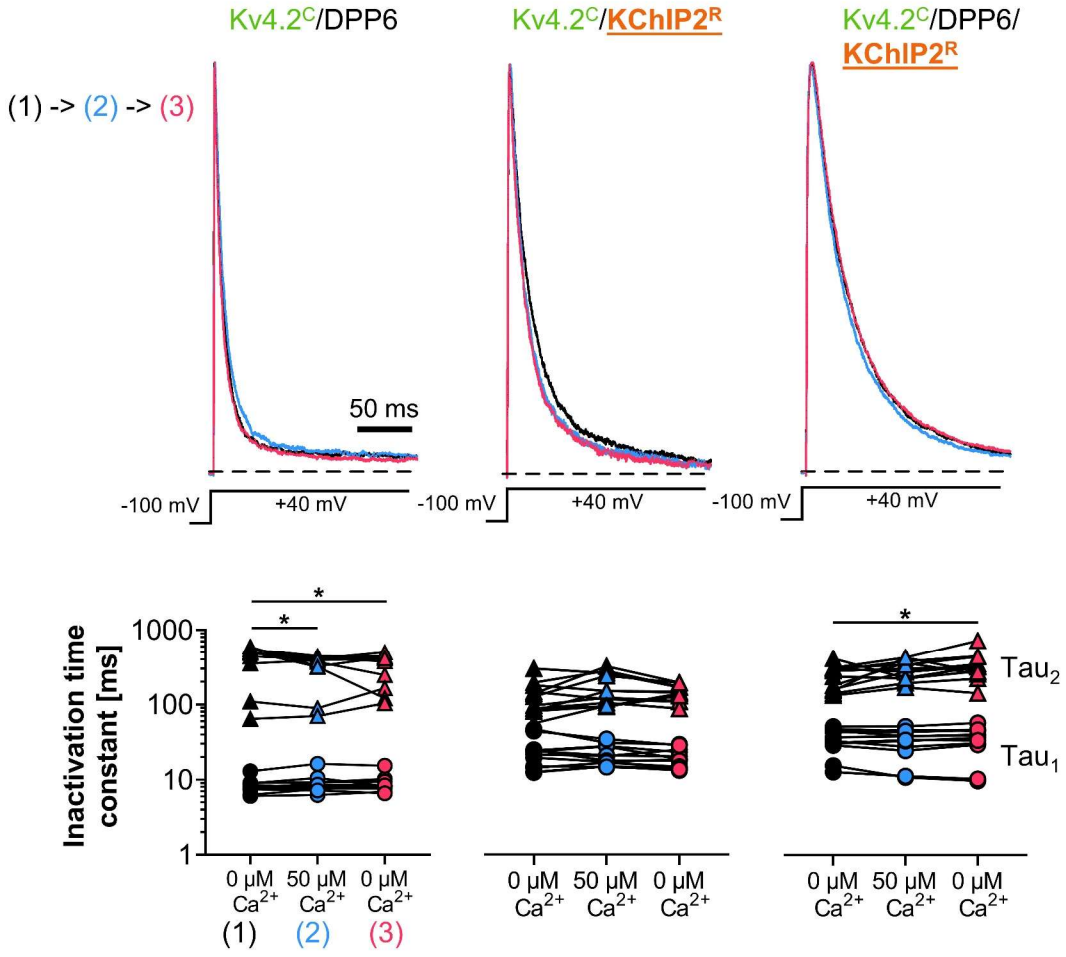

Figure 4.22: **Effects of internal Ca^{2+} on the macroscopic current inactivation in Kv4.2^{C} channel complexes studied in HEK293T inside-out patches.**
Normalized currents in Ca^{2+}-free solution (black and red trace) and 50 µM Ca^{2+} solution (blue trace). Inactivation kinetics were analyzed using a double exponential fitting procedure. Individual values are shown in triplets from 0 µM Ca^{2+} (1) to 50 µM Ca^{2+} (2) to 0 µM Ca^{2+} (3). Triplets were analyzed using repeated measures ANOVA (or mixed effects analysis, when values are missing) with a Tukey post hoc test. *$p<0.05$.

The comparison of the relative effects on the inactivation kinetics showed that the presence of KChIP2^{R} led to an increase in Tau2 when 50 µM Ca^{2+} were applied, while Kv4.2^{C}/DPP6 channel complexes led to a decrease in Tau2 when 50 µM Ca^{2+} were applied. (Figure 4.23)

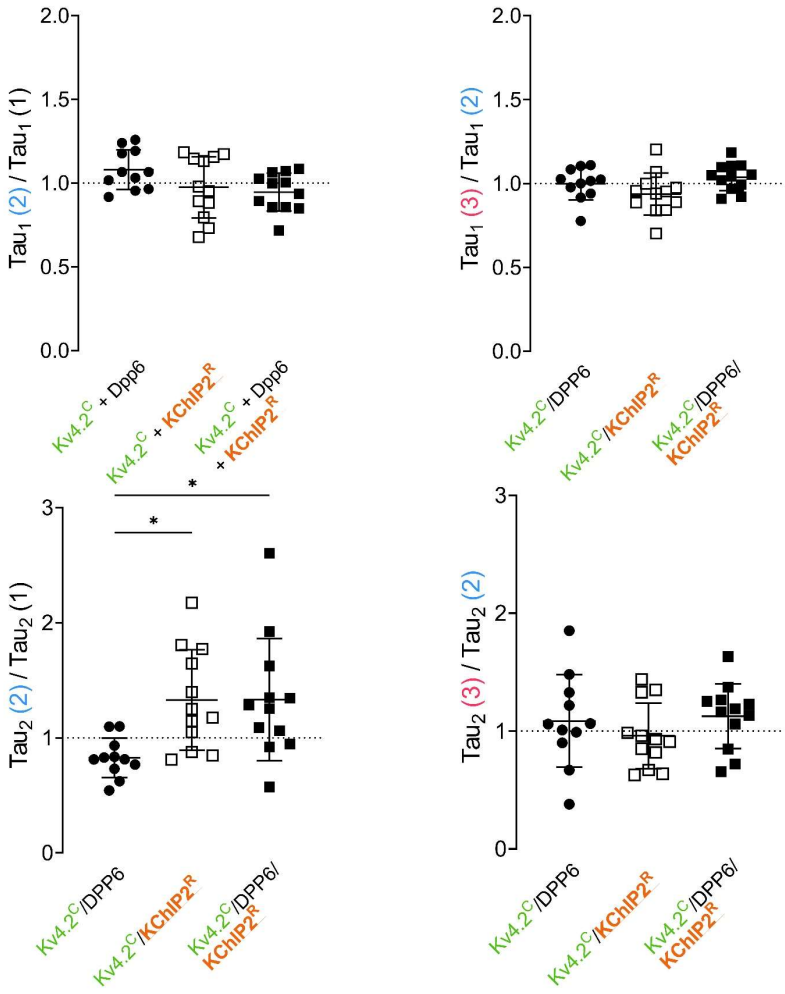

Figure 4.23: **Relative changes in macroscopic inactivation kinetics of Kv4.2^{C} channel complexes in HEK293T inside-out patches.**
Inactivation time constant pairs were put in relation due to application or withdrawal of 50 µM Ca^{2+}. The resulting relative changes in inactivation kinetics were analyzed using one-way ANOVA followed by a Tukey post hoc test. **p<0.01

Recovery from inactivation in 50 µM Ca^{2+}

Similar to the macroscopic inactivation kinetics, the application or depletion of 50 µM Ca^{2+} resulted in no observable effects on the recovery from inactivation among the studied groups. For ternary complex $Kv4.2^{C}$/DPP6/$KChIP2^{R}$, no notable effects were observed when either Ca^{2+} was applied or depleted, but overall Tau_{Rec} significantly increased when going from the starting condition (1) to the final condition (3).
The comparison of the relative changes in the recovery from inactivation within the groups revealed no significant differences (Figure 4.24).

Voltage dependence of steady-state of inactivation in 50 µM Ca^{2+}

Lastly, application of 50 µM Ca^{2+} resulted in no notable differences in the voltage dependence of steady-state inactivation for the binary complexes $Kv4.2^{C}$/DPP6 and $Kv4.2^{C}$/$KChIP2^{R}$. However, for ternary complexes $Kv4.2^{C}$/DPP6/$KChIP2^{R}$, application of 50 µM Ca^{2+} led to a positive shift in $V_{1/2\ inact}$ from -89.7 ± 2.6 mV to -87.9 ± 2.3 mV ($p<0.05$, $n = 6$). The comparison of the shift in $V_{1/2\ inact}$ showed opposite effects. Binary complex $Kv4.2^{C}$/DPP6 tended to a negative shift in $V_{1/2\ inact}$, while the presence of $KChIP2^{R}$ as binary as well as ternary complexes tended to a positive shift in $V_{1/2\ inact}$. (Figure 4.25)

In summary, the internal application of 10 µM Ca^{2+} showed a decrease in Tau1 in $Kv4.2^{C}$ channel complexes with the presence of either $KChIP2^{R}$ or $KChIP3^{R}$ while a higher Ca^{2+} concentration of 50 µM showed no notable differences in macroscopic current inactivation. Application of 10 µM Ca^{2+} resulted in a slowing in the recovery from inactivation in the presence of and the presence of $KChIP2^{R}$ had no notable influence on the observed effect. However, in the presence of $KChIP3^{R}$ as ternary complexes, the decrease in Tau_{Rec} remained absent in 10 µM Ca^{2+}. In addition, the application of 50 µM Ca^{2+} had no effect on the recovery from inactivation. Finally, the shift in the voltage dependence of inactivation was unaffected in 10 µM Ca^{2+} and showed no notable differences among the studied groups. However, the application of 50 µM Ca^{2+} resulted in a positive shift in $V_{1/2\ inact}$ in the presence of $KChIP2^{R}$.

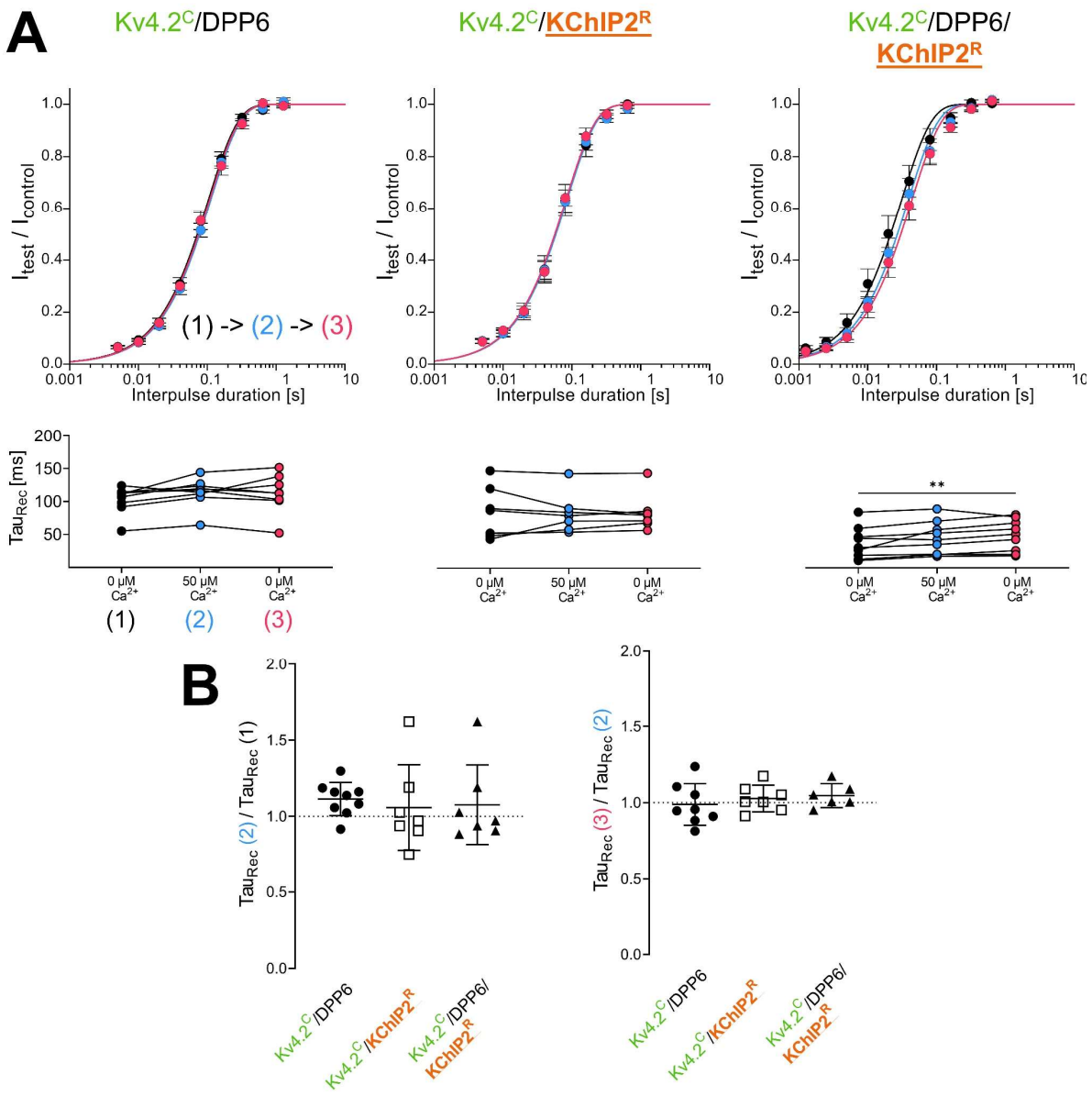

Figure 4.24: **Effects of 50 µM internal Ca^{2+} on the recovery from inactivation on $Kv4.2^C$ channel complexes studied in HEK293T inside-out patches.**
(**A**) Recovery from inactivation in Ca^{2+}-free solution (black, red) and 50 µM Ca^{2+} (blue). Data were analyzed using single exponential fit and individual values are show in triplets. Triplets were analyzed using repeated measures ANOVA (or mixed effects analysis, when values are missing) followed by Tukey post hoc test. (**B**) Relative change in Tau_{Rec} values when 50 µM Ca^{2+} was applied or withdrawn. Groups were analyzed using one-way ANOVA followed by a Tukey post hoc test. *p<0.05, **p<0.01.

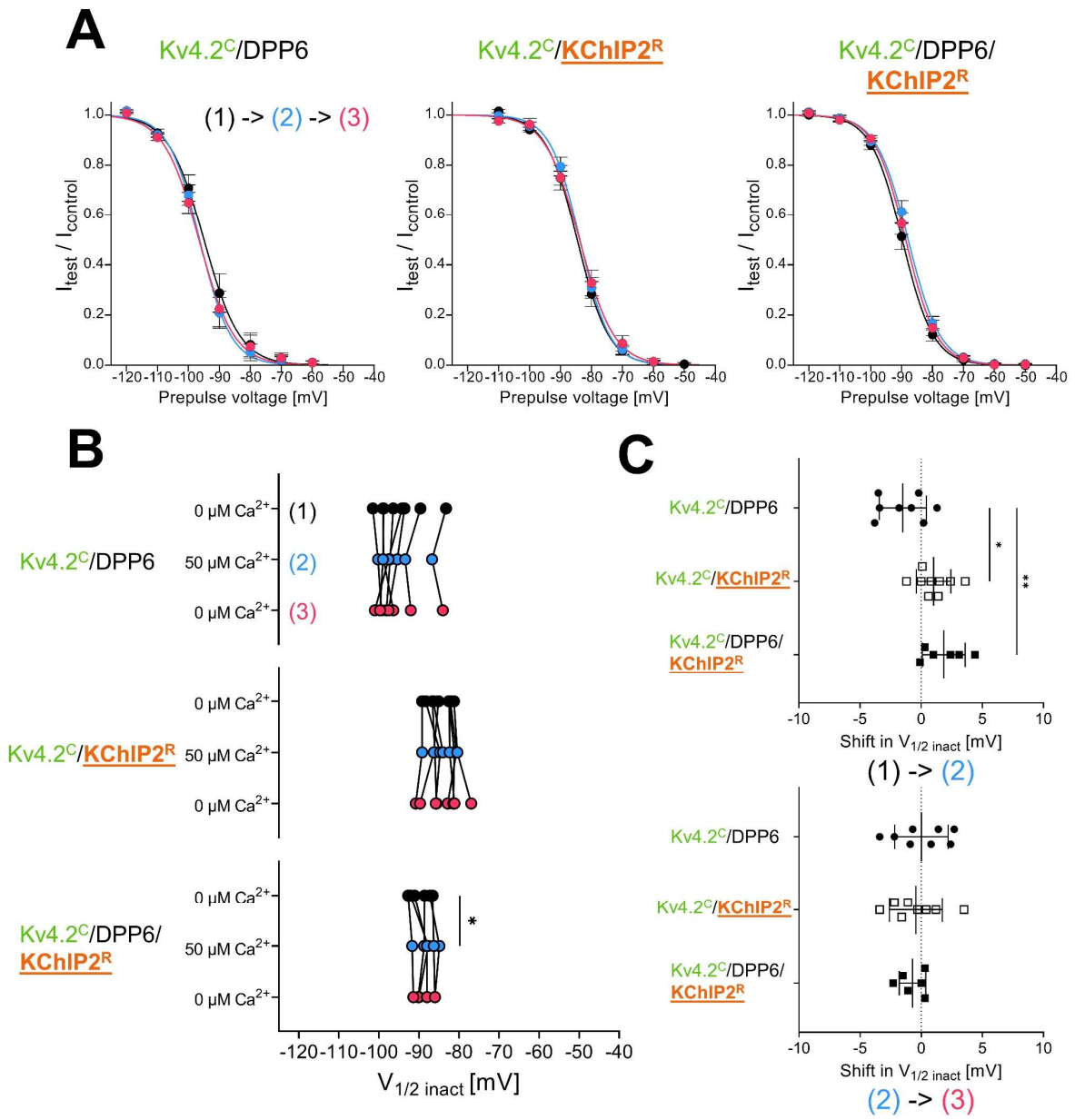

Figure 4.25: **Effects of 50 µM internal Ca^{2+} on the voltage dependence of steady-state inactivation on Kv4.2^{C} channel complexes studied in HEK293T inside-out patches.**
(**A**) Voltage dependence of steady-state inactivation in Ca^{2+}-free solution (black, red) and 50 µM Ca^{2+}. (**B**) Data were analyzed using a single Boltzmann fit and individual $V_{1/2\ inact}$ values are shown in triplets. Triplets were analyzed using repeated measures ANOVA (or mixed effects analysis, when values are missing) followed by Tukey post hoc test. (**C**) Shift $V_{1/2\ inact}$ due to application or withdrawal of 50 µM Ca^{2+}. Groups were analyzed using one-way ANOVA followed by a Tukey post hoc test. *p<0.05, **p<0.01

Table 4.8: **Electrophysiological properties and effects of 50 µM internal Ca^{2+} in $Kv4.2^C$ channel complexes studied in HEK293T cells inside-out patches.**
Number of experiments may vary due to patch breakage. If not otherwise stated number count is displayed at the top of the column of values.
* indicate for significant Ca^{2+}-related effect,
# indicate for significant differences between both Ca^{2+}-free solution recordings (1) and (3),
T indicate for significant differences between $Kv4.2^C$/$KChIP2^R$ and $Kv4.2^C$/DPP6/$KChIP2^R$,
D indicate for significant differences between $Kv4.2^C$/DPP6 and $Kv4.2^C$/DPP6/KChIP2 or $Kv4.2^C$/DPP6/$KChIP3^R$.
All entries describe mean ± SD. One symbol : p<0.05, two symbols : p<0.01, three symbols : p<0.001, four symbols : p<0.0001.

	Tau1 [ms]	Rel. change Tau1	Tau2 [ms]	Rel. change Tau2	Tau_{Rec} [ms]	Rel. change Tau_{Rec}	$V_{1/2\ inact}$ [mV]	Shift in $V_{1/2\ inact}$ [mV]
$Kv4.2^C$/DPP6	(n = 11)				(n = 9)		(n = 8)	
(1) 0 µM Ca^{2+}	8.2 ± 1.8		422 ± 177		103 ± 20		-94.4 ± 5.9	
(2) 50 µM Ca^{2+}	8.9 ± 2.7	1.08 ± 0.12	331 ± 130 *	0.83 ± 0.17	114 ± 22	1.11 ± 0.11	-95.9 ± 4.3	-1.5 ± 1.9
(3) 0 µM Ca^{2+}	8.8 ± 2.4	1.00 ± 0.10	330 ± 143 #	1.09 ± 0.39	112 ± 30 (n = 8)	0.99 ± 0.14	-95.9 ± 5.6	0.0 ± 2.2
$Kv4.2^C$/$KChIP2^R$	(n = 12)				(n = 7)		(n = 9)	
(1) 0 µM Ca^{2+}	18.3 ± 8.0		89 ± 42		85.0 ± 39.3		-84.8 ± 2.9	
(2) 50 µM Ca^{2+}	16.8 ± 4.9	0.98 ± 0.18	112 ± 51	1.33 ± 0.44 D	83.6 ± 29.7	1.06 ± 0.28	-83.7 ± 3	1.0 ± 1.4 D
(3) 0 µM Ca^{2+}	15.5 ± 4.1	0.94 ± 0.13	97 ± 21	0.96 ± 0.28	84.9 ± 28.1	1.03 ± 0.09	-84.2 ± 4.6 (n = 8)	-0.4 ± 2.2
$Kv4.2^C$/DPP6/ $KChIP2^R$	(n = 12)				(n = 7)		(n = 6)	
(1) 0 µM Ca^{2+}	27.1 ± 8.9		165 ± 56		37.7 ± 24.2		-89.7 ± 2.6	
(2) 50 µM Ca^{2+}	26.1 ± 9.6	0.95 ± 0.11	201 ± 55	1.33 ± 0.53 D	45.5 ± 24.9	1.08 ± 0.26	-87.9 ± 2.3 *	1.6 ± 1.8 DD
(3) 0 µM Ca^{2+}	27.4 ± 10.4	1.04 ± 0.08	226 ± 90 #	1.13 ± 0.28	49.5 ± 24.0 ## (n = 6)	1.05 ± 0.08	-88.6 ± 2.3	-0.7 ± 1.1

4.5 Expression and subcellular localization of Kv4.2^{C} and KChIP2^{R} or KChIP3^{R} in HEK293T cells

Lastly, possible effects of Ca^{2+} on the subcellular localization and possible trafficking of Kv4.2 channel complexes were studied. Epitope-tagged Kv4.2 channel complexes were used and imaged. After transient transfection, HEK293T cells were incubated in culture medium with the addition of 30 µM BAPTA-AM.

Transfection of Kv4.2^{C} in HEK293T cells resulted in the visible expression of Kv4.2^{C} channel constructs. However, Kv4.2^{C} expression alone resulted in clustered expression in the cytosolic region with little to no visible membrane expression. Treatment with 30 µM BAPTA did not show any observable differences compared to untreated groups. Co-expression with DPP6 showed a less clustered appearance with a uniform distribution along the plasma membrane. Treatment with 30 µM BAPTA-AM did not show any notable differences (Figure 4.26). Co-expression with KChIP2^{R} also resulted in a strong association with the plasma membrane, with Kv4.2^{C} clusters in the cytosol mostly abolished. KChIP2^{R} was observed to be evenly expressed inside the cytosol in some cases. Treatment with 30 µM BAPTA-AM did not show any significant differences (Figure 4.27). Co-expression as a ternary complex Kv4.2^{C}/DPP6/KChIP2^{R} showed similar results as the binary complex Kv4.2^{C}/KChIP2^{R} (Figure 4.28). Overall, the morphology and membrane association were similar in every studied case, with some variability in the expression of KChIP2^{R} observed among the cells.

Co-expression of Kv4.2^{C} with KChIP3^{R} showed similar characteristics in terms of morphology and membrane association. No notable differences were observed in the microscopy images. However, when KChIP3^{R} transfected cells were cultivated in 30 µM BAPTA-AM, a significant amount of cell death was observed, and very few cells remained for imaging.

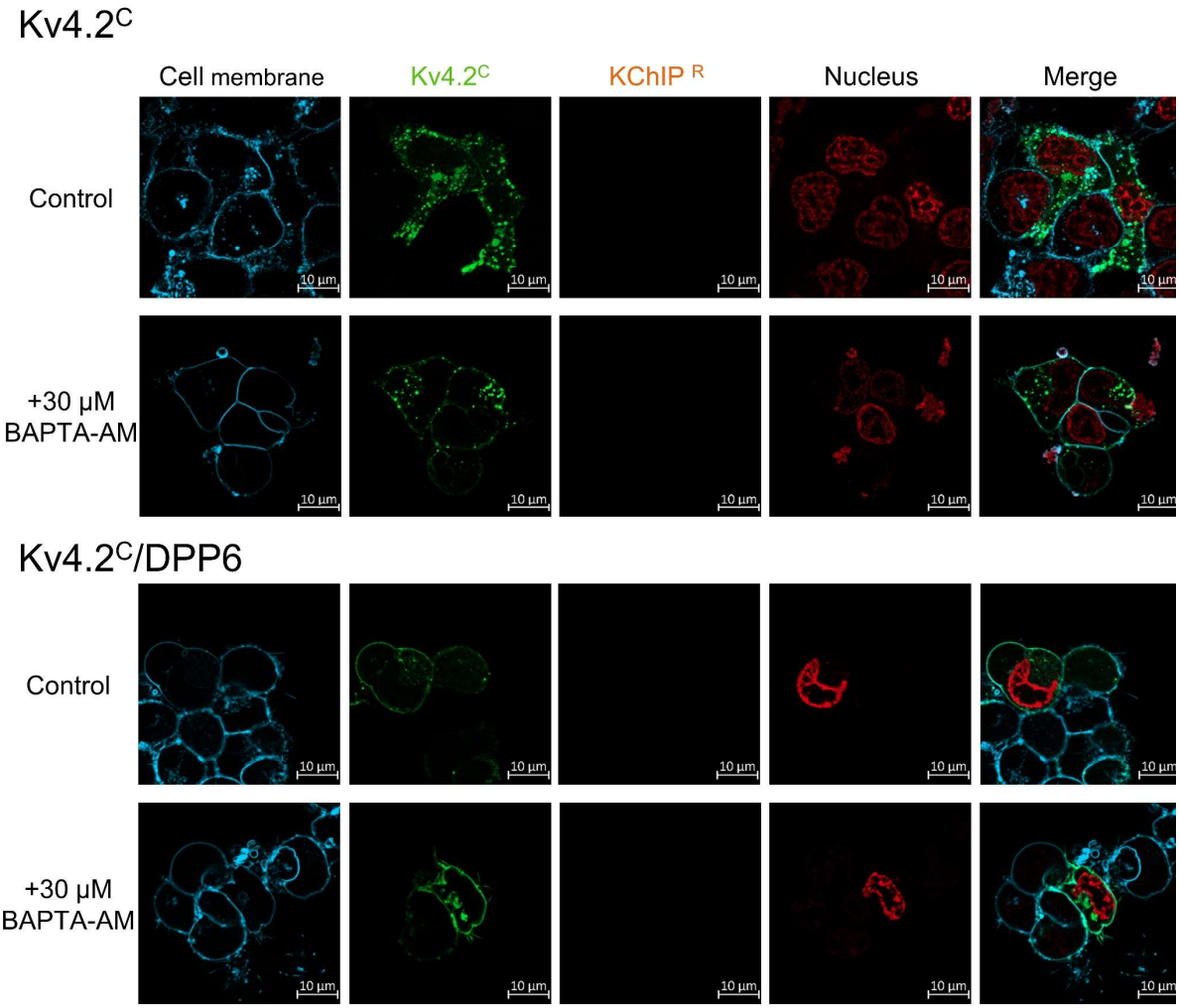

Figure 4.26: **Localization of Kv4.2^{C} studied in HEK293T cells.**
Representative cells were selected to show distribution of Kv4.2^{C} when expressed without auxiliary subunits and co-expression with DPP6.

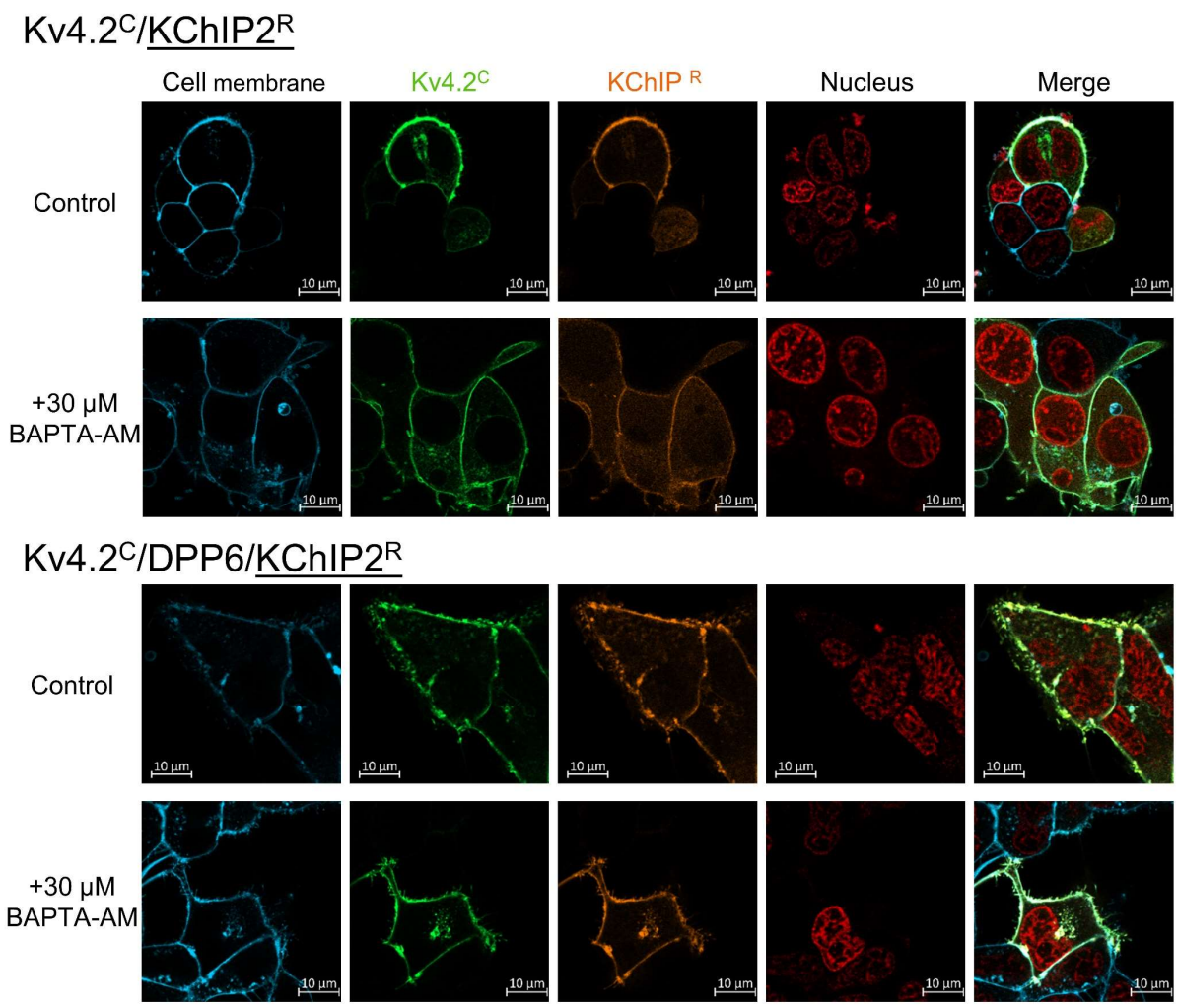

Figure 4.27: **Localization of Kv4.2^{C} co-expressed with KChIP2^{R} studied in HEK293T cells.** Representative cells were selected to show distribution of Kv4.2^{C} when co-expressed with KChIP2^{R} as binary complex and together with DPP6 as ternary complex.

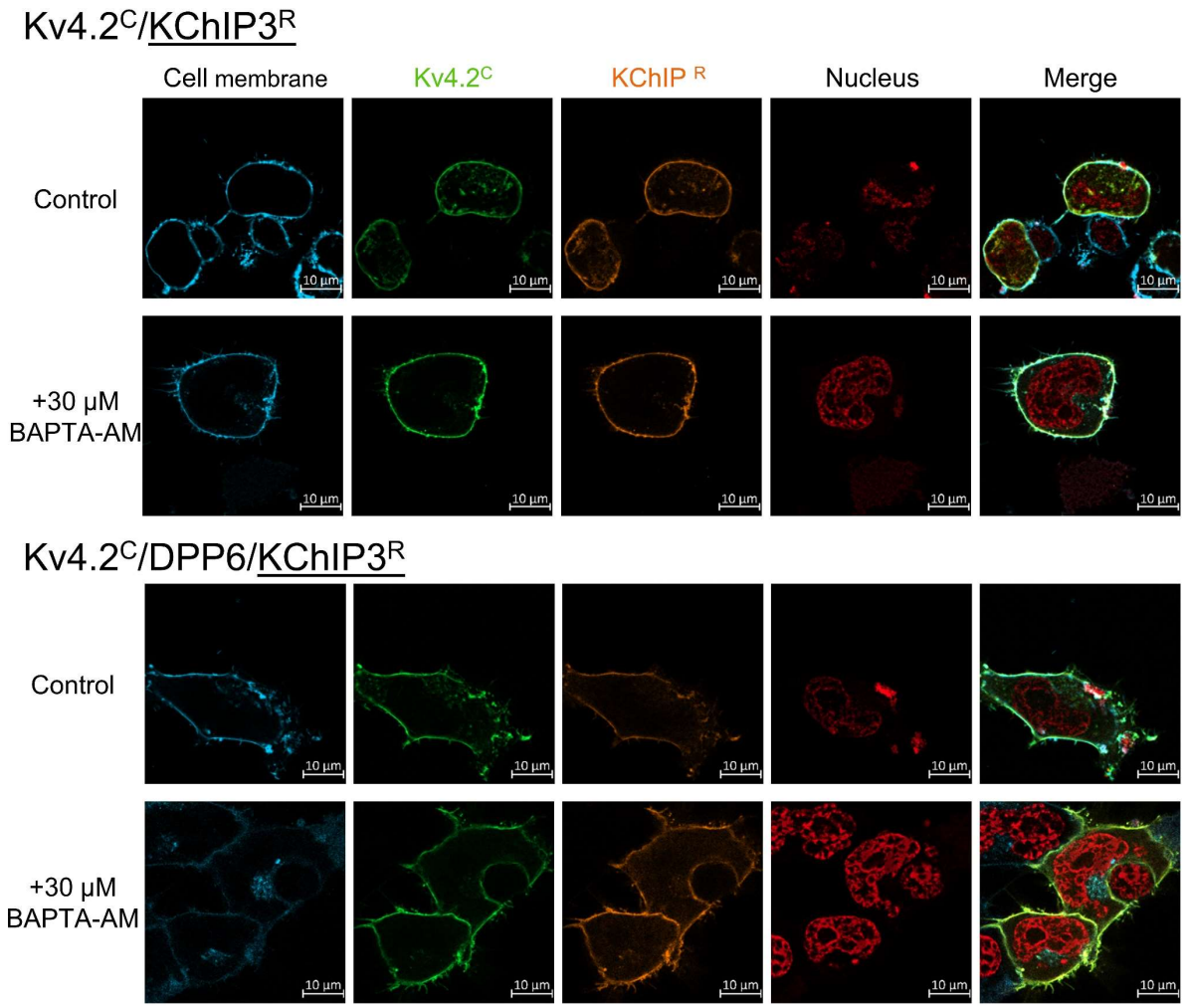

Figure 4.28: **Localization of Kv4.2^{C} co-expressed with KChIP3^{R} studied in HEK293T cells.** Representative cells were selected to show distribution of Kv4.2^{C} when co-expressed with KChIP3^{R} as binary complex and together with DPP6 as ternary complex.

5. Discussion

5.1 Modulation of Kv4 channel complexes by varying internal Ca^{2+}

The present study demonstrated a different approach to study the acute modulation of Kv4.2 channel complexes by varying internal Ca^{2+} through direct application to inside-out patches. In addition, the effects of patch excision were studied for $Kv4.2^{C}$ channel complexes.

Beck and Covarrubias previously studied the effects of patch excision and patch-cramming on Kv4.1 and Kv4.3 channels in *Xenopus* oocytes[52]. Patch excision in a Ca^{2+}-free environment led to a time-dependent acceleration of macroscopic inactivation and a reduction in the peak amplitude. Patch-cramming in the *Xenopus* oocyte partially reversed the observed effects. Furthermore, they reported a negative shift in the voltage dependence of inactivation and minimal changes in the recovery from inactivation at hyperpolarized voltages. These authors suggested a modulation of the closed-state inactivation of Kv4 channels and a potential influence of modulatory cytoplasmic factors[52]. Similar to the study by Beck and Covarrubias, patch excision in HEK293T cells expressing $Kv4.2^{C}$ channels together with auxiliary subunits led to an acceleration of macroscopic inactivation with the modest effects observed in $Kv4.2^{C}$/DPP6/$KChIP2^{R}$ channel complexes. Furthermore, a negative shift in the voltage dependence of steady-state inactivation was observed, but unlike in the study of Beck and Covarrubias, a slowing in the recovery from inactivation was also observed. In the presence of KChIP, either as a binary or ternary complex, the observed effects were bolder.

Modulation of Kv4 channel complexes through varying cytoplasmic Ca^{2+} has been studied before. Wang and coworkers[41] used patch-pipette solutions with different Ca^{2+} concentrations and recorded, in whole cell configuration, I_{SA} currents from cultured rat cerebellar granule cells, where KChIP1, 3, and 4 are highly expressed [53]. These authors report a nearly 2-fold increase in the peak current amplitude in high Ca^{2+}, a slowing in the macroscopic inactivation, and a negative shift in the voltage dependence of inactivation, but no significant effects on the recovery from inactivation[41]. Groen and Bähring[54] studied the modulation of Kv4.2/KChIP2 channel complexes in HEK293 cells by using different patch-pipette solutions in whole cell configuration. These authors reported a slowing in the recovery from inactivation with increasing Ca^{2+} compared to nominal Ca^{2+}-free recordings with BAPTA in the patch-pipette solution. In addition, this

study used EF-hand mutants of KChIP2c to study the effect of cytoplasmic Ca^{2+} on the recovery from inactivation. For Kv4.3/KChIP2ΔEF3 channel complexes, the recovery from inactivation was accelerated in 50 µM Ca^{2+} and showed an inversion of the observed effect in wild type constructs. Furthermore, these authors studied the effect using a CaMKII inhibitor. The presence of the CaMKII inhibitor KN-93 together with high Ca^{2+} (50 µM Ca^{2+}) showed an acceleration of the recovery from inactivation, again an inversion of the previous observed effect without a CaMKII inhibitor[54]. These results showed the differential effects on the modulation of Kv4.2/KChIP2 channel complexes in high Ca^{2+} and the potential involvement of other cellular components such as CaMKII. Murphy and Hoffmann[55] studied Kv4 channel complexes with different KChIP families and splice variants in HEK293 cells using different patch-pipette solutions. Whole cell recordings in 10 µM Ca^{2+} pipette solution showed a decrease in Tau1 as well as an increase in current density for Kv4.2/KChIP2c channel complexes, while the voltage dependence of steady-state inactivation and the recovery from inactivation remained unaffected. For Kv4.2/KChIP2 channel complexes, an increase in the current density but no differences in the biophysical properties were observed in 10 µM Ca^{2+}. For Kv4.2/KChIP3 channel complexes, a slight, but significant, negative shift in the voltage dependence of inactivation was observed, but no differences in the recovery from inactivation or macroscopic inactivation were observed in 10 µM Ca^{2+} [55]. These results showed the divergent Ca^{2+} regulation of Kv4 channels mediated by different KChIP families and their splice variants.

In the present study, the internal application of 10 µM Ca^{2+} on inside-out patches of HEK293T cells expressing $Kv4.2^{C}$ channel complexes led to a decrease in Tau1 in the presence of either KChIP2 or KChIP3. Furthermore, a slowing in the recovery from inactivation was observed in $Kv4.2^{C}$/DPP6/$KChIP2^{R}$ channel complexes. For $Kv4.2^{C}$/DPP6/$KChIP3^{R}$ channel complexes, the recovery from inactivation remained unaffected in 10 µM Ca^{2+}. This demonstrated the divergent effects of 10 µM internal Ca^{2+} on the Kv4.2 channel complex between the KChIP families. A slight negative shift in the voltage dependence of steady-state inactivation was observed for $Kv4.2^{C}$/DPP6/$KChIP3^{R}$ channel complexes in 10 µM Ca^{2+}, which is consistent with the reported results from Murphy and Hoffmann[55].

A limitation of the present study is the potential dissociation and loss of KChIP during patch excision and perfusion. In the presence of KChIP, patch excision resulted in a pronounced effect on the recovery from inactivation and the voltage dependence of

steady-state inactivation. This could suggest a disruption of the 4:4:4 stoichiometry over longer periods of recording and the possibility of introducing artificial effects. To address this, epitope-tagged proteins were intended to be used in patch-clamp fluorometry. The present study examined the FRET efficiencies between epitope-tagged Kv4.2/KChIP2 channel complexes with different linker lengths and yielded a slightly higher FRET efficiency than the previously reported "high FRET efficiency" of 11.22% in Kv4.2-YFP/KChIP3-CFP channel complexes[56]. $Kv4.2^{C}$ and $KChIP^{R}$ constructs can be utilized in future studies involving patch clamp fluorometry. However, the reported FRET efficiency should be interpreted with caution due to the strong photochromic behavior of mRuby3, which could potentially lead to a misinterpretation of FRET behavior[57]. It would be advised to exchange the mRuby3 fluorophore to another red fluorophore like e.g. mScarlet. This could potentially even increase the current FRET efficiency without changes to the filter cube setup. McCullock and co-workers reported a significant increase in the FRET efficiency using mScarlet-I compared to mRuby3[58]. Lastly, it should be noted that epitope-tagging of KChIP could potentially interfere with the KChIP/Ca^{2+} effects, but it seems unlikely.

5.2 The involvement of CaV channels in the Kv4 channel complex

The previously discussed studies utilized patch-pipette solutions to manipulate the Ca^{2+} in the entire cytoplasm, but physiologically relevant increases in Ca^{2+} could be spatially restricted in the cytoplasm. In a study by Anderson and coworkers[43], T-type calcium channels (CaV3) were identified as a physiological source of Ca^{2+}. The authors initially observed, in cerebral stellate cells, a negative shift around -10 mV in the voltage dependence of steady-state inactivation in the I_{SA} with the application of mibefradil. Application of the specific R-type calcium channel inhibitor SNX-482 resulted in no alterations in the properties of I_{SA}, suggesting the involvement of CaV3 channels in the regulation of I_{SA}. The co-immunoprecipitation experiments suggested the formation of Kv4.2, KChIP3, and CaV3 as a macromolecular signaling complex. Heterologous expression of these components in tsA-201 cells together with DPP10 reproduced a similar shift in the voltage dependence of steady-state inactivation. This mibefradil-induced shift in $V_{1/2\ inact}$ was exclusively observed in the presence of KChIP3 and CaV3 channels. The presence of other KChIP members (KChIP1, KChIP2, and KChIP4) or other CaV channels (CaV1.4, CaV2.1, and CaV2.3 with their respective pharmacological blocking) did not result in any significant alteration in the $V_{1/2\ inact}$ [43,59].

These results suggested the formation of a macromolecular signaling complex containing the CaV3 channels as a physiological Ca^{2+} source and KChIP3 as a potential Ca^{2+} sensor and modulator of Kv4 channels in a functional nanodomain (<50 nm)[43,59,60]. Murphy and colleagues[56] studied the involvement of R-type calcium channels (CaV2.3) in Kv4 channel complexes. These authors utilized co-immunoprecipitation as well as FRET to test Kv4.2 and CaV2.3 interactions. Their results suggested that CaV2.3 and Kv4.2 bind together and form a complex in a nanodomain (<10 nm) and, furthermore, can form without Kv4 auxiliary subunits. Heterologous expression of Kv4.2/KChIP2c/CaV2.3 in HEK293-FT cells resulted in an increased current density compared to Kv4.2/KChIP2c channel complexes without alterations in the recovery from inactivation or the voltage dependence of steady-state inactivation. These authors further tested if local CaV2.3 Ca^{2+} influx led to the increase of the current density. They used patch-pipettes containing the fast-acting Ca^{2+} chelator BAPTA and indeed observed a reversal of the effect[56]. Even though these authors did not fully test for significance, it is noteworthy to examine the effects of CaV2.3 co-expression on Kv4.2 channel complexes. Co-expression of CaV2.3 together with Kv4.2/KChIP2c showed a slight positive shift in $V_{1/2\ inact}$ [56]. Similar to the present study, the internal application of 50 µM Ca^{2+} on $Kv4.2^{C}$/DPP6/$KChIP2^{R}$ channel complexes led to a positive shift in $V_{1/2\ inact}$, while this positive shift remained absent with the internal application of 10 µM Ca^{2+}.
Interestingly, Murphy and coworkers did recordings with BAPTA in the patch-pipettes of either Kv4.2/KChIP2c/CaV2.3 or Kv4.2/DPP6/KChIP2c/CaV2.3 channel complexes, and their results showed a strong positive shift around +8 mV in $V_{1/2\ inact}$ [56].

Concluding so far, the involvement of CaV channels in Kv4 channel complexes seems to greatly enhance the modulation of Kv4/KChIP channel complexes. Previous studies using 10-50 µM Ca^{2+} in the patch-pipettes or the internal application of 10 µM or 50 µM Ca^{2+} in the present study showed surprisingly subtle effects on Kv4 channel complexes. The formation of a nanodomain (<10 nm) containing Kv4.2 with auxiliary subunits together with CaV channels, as a signaling complex, raised the question whether the used Ca^{2+} concentration might be too low and whether internal Ca^{2+} concentrations could reach several hundred µM in a temporal-spatial manner[61,62]. In addition, could other intracellular components predominantly regulate Kv4 channels in a KChIP and Ca^{2+}-dependent manner.

The results from the present study and the findings from the mentioned studies are summarized and simplified in Table5.1 and Table 5.2.

Table 5.1: Overview of reported effects of internal Ca^{2+} on Kv4 channel complexes with the focus on KChIP3 co-expression. Arrows indicate an increase (↑) or decrease (↓) in time constants value and negative (←) or positive (→) shift in the voltage dependence of inactivation.

Group	Expression system	Ca2+ source	Application/ Depletion of Ca2+	Kv4 channel complex	Tau1	Tau2	Tau_{Rec}	$V_{1/2\ inact}$
Present study	*Xenopus* Inside Out	Perfusion	+10 µM Ca^{2+}	Kv4.2/DPP6/KChIP3			↑	←
	HEK293T Inside Out	Perfusion	+10 µM Ca^{2+}	$Kv4.2^{C}$/DPP6/$KChIP3^{R}$	↓			
Murphy 2019	HEK293-T Whole cell	Pipette	+ 10 µM Ca^{2+}	Kv4.2/KChIP3				←
Wang 2005	Rat cerebellar granule neurons Whole cell	Pipette	+ 2 mM Ca^{2+}	Endogenous expression	↑	↑		←
Present study	*Xenopus* Inside Out	Perfusion (10 µM Ca^{2+})	HEDTA/EGTA	Kv4.2/DPP6/KChIP3	↓	↓		
	HEK293T Inside Out	Perfusion (10 µM Ca^{2+})	EGTA	$Kv4.2^{C}$/DPP6/$KChIP3^{R}$				
Anderson 2010	Stellate cells Whole cell	CaV	Mibefradil (-Ca^{2+})	Endogenous expression				←
	HEK293T Whole cell	CaV3.3	Mibefradil (-Ca^{2+})	Kv4.2/KChIP3				←
			Mibefradil (-Ca^{2+})	Kv4.2/DPP10c/KChIP3				←

Table 5.2: Overview of reported effects of internal Ca^{2+} on Kv4 channel complexes with the focus on co-expression together with KChIP2 and other members of the KChIP families and its splice variants. Arrows indicate an increase (↑) or decrease (↓) in time constants value and negative (←) or positive (→) shift in the voltage dependence of inactivation. Double arrows indicate increased effect in response to higher internal Ca^{2+} concentrations. There were no statistics made for the biophysical parameters of Kv4.2 channel complexes in the study, indicated by the asterisk.

Group	Expression system	Ca^{2+} source	Application/ Depletion of Ca2+	Kv4 channel complex	Tau1	Tau2	Tau_{Rec}	$V_{1/2\ inact}$
Present study	*Xenopus* Inside Out	Perfusion	+10 µM Ca^{2+}	Kv4.2/DPP6/KChIP2			↑	←
		Perfusion	+10 µM Ca^{2+}	$Kv4.2^{C}$/$KChIP2^{R}$	↓			
	HEK293T Inside Out	Perfusion	+50 µM Ca^{2+}	$Kv4.2^{C}$/$KChIP2^{R}$				
		Perfusion	+10 µM Ca^{2+}	$Kv4.2^{C}$/DPP6/$KChIP2^{R}$	↓		↑	
		Perfusion	+50 µM Ca^{2+}	$Kv4.2^{C}$/DPP6/$KChIP2^{R}$				→
Groen 2017	HEK293 Whole cell	Pipette	+10 µM Ca^{2+}	Kv4.3/KChIP2			↑	
			+50 µM Ca^{2+}	Kv4.3/KChIP2			↑↑	
Murphy* 2022	HEK293-FT Whole cell	CaV2.3	+ Ca^{2+}	Kv4.2/KChIP2c		↓		→
Murphy 2019	HEK293-T Whole cell	Pipette	+ 10 µM Ca^{2+}	Kv4.2/KChIP2				
				Kv4.2/KChIP2c				
				Kv4.2/DPP6/KChIP2c				
				Kv4.1/KChIP2c				
				Kv4.3/KChIP2c				
				Kv4.2/KChIP2a1				
				Kv4.2/KChIP2a	↓			
				Kv4.2/KChIP1a				
				Kv4.2/KChIP1b			↓	→
				Kv4.2/KChIP4bL				
				Kv4.2/KChIP4a				
Present study	*Xenopus* Inside Out	perfusion (10 µM Ca^{2+})	HEDTA/EGTA (-Ca^{2+})	Kv4.2/DPP6/KChIP2	↓	↓		
	HEK293T Inside Out	perfusion (10 µM Ca^{2+})	EGTA (-Ca^{2+})	$Kv4.2^{C}$/$KChIP2^{R}$			↑	
		perfusion (50 µM Ca^{2+})	EGTA (-Ca^{2+})	$Kv4.2^{C}$/$KChIP2^{R}$				
		perfusion (10 µM Ca^{2+})	EGTA (-Ca^{2+})	$Kv4.2^{C}$/DPP6/$KChIP2^{R}$				
		perfusion (50 µM Ca^{2+})	EGTA (-Ca^{2+})	$Kv4.2^{C}$/DPP6/$KChIP2^{R}$				
Murphy* 2022	HEK293-FT Whole cell	CaV2.3	BAPTA (-Ca^{2+})	Kv4.2/KChIP2c		↓		→
		CaV2.3	BAPTA (-Ca^{2+})	Kv4.2/DPP6/KChIP2c				→
Andrson 2010	HEK293T Whole cell	CaV3.3	Mibefradil (-Ca^{2+})	Kv4.2/DPP10c/KChIP2				

5.3 The many roles of KChIP

So far, the present study has focused mainly on the modulatory role of KChIP on Kv4 channels, but the functionality of KChIPs goes far beyond Kv4 modulation. Four KChIP genes have been identified, along with several splice variants, and have been found to be broadly expressed across diverse tissues and brain regions. These alternative splice variants primarily exhibit variation in the N-terminal region, and each variant demonstrates distinct mechanisms of action[26,55]. Ongoing research is actively exploring the complex interactions between KChIP and various proteins and ion channels. Studies have demonstrated that KChIP proteins can act as Ca^{2+} sensors for protein complexes unrelated to Kv4 channels. Among the four KChIP members, KChIP3 stands out as the most prominent family member. Ramachadan and coworkers[63] identified several interaction partners of KChIP3 in a Ca^{2+}-dependent and independent manner using affinity capture and mass spectrometry. Furthermore, these authors reported the heterodimerization of KChIP3 and Calmodulin in a Ca^{2+}-dependent manner, and their results showed that KChIP3/Calmodulin regulate Calcineurin activity[63]. Calcineurin is a serine-threonine-specific protein phosphatase and participates in diverse cellular processes. One of them is the regulation of Kv4 channel expression through the Calcineurin/NFAT signaling pathway[64,65]. These findings could indicate an indirect role for KChIP3 as a Ca^{2+} sensor for the regulation of Kv4 channel expression.

KChIP3 also interacts in a Ca^{2+}-dependent way with both presenilin 1 & 2 (PS1 & PS2), which are part of the gamma-secretase complex that mediates the gamma-cleavage of amyloid precursor proteins, and studies have shown that overexpression of KChIP3 increased gamma-secretase activity[66,67]. Furthermore, KChIP3/PS complexes play a role in intracellular Ca^{2+} signaling itself via Inositol-1, 4, 5-trisphosphate (IP3) and ryanodine receptors in the ER and regulates Ca^{2+} release. KChIP3 reversed the potentiation of Ca^{2+} signaling mediated by PS1 as well as slowed the decay rate of Ca^{2+} signaling. Dysregulation of both gamma secretase and ER Ca^{2+} release systems are linked to Alzheimer's disease[27,68,69].

KChIP3 also participates in the regulation of NMDA receptors. Wu and coworkers studied the function of KChIP3 in synaptic transmission and utilized transgenic mice overexpressing a Ca^{2+}-insensitive KChIP3 mutant. These authors reported in a reduction NMDA receptor-mediated current in transgenic mice. These authors additionally identified the scaffolding postsynaptic protein PSD-95 as an interaction

partner for KChIP3 and suggested KChIP3 contributes to a reduction in NMDA receptor-mediated response through the interaction of scaffolding postsynaptic protein PSD-95[70]. In a study done by Zhang and coworkers[32], they identified a direct Ca^{2+}-dependent interaction between KChIP3 and NR1, a subunit of the NMDA receptor. These authors suggested that this interaction reduces NMDA current and may play a neuroprotective role in excitotoxicity by negatively regulating KChIP3/NR1 on NMDA receptors[32].

KChIP2, another member of the KChIP family, has been discovered to directly modulate Ca^{2+} signaling. Studies have shown a direct interaction and modulation of L-type calcium current ($I_{Ca,L}$) by KChIP2 through the N-terminal domain of CaV1.2 channels in a Ca^{2+}-independent manner. KChIP2-deficient mice myocytes resulted in a reduced $I_{Ca,L}$ without affecting the voltage dependence of activation or inactivation[31]. In a separate study by Nassal and coworkers[30], the knockdown of KChIP2 in guinea pig ventricular myocytes led to a decrease in the amplitude and the broadening of Ca^{2+} transients, resulting in a reduced Ca^{2+} release and impaired myocyte contractility. These authors demonstrated that the reduced activity of ryanodine receptors was attributed to the relocalization of presenilin[30].

Ongoing studies continue to uncover the diverse roles of KChIPs, both in a Ca^{2+}-dependent and Ca^{2+}-independent manner. This diversity in KChIP functionality raises the question of whether such a specific acute modulation of Kv4 channels through KChIP can exist. Can KChIPs directly interact and modulate Kv4 channels in a Ca^{2+}-dependent manner, or could KChIPs act more as a Ca^{2+} sensor and a mediator between Kv4 channels and other internal cellular elements?

5.4 The diversity in the regulation of Kv4 channels

The regulation of Kv4 channels has been shown to be very diverse. KChIPs are able to bind to Kv4 channels in a Ca^{2+}-independent manner[27,71] and similar to the results presented here; Ca^{2+} does not seem to be needed for membrane expression. Incubation in a 30 µM BAPTA-AM solution post-transfection showed no alteration in membrane expression. Intriguingly, despite high membrane expression of $Kv4.2^{C}$/$KChIP3^{R}$, cell-attached and inside-out recordings resulted in very low to no notable current <20 pA (data not shown). In a recent study by Li and coworkers[72], the authors suggested that phosphorylation of Ser552 disrupts Kv4.2 and KChIP2 interactions, leading to dissociation of Kv4.2 from lipid rafts and therefore internalization. Furthermore, mutation of Ser552 to aspartate, which resembles a pseudo-phosphorylated state, resulted in a reduced current density in HEK293T cells[72]. Could specific phosphorylation status also be critical for Kv4/KChIP3 interaction and additionally important for proper channel function? Furthermore, could Kv4 phosphorylation play a role in Ca^{2+}-mediated KChIP modulation on Kv4 channel complexes? Phosphorylation of Kv4 channels has gained more attention, and ongoing studies provide more insights into how phosphorylation status changes the interaction between proteins and may interfere with KChIP functionality. The phosphorylation of Ser552 has gained significant attention due to its observed phosphorylated state in the rat hippocampus *in situ*[73]. Studies indicated that co-expression with DPP or KChIP leads to enhanced phosphorylation of Kv4 channels, suggesting a potential role in membrane trafficking[74,75]. Hammond and coworkers[76] demonstrated that phosphorylation at Ser552 resulted in a decrease in current amplitude and internalization of Kv4.2 channels. These studies showed a correlation between membrane expression and the phosphorylation status of Ser552, but not being a determent for trafficking[74–76]. Nestor and colleagues[77] reported that it may have an essential role in the somato-dendritic gradient distribution of Kv4.2 channels in Ca1 hippocampal neurons[77]. Taken together, Ser552 seems to take an important role in the internalization and localization of Kv4.2 channels.

Modulation via the ERK/MAPK pathway could also influence channel properties. Schrader and coworkers[78] studied the functional effects of Kv4.2 phosphorylation at Thr602, Thr607, and S616 in *Xenopus* oocytes using site-directed mutants. Their results demonstrated that Thr607 phosphorylation influences the voltage dependence of activation as well as the recovery from inactivation. This study additionally showed

how KChIP interaction might be necessary for functional effects of ERK phosphorylation to Kv4 channel properties. Co-expression of wild type or phosphorylation-resistant mutation Thr607Ala Kv4.2 and KChIP3 showed a negative shift in the voltage dependence of activation. Co-expression of pseudo-phosphorylated Thr607Asp Kv4.2 and KChIp3 showed no significant alterations in the voltage dependence of activation[78]. These results demonstrated the modulating effects of phosphorylation on the Kv4.2 channel. Hu and coworkers[79,80] observed a co-localization of p38 MAPK with Kv4.2 channels. Activation of p38 MAPK with kainat led to an increased phosphorylation of Thr607 and Thr602 in Kv4.2 channels and a reduction in excitability of hippocampal neurons. These authors suggested that these phosphorylation sites contribute to binding with peptidyl-prolyl cis-trans isomerase NIMA-interacting 1 (Pin1), which modulates Kv4 channel conformation and furthermore promotes the dissociation from DPP6, regulating neuronal excitability[79,80].

Phosphorylations by CaMKII also seem to play an important role in Kv4 regulation.
Groen and Bähring[54] studied the influence of CaMKII on the regulation of Kv4.3/KChIP2 channel complexes in HEK293 cells by using different patch-pipette solutions in whole cell configuration. These authors first reported a slower recovery from inactivation when recorded in 50 µM Ca^{2+} compared to nominal Ca^{2+}-free recordings in BAPTA. The addition of the CaMKII inhibitor KN-93 turned the observed effect around. The authors observed an accelerated recovery from inactivation when recorded in 50 µM Ca^{2+} together with KN-93 compared to nominal Ca^{2+}-free recordings in BAPTA + KN-93. Furthermore, the authors studied three potential phosphorylation sites of CaMKII in Kv4.3 channels. Mutations of Thr53, Ser516, and Ser550 in the Kv4.3 short splice variant to either alanine or aspartate showed no alterations in the recovery from inactivation, recorded either in BAPTA or in 50 µM Ca^{2+}. Previously discussed phosphorylation at Ser552 (Ser550 for Kv4.3 short splice variant) seemed to be important in membrane expression but could the other phosphorylation sites be important for regulation in the Kv4 channel kinetics and interfere with KChIP interaction?
Kim et al[81] reported that CaMKII phosphorylation in Kv4.1 at Ser555 (Ser552 for Kv4.2) regulated channel activity by decreasing current density without changes in macroscopic current inactivation. These authors showed that this specific site could also be susceptible to CaMKII phosphorylation in addition to previously found PKA

phosphorylation. Contradictorily, inhibition of CaMKII by KN-93 resulted in a decrease in current density. This effect is also present, although not significant, in Kv4.1 Ser555Ala[81]. In a previous study by Varga and coworkers[82], the authors reported that Ser438 and Ser459 play a major role in channel expression. Kv4.2 co-expressed with KChIP3 and a constitutively active CaMKII increased total protein expression levels in COS-7 cells as well as increased current density. Pseudophosphorylation by mutating these sites to aspartate resulted in elevated expression, while mutation to alanine decreased total expression. This study claimed no relevant changes in Kv4 channel properties, but only a small number of experiments were conducted[82]. Studies done with the Kv4.3 short splice variant expressed alone in HEK293 cells revealed a modulatory role for CaMKII phosphorylation. Recordings with constitutive active CaMKII in the patch-pipette showed similar effects as co-expression with KChIP. Kv4.3 currents slowed in macroscopic inactivation kinetics, increased recovery from inactivation, and showed a positive shift in the voltage dependence of inactivation. Inhibition of endogenously expressed CaMKII reversed the effects. The study showed that Ser550 (Ser552 for Kv4.2) is a key modulatory site and phosphorylation-resistant mutation to alanine abolished the modulatory effects of CaMKII[83]. In a later study by Colinas and coworkers[84], same effects were reported for Kv4.3 when CaMKII was inhibited. In addition, these authors reported no effects on Kv4.2 channels when CaMKII was inhibited. However, elevating intracellular Ca^{2+} concentration showed a slowing in macroscopic inactivation kinetics. Additional inhibition of CaMKII abolished observed effects. Recordings in isolated rat myocytes showed that inhibition of CaMKII did accelerate macroscopic inactivation, but recovery from inactivation was not affected[84]. Rat myocytes express KChIP2 and therefore could raise the question of whether KChIP could influence Kv4 modulations by CaMKII. Furthermore, these studies showed that CaMKII directly interacts with Kv4.3 and Kv4.2. Co-immunoprecipitation revealed that CaMKII and Kv4.3 form a complex, while Kv4.2 did not in HEK293 cells. However, in myocytes, Kv4.2 also formed a complex with CaMKII. In a later study by El-Haou and coworkers[85], the membrane-associated guanylate kinase SAP97 formed the link between Kv4 and CaMKII[84]. Co-expression of SAP97 with Kv4.3 and KChIP2 increased current density and slowed macroscopic inactivation kinetics without affecting voltage dependence of activation and inactivation or recovery from inactivation. Intriguingly, transfection of Kv4.3 in stable-expressing SAP97 HEK293 cells showed similar characteristic effects as it would with KChIP co-

expression. Furthermore, co-transfection of Kv4.3 with SAP97 silencing shRNA abolished the observed effect. Additionally, treatment with the CaMKII inhibitor AIP reduced the observed effect in the Kv4.3 group and no effect was observed in the Kv4.3 + SAP97 shRNA group. The same experiments were done with Kv4.2, which resulted only in an increase in current density but did not affect channel kinetics. However, additional elevation of intracellular Ca^{2+} resulted in a slowing of macroscopic inactivation, but other channel properties were not tested[85].

These results provide intriguing insights into how phosphorylation of Kv4 channels can alter channel properties and, furthermore, mimic similar effects as they would with KChIP co-expression.

6. Conclusion

The presented study provided first insights into the acute modulation of Kv4/KChIP channel complexes by internally applied Ca^{2+}. However, utilization of inside-out patches and internal application of Ca^{2+} resulted in minimal effects. In addition, findings were incoherent among the studied expression systems and internal Ca^{2+} concentrations. The results revealed the complex effects of internal Ca^{2+} on different channel complexes and raised many unanswered questions and areas for further exploration.

1) Examination of higher Ca^{2+} concentrations: The present study primarily used 10 and 50 µM internal Ca^{2+}. It would be intriguing to explore the effects of higher Ca^{2+} concentrations on the modulation of Kv4/KChIP chan nel complexes. Previous research suggests that internal Ca^{2+} concentrations could reach several hundred µM in a temporal-spatial manner if Kv4 channel complexes exist in a nanodomain together with voltage gated Ca^{2+} channels[61]. That raises the question of whether higher Ca^{2+} concentrations may have different effects on channel kinetics and recovery from inactivation.
2) Investigation of interactions between Kv4 and KChIP: With the provided preliminary results on the FRET efficiency in Kv4/KChIP channel complexes and the recommendation made relating to the acceptor fluorophore, the epitope-tagged constructs open the possibility to study conformational changes under varying internal Ca^{2+} concentrations. Furthermore, epitope-tagged constructs have the potential to be utilized in combining fluorometry and electrophysiology

to study conformational changes as well as the biophysical properties of Kv4/KChIP channel complexes.

3) Investigation of other intracellular components: While the present study focused on the acute modulatory effect of internal Ca^{2+} on Kv4 channel complexes in inside-out patches, there may be other intracellular components that could predominantly regulate Kv4 channels in a KChIP and Ca^{2+}-dependent manner. Exploring the roles of these components and their interactions with Kv4/KChIP channel complexes can provide a more comprehensive understanding of the regulatory mechanisms involved.
4) Exploration of Kv4 phosphorylation sites: Phosphorylation of Kv4 channels has been implicated in channel modulation and membrane trafficking. Investigating the specific phosphorylation sites of Kv4 channels could reveal regulatory and modulatory effects in the Kv4 channel as well as the interaction with the auxiliary subunits. Examining the interplay between Kv4 phosphorylation, KChIP, and Ca^{2+} effects could provide a more comprehensive understanding of the regulatory mechanisms involved.

By addressing these study objectives, we could obtain a better understanding of the modulation of Kv4/KChIP channel complexes by Ca^{2+} as well as the regulatory mechanisms underpinning these interactions. Furthermore, these insights could translate into a deeper understanding of neuronal excitability.

7. Literature

1. Wright, S. H. Generation of resting membrane potential. *Am. J. Physiol. - Adv. Physiol. Educ.* **28**, 139–142 (2004).
2. Hodgkin, A. & Huxley, A. A quantitative description of membrane current and its application to conductance and excitation. *J. Physiol.* **117**, 500–44 (1952).
3. Tanner, M. R. & Beeton, C. Differences in ion channel phenotype and function between humans and animal models. *Front. Biosci. - Landmark* **23**, 43–64 (2018).
4. Bean, B. P. The action potential in mammalian central neurons. *Nat. Rev. Neurosci.* **8**, 451–465 (2007).
5. Kuo, M. M. C., Haynes, W. J., Loukin, S. H., Kung, C. & Saimi, Y. Prokaryotic K+ channels: From crystal structures to diversity. *FEMS Microbiol. Rev.* **29**, 961–985 (2005).
6. Coetzee, W. A. *et al.* Molecular diversity of K+ channels. *Ann. N. Y. Acad. Sci.* **868**, 233–255 (1999).
7. Alexander, S. P. H. *et al.* The Concise Guide to Pharmacology 2019/20: Ion channels. *Br. J. Pharmacol.* **176**, S142–S228 (2019).
8. Yu, F. H. & Catterall, W. A. The VGL-chanome: a protein superfamily specialized for electrical signaling and ionic homeostasis. *Sci. STKE* **2004**, 1–18 (2004).
9. MacKinnon, R. Potassium channels. *FEBS Lett.* **555**, 62–65 (2003).
10. Alam, A. & Jiang, Y. Structural studies of ion selectivity in tetrameric cation channels. *J. Gen. Physiol.* **137**, 397–403 (2011).
11. Kuang, Q., Purhonen, P. & Hebert, H. Structure of potassium channels. *Cell. Mol. Life Sci.* **72**, 3677–3693 (2015).
12. Hibino, H. *et al.* Inwardly rectifying potassium channels: Their structure, function, and physiological roles. *Physiol. Rev.* **90**, 291–366 (2010).
13. Buckingham, S. D., Kidd, J. F., Law, R. J., Franks, C. J. & Sattelle, D. B. Structure and function of two-pore-domain K+ channels: Contributions from genetic model organisms. *Trends Pharmacol. Sci.* **26**, 361–367 (2005).
14. Enyedi, P. & Czirják, G. Molecular background of leak K+ currents: Two-pore domain potassium channels. *Physiol. Rev.* **90**, 559–605 (2010).
15. Kaczmarek, L. K. *et al.* International union of basic and clinical pharmacology. C. Nomenclature and properties of calcium-activated and sodium-activated potassium channels. *Pharmacol. Rev.* **69**, 1–11 (2017).
16. Grizel, A. V., Glukhov, G. S. & Sokolova, O. S. Mechanisms of activation of voltage-gated potassium channels. *Acta Naturae* **6**, 10–26 (2014).
17. Shen, N. V. & Pfaffinger, P. J. Molecular recognition and assembly sequences involved in the subfamily-specific assembly of voltage-gated K+ channel subunit proteins. *Neuron* **14**, 625–633 (1995).
18. Ludwig, J., Owen, D. & Pongs, O. Carboxy-terminal domain mediates assembly of the voltage-gated rat ether-a-go-go potassium channel. *EMBO J.* **16**, 6337–6345 (1997).
19. Salinas, M., Duprat, F., Heurteaux, C., Hugnot, J. P. & Lazdunski, M. New modulatory α subunits for mammalian Shab K+ channels. *J. Biol. Chem.* **272**, 24371–24379 (1997).
20. Matsumura, K., Yokogawa, M. & Osawa, M. *Peptide Toxins Targeting KV Channels BT - Pharmacology of Potassium Channels*. vol. 267 (Springer International Publishing, 2021).
21. Zhou, M., Morais-Cabral, J. H., Mann, S. & MacKinnon, R. Potassium channel receptor site for the inactivation gate and quaternary amine inhibitors. *Nature* **411**, 657–661 (2001).
22. Bähring, R. & Covarrubias, M. Mechanisms of closed-state inactivation in voltage-gated ion channels. *J. Physiol.* **589**, 461–479 (2011).
23. Bähring, R., Barghaan, J., Westermeier, R. & Wollberg, J. Voltage Sensor Inactivation in Potassium Channels. *Front. Pharmacol.* **3**, 1–8 (2012).
24. Ye, W. *et al.* Activation and closed-state inactivation mechanisms of the human voltage-gated KV4 channel complexes. *Mol. Cell* **82**, 2427-2442.e4 (2022).
25. Frank An, W. *et al.* Modulation of A-type potassium channels by a family of calcium

sensors. *Nature* **403**, 553–556 (2000).
26. Pruunsild, P. & Timmusk, T. Structure, alternative splicing, and expression of the human and mouse KCNIP gene family. *Genomics* **86**, 581–593 (2005).
27. Bähring, R. Kv channel-interacting proteins as neuronal and non-neuronal calcium sensors. *Channels* **12**, 187–200 (2018).
28. Jerng, H. H. & Pfaffinger, P. J. Modulatory mechanisms and multiple functions of somatodendritic A-type K+ channel auxiliary subunits. *Front. Cell. Neurosci.* **8**, 1–20 (2014).
29. Buxbaum, J. D. *et al.* Calsenilin: A calcium-binding protein that interacts with the presenilins and regulates the levels of a presenilin fragment. *Nat. Med.* **4**, 1177–1181 (1998).
30. Nassal, D. M., Wan, X., Liu, H., Laurita, K. R. & Deschênes, I. KChIP2 regulates the cardiac Ca2+ transient and myocyte contractility by targeting ryanodine receptor activity. *PLoS One* **12**, 1–15 (2017).
31. Thomsen, M. B. *et al.* Accessory subunit KChIP2 modulates the cardiac L-Type calcium current. *Circ. Res.* **104**, 1382–1389 (2009).
32. Zhang, Y. *et al.* The DREAM protein negatively regulates the NMDA receptor through interaction with the NR1 subunit. *J. Neurosci.* **30**, 7575–7586 (2010).
33. Callsen, B. *et al.* Contribution of N- and C-terminal channel domains to Kv channel interacting proteins in a mammalian cell line. *J. Physiol.* **568**, 397–412 (2005).
34. Ma, D. *et al.* Structural basis for the gating modulation of Kv4.3 by auxiliary subunits. *Cell Res.* **32**, 411–414 (2022).
35. Kise, Y. *et al.* Structural basis of gating modulation of Kv4 channel complexes. *Nature* **599**, 158–164 (2021).
36. Nadal, M. S., Amarillo, Y., Vega-Saenz De Miera, E. & Rudy, B. Evidence for the presence of a novel Kv4-mediated A-type K+ channel-modifying factor. *J. Physiol.* **537**, 801–809 (2001).
37. Nadal, M. S. *et al.* The CD26-related dipeptidyl aminopeptidase-like protein DPPX is a critical component of neuronal A-type K+ channels. *Neuron* **37**, 449–461 (2003).
38. Takimoto, K., Hayashi, Y., Ren, X. & Yoshimura, N. Species and tissue differences in the expression of DPPY splicing variants. *Biochem. Biophys. Res. Commun.* **348**, 1094–1100 (2006).
39. Nadal, M. S., Amarillo, Y., de Miera, E. V. S. & Rudy, B. Differential characterization of three alternative spliced isoforms of DPPX. *Brain Res.* **1094**, 1–12 (2006).
40. Jerng, H. H., Kunjilwar, K. & Pfaffinger, P. J. Multiprotein assembly of Kv4.2, KChIP3 and DPP10 produces ternary channel complexes with ISA-like properties. *J. Physiol.* **568**, 767–788 (2005).
41. Wang, X., Bao, J., Zeng, X. M., Liu, Z. & Mei, Y. A. Elevation of intracellular Ca2+ modulates A-currents in rat cerebellar granule neurons. *J. Neurosci. Res.* **81**, 530–540 (2005).
42. Anderson, D. *et al.* The Cav3-Kv4 complex acts as a calcium sensor to maintain inhibitory charge transfer during extracellular calcium fluctuations. *J. Neurosci.* **33**, 7811–7824 (2013).
43. Anderson, D. *et al.* Regulation of neuronal activity by Cav3-Kv4 channel signaling complexes. *Nat. Neurosci.* **13**, 333–337 (2010).
44. Curtis, H. J. & Cole, K. S. Membrane resting and action potentials from the squid giant axon. *J. Cell. Comp. Physiol.* **19**, 135–144 (1942).
45. Hodgkin, A. L., Huxley, A. F. & Katz, B. Measurement of current□voltage relations in the membrane of the giant axon of Loligo. *J. Physiol.* **116**, 424–448 (1952).
46. Guan, B., Chen, X. & Zhang, H. Two-electrode voltage clamp. in *Methods in Molecular Biology* vol. 998 79–89 (2013).
47. Verkhratsky, A. & Parpura, V. History of electrophysiology and the patch clamp. *Methods Mol. Biol.* **1183**, 1–19 (2014).
48. Jue, T. *Modern Tools of Biophysics*. *Modern Tools of Biophysics* (Springer New York, 2017). doi:10.1007/978-1-4939-6713-1.
49. Zal, T. & Gascoigne, N. R. J. Photobleaching-corrected FRET efficiency imaging of live

cells. *Biophys. J.* **86**, 3923–3939 (2004).
50. Terhag, J., Cavara, N. A. & Hollmann, M. Cave Canalem: How endogenous ion channels may interfere with heterologous expression in Xenopus oocytes. *Methods* **51**, 66–74 (2010).
51. Yang, H., Zhang, G. & Cui, J. BK channels: Multiple sensors, one activation gate. *Front. Physiol.* **6**, 1–16 (2015).
52. Beck, E. J. & Covarrubias, M. Kv4 Channels Exhibit Modulation of Closed-State Inactivation in Inside-Out Patches. *Biophys. J.* **81**, 867–883 (2001).
53. Strassle, B. W., Menegola, M., Rhodes, K. J. & Trimmer, J. S. Light and electron microscopic analysis of KChIP and Kv4 localization in rat cerebellar granule cells. *J. Comp. Neurol.* **484**, 144–155 (2005).
54. Groen, C. & Bähring, R. Modulation of human Kv4.3/KChIP2 channel inactivation kinetics by cytoplasmic Ca 2+. *Pflugers Arch. Eur. J. Physiol.* **469**, 1457–1470 (2017).
55. Murphy, J. G. & Hoffman, D. A. A polybasic motif in alternatively spliced KChIP2 isoforms prevents Ca2 regulation of Kv4 channels. *J. Biol. Chem.* **294**, 3683–3695 (2019).
56. Murphy, J. G. *et al.* R-type voltage-gated Ca2+ channels mediate A-type K+ current regulation of synaptic input in hippocampal dendrites. *Cell Rep.* **38**, 110264 (2022).
57. Bindels, D. S. *et al.* MScarlet: A bright monomeric red fluorescent protein for cellular imaging. *Nat. Methods* **14**, 53–56 (2016).
58. McCullock, T. W., MacLean, D. M. & Kammermeier, P. J. Comparing the performance of mScarlet-I, mRuby3, and mCherry as FRET acceptors for mNeonGreen. *PLoS One* **15**, 1–22 (2020).
59. Anderson, D. *et al.* Regulation of the KV4.2 complex by CaV3.1 calcium channels. *Channels* **4**, 163–167 (2010).
60. Turner, R. W. & Zamponi, G. W. T-type channels buddy up. *Pflugers Arch. Eur. J. Physiol.* **466**, 661–675 (2014).
61. Augustine, G. J., Santamaria, F. & Tanaka, K. Local calcium signaling in neurons. *Neuron* **40**, 331–346 (2003).
62. Naraghi, M. & Neher, E. Linearized buffered Ca2+ diffusion in microdomains and its implications for calculation of [Ca2+] at the mouth of a calcium channel. *J. Neurosci.* **17**, 6961–6973 (1997).
63. Ramachandran, P. L. *et al.* The Potassium Channel Interacting Protein 3 (DREAM/KChIP3) Heterodimerizes with and Regulates Calmodulin Function. *J. Biol. Chem.* **287**, 39439–39448 (2012).
64. Yao, J., Zhao, Q.-R., Liu, D.-D., Chow, C.-W. & Mei, Y.-A. Neuritin Up-regulates Kv4.2 α-Subunit of Potassium Channel Expression and Affects Neuronal Excitability by Regulating the Calcium-Calcineurin-NFATc4 Signaling Pathway. *J. Biol. Chem.* **291**, 17369–17381 (2016).
65. Rossow, C. F., Dilly, K. W. & Santana, L. F. Differential calcineurin/NFATc3 activity contributes to the Ito transmural gradient in the mouse heart. *Circ. Res.* **98**, 1306–1313 (2006).
66. Jo, D. G., Jang, J., Kim, B. J., Lundkvist, J. & Jung, Y. K. Overexpression of calsenilin enhances γ-secretase activity. *Neurosci. Lett.* **378**, 59–64 (2005).
67. Pham, K. & Miksovska, J. Molecular insight of DREAM and presenilin 1 C-terminal fragment interactions. *FEBS Lett.* **590**, 1114–1122 (2016).
68. Leissring, M. A. *et al.* Calsenilin reverses presenilin-mediated enhancement of calcium signaling. *Proc. Natl. Acad. Sci. U. S. A.* **97**, 8590–8593 (2000).
69. LaFerla, F. M. Calcium dyshomeostasis and intracellular signalling in alzheimer's disease. *Nat. Rev. Neurosci.* **3**, 862–872 (2002).
70. Wu, L. J. *et al.* DREAM (Downstream Regulatory Element Antagonist Modulator) contributes to synaptic depression and contextual fear memory. *Mol. Brain* **3**, 1–13 (2010).
71. Bähring, R. *et al.* Conserved Kv4 N-terminal Domain Critical for Effects of Kv Channel-interacting Protein 2.2 on Channel Expression and Gating. *J. Biol. Chem.* **276**, 23888–23894 (2001).

72. Li, Y. *et al.* Kv4.2 phosphorylation by PKA drives Kv4.2-KChIP2 dissociation, leading to Kv4.2 out of lipid rafts and internalization. *Am. J. Physiol. - Cell Physiol.* **323**, C190–C201 (2022).
73. Varga, A. W., Anderson, A. E., Adams, J. P., Vogel, H. & Sweatt, J. D. Input-specific immunolocalization of differentially phosphorylated Kv4.2 in the mouse brain. *Learn. Mem.* **7**, 321–332 (2000).
74. Shibata, R. *et al.* A fundamental role for KChIPs in determining the molecular properties and trafficking of Kv4.2 potassium channels. *J. Biol. Chem.* **278**, 36445–36454 (2003).
75. Seikel, E. & Trimmer, J. S. Convergent modulation of Kv4.2 channel α subunits by structurally distinct DPPX and KChIP auxiliary subunits. *Biochemistry* **48**, 5721–5730 (2009).
76. Hammond, R. S., Lin, L., Sidorov, M. S., Wikenheiser, A. M. & Hoffman, D. A. Protein kinase a mediates activity-dependent Kv4.2 channel trafficking. *J. Neurosci.* **28**, 7513–7519 (2008).
77. Nestor, M. W. & Hoffman, D. A. Differential cycling rates of Kv4.2 channels in proximal and distal dendrites of hippocampal CA1 pyramidal neurons. *Hippocampus* **22**, 969–980 (2012).
78. Schrader, L. A. *et al.* ERK/MAPK regulates the Kv4.2 potassium channel by direct phosphorylation of the pore-forming subunit. *Am. J. Physiol. - Cell Physiol.* **290**, C852–C861 (2006).
79. Hu, J. –H *et al.* Activity-dependent isomerization of Kv4.2 by Pin1 regulates cognitive flexibility. *Nat. Commun.* **11**, (2020).
80. Hu, J. H., Malloy, C. & Hoffman, D. A. P38 regulates kainic acid-induced seizure and neuronal firing via kv4.2 phosphorylation. *Int. J. Mol. Sci.* **21**, 1–16 (2020).
81. Kim, K. R. *et al.* Calbindin regulates Kv4.1 trafficking and excitability in dentate granule cells via CaMKII-dependent phosphorylation. *Exp. Mol. Med.* **53**, 1134–1147 (2021).
82. Varga, A. W. *et al.* Calcium-Calmodulin-Dependent Kinase II Modulates Kv4.2 Channel Expression and Upregulates Neuronal A-Type Potassium Currents. *J. Neurosci.* **24**, 3643–3654 (2004).
83. Sergeant, G. P. *et al.* Regulation of Kv4.3 currents by Ca2+/calmodulin- dependent protein kinase II. *Am. J. Physiol. - Cell Physiol.* **288**, 304–313 (2005).
84. Colinas, O. *et al.* Differential modulation of Kv4.2 and Kv4.3 channels by calmodulin-dependent protein kinase II in rat cardiac myocytes. *Am. J. Physiol. - Hear. Circ. Physiol.* **291**, 1978–1987 (2006).
85. El-Haou, S. *et al.* Kv4 potassium channels form a tripartite complex with the anchoring protein SAP97 and CaMKII in cardiac myocytes. *Circ. Res.* **104**, 758–769 (2009).

8. Appendix

Publications

Related to this dissertation:

-None

Other publications:

KCND2 variants associated with global developmental delay differentially impair Kv4.2 channel gating

Zhang Y, **Tachtsidis G**, Schob C, Koko M, Hedrich U, Lerche H, Lemke J, van Haeringen A, Ruivenkamp C, Prescott T, Tveten K, Gerstner T, Pruniski B, DiTroia S, VanNoy G, Rehm H, McLaughlin H, Bolz H, Zechner U, Bryant E, McDonough T, Kindler S, Bähring R

HUM MOL GENET. 2021;30(23):2300-2314.

Aberrations

ATP	Adenosine-triphosphate
BK	large conductance Ca^{2+} activated K^{+} channels
CHO	Chinese hamster ovary cells
DNA	Deoxyribonucleic acid
DPP	dipeptidyl aminopeptidase-like protein
HEK	human embryonic kidney cells
HEPES	N-2-hydroxyethylpiperazine-N-2-ethane sulfonic acid
KChIP	Kv channel interacting protein
KChIP^{R}	Epitope-tagged KChIP-mRuby3 auxiliary subunit
Kv4.2^{C}	Epitope-tagged Kv4.2-mClover3 channel
NCS	Neuronal Calcium Sensor
RNA	Ribonucleic acid
RPM	Rounds per minute
SD	Standard deviation
SK	small conductance Ca^{2+} activated K+ channels
VSD	voltage-sensing domain

Acknowledgements

My deepest thanks go to my supervisor, Prof. Dr. Robert Bähring for giving me the opportunity to study in such an interesting research field. I am very grateful for the great care he took in teaching me and allowing me to expand my knowledge in the scientific field.

I also want to thank everyone at the Institute of Cellular and Integral Physiology for making my time there more fun and for boosting my academic experience. My sincere gratitude goes out to Leya Eckermann, whose persistent presence made me smile and contributed a lovely touch to my work.
A special thank you to Woyou Cao for our enjoyable discussions on science and, additionally, the many cuisines that made my writing time much more enjoyable.
I also want to thank Yongqiang Zhang and Annett Hasse for teaching me everything throughout my first few months of studies and Dr. Desiree Loreth for introducing me and guiding me through the fluorescence recordings.
My appreciation to Prof. Dr. Christiane Bauer for her assistance in addressing many of my queries and for the enjoyable recording sessions that included some history lectures on electrophysiology.
A special thank you to Claudia Kollien, who helped me navigate certain bureaucratic processes with apparent ease.

Lastly, I would like to express my gratitude to everyone in my private field for every bit of support I received in the wildest times during a global pandemic conjoined with a crisis on top of an ongoing PhD procedure. A special thanks to my psychiatrist and therapist for supporting me through each internal crisis and guiding me through my most vulnerable times.